Interface Magnetic Properties in Ferromagnetic Metal/Semiconductor and Related Heterostructures

Yu Yan

PhD

University of York
Electronic Engineering
December 2017

Abstract

This dissertation investigates the growth and magnetic properties of magnetic thin films deposited on semiconductor GaAs and the insulator MgO, which could be useful for devices such as Spin-FET and MRAM.

CoFeB amorphous films were grown on both GaAs and MgO. We have studied the origin of the uniaxial magnetic anisotropy (UMA) and perpendicular magnetic anisotropy (PMA) with TEM, VSM and XMCD. Our results demonstrated that the orbital moment of Co atoms play an important role to both UMA and PMA.

The origin of UMA in Fe/GaAs (100) system with Cr interlayers is explored. The values of UMA in the Fe/GaAs systems were found to be dependent on the thickness of Cr interlayer by the SQUID-VSM measurements. RHEED patterns and TEM images offered the morphology and crystalline structure information of different layers in the samples. Our results show that the UMA disappears when the interlayer Cr forms continuous film of around 5 ML. This offers direct evidence for the first time that the origin of UMA is from the interface bonding rather than the lattice mismatch related film stress.

Finally, Fe films were deposited onto GaAs (100) substrate with a heavy metal element Au interface layer. The enhancement of UMA was found in the Fe/Au/GaAs system by the VSM measurements. The XMCD results show that the orbital moment of Fe is enhanced when the Au interlayer is under 0.5 ML, which leads to the enhancement of the UMA in the Fe/Au/GaAs system.

Results from the three different systems provide an important understanding of the research into the interface magnetic properties of ferromagnetic metal/semiconductors. These interesting discoveries are very useful for the development of next generation electronic devices like MRAM and SpinFET.

Contents

List of Figures

Chapter 2

Chapter 3

Chapter 4

Chapter 5

Figure 5.17 (a) and (b) indicate the orbital moment and spin moment of Cr atoms with different thicknesses of Cr interlayer between 10 ML Fe films and GaAs (100) substrate respectively.

Chapter 6

Figure 6.1 shows the RHEED patterns from GaAs (100) substrates ($[0\bar{1}1]$ view), the various thicknesses of Au interlayers and 10 ML Fe films which grew on the Au interlayer. The thickness of the Au interlayer is from 0ML to 5ML, and the thickness of Fe remains 10ML.

Figure 6.2 VSM hysteresis loops of various Au interlayer thickness (from 0 to 5ML) between GaAs (100) substrate and 10 ML Fe. These loops are all measured at room temperature with the 3000 Oe magnetic field applied along [011] and $[0\bar{1}1]$ (hard axis and easy axis respectively)

Figure 6.3 (a) and (b) are the tendency charts for the saturation field and effective uniaxial anisotropy constant respectively.

Figure 6.4 XAS and XMCD spectra of Fe atoms at L_2 and L_3 edges in Cr(3nm)/Fe(10ML)/Au/GaAs (100) from (a) to (f): (a), (b), (c) are the thickness of Au interlayer for 0ML, 0.2 ML and 0.5 ML respectively. (d), (e), (f), are the thickness of Au interlayer for 1 ML, 2 ML and 5ML respectively.

Figure 6.5 presents black and red lines which show the orbital moment and spin moment of Fe atoms with different thicknesses of Au interlayers. The green line gives the values for the orbital to spin ratio.

List of Tables

Chapter 3

Chapter 4

Chapter 5

Chapter 6

Acknowledgements

A thesis is a summary of the research work and results of years of hard work that only could have been possible with many others helping me by my side. My greatest gratitude would be my supervisor Prof. Yongbing Xu for offering me an opportunity of PhD research and freedom to let me work on my own.

I would also thank Dr. Sarnjeet, Dr. Francesco Maccherozzi, Dr. Paul Steadman, Dr. Peter Bencok and the technician teams from I06 and I10 Diamond Light Source in Rutherford Appleton Laboratory for such an exciting collaboration; Dr. Iain Will, Mr. Jonathan Creamer, Mr Charan Panesar for professional support and guidance in the MBE lab and cleanroom; Dr. Vlado Lazarov, Mr Ian Wright for the instructions in the nanocentre. My practical experience was sharpened because of you, and it really benefits me throughout the whole PhD period.

My colleagues are the next group of people I must pay gratitude for. You have been my spiritual companions for years and we shared the same experience of pursuing for PhD degree. I’m glad some of you have already achieved it, and I wish those who are still on the way the best luck. Your names are: Dr. Jing Wu, Dr. Cong Lu, Mr. Nicholas Maltby, Dr. James Sizeland, Dr. Wenqing Liu, Mr. Junlin Wang, Mr. Yichuan Wang, Mr. Kunpeng Zhang, Mr. Xiangyu Zheng, Mr. Lingyu Yan and Mr. Hua Lin. Special thanks go to Mr. Xianyang Lu, who has contributed a lot for my last period of experiment and writing up.

The last and the greatest belongs to my family for their unwavering support throughout my studies. Their words of encouragement served as a source of motivation and helped me pull through unbearable times.

Declaration of Authorship

I declare that this thesis titled, “Interface Magnetic Properties in Ferromagnetic Metal/Semiconductor and Related Heterostructures”, and the work presented in it are my own. I confirm that:

This work was done wholly or mainly while in candidature for a research degree at this university and has not been submitted previously for a degree at this or any other university.

Where I have quoted from the work of others, the source is always given. Except for such quotations, this thesis is entirely my own work. I have acknowledged all main sources of help.

Where the thesis is based on work done by myself jointly with other, I have made clear exactly what was done by others and what I have contributed myself.

Publication List

1. Y. Yan, Cong Lu, Xiangyang Lu, Wenqing Liu, Junling Wang, Iain G Will, Vlado K. Lazarov, Jun Du, Jing Wu, Rong Zhang, Yongbing Xu, "Element specific spin and orbital moments of nanoscale CoFeB amorphous thin films on GaAs (100)," *AIP Advances,* vol. 6, no. 9, p. 095011, 2016. (This paper got the best poster award in the 26th Chinese Physical Society, Beijing, 03/09/2016)

2. Yu Yan, Xianyang Lu, Wenqing Liu, Xiaoqian Zhang, Junlin Wang, Kunpeng Zhang, Sarnjeet S. Dhesi, Iain G. Will, Vlado K. Lazarov, Jun Du, Jing Wu, Rong Zhang, Yongbing Xu. "The origin of the uniaxial magnetic anisotropy in Fe/GaAs (100) system". (submitted to Physic Review Letter on 18/12/2017)

3. Junlin Wang, Yu Yan, Xiangyang Lu, Jason Zhang, Hua Ling, Xichao Zhang, Jing Wu, Yan Zhou and Yongbing Xu, "Magnetic domain wall engineering in a nanoscale permalloy junction," *Applied Physics Letters,* vol. 111, no. 7, p. 072401, 2017.

4. Yongbing Xu, PingKwan Johnny Wong, Wenqing Liu, Daxin Niu, Yongxiong Lu, Iain Gordon Will, Yu Yan, Sameh Hassan, Wen Guo Zhang, "Magnetic/III-V Semiconductor Based Hybrid Structures," *Handbook of Spintronics,* pp. 285-333, 2016.

5. Lu, Xianyang; Yu Yan: Lu, Cong; Zhang, Kunpeng; Jin, Fang; Wu, Jing; Will, Iain G.; Xu, Yongbing. "The correlation between GaAs surface treatment and interface magnetic anisotropy in Fe/GaAs(100) heterostructure". (submitted to JPhysD on 07/12/2017)

6. Hua Ling, Junlin Wang, Yu Yan, Xiangyang Lu, Junran Zhang, Christopher Reardon, Jason Zhang, Yichuan Wang, Jing Wu and Yongbing Xu. "Effect of Notch Structure on Magnetic Domain Movement in Planar Nanowires". (submitted to Applied Physics Letter on 01/11/2017)

Chapter 1 Introduction

1.1 The Evolution of Electronic Devices

The success of semiconductor-based electronics has been built on the nature of the charge freedom of electrons found in semiconductors. Electronic devices began in 1947 with the discovery of transistor action in Bell Labs[1]. Following this, many semiconductor devices such as field-effect-transistors (FET), light emitting diodes (LED) and integrated circuits (IC) have become popular topic areas over the last seven decades. These revolutions have supported the enormous development of the computational industry whilst simultaneously – and constantly – demanding higher performance. After decades of development, the industry might hit the wall of Moore's Law in the near future, meaning that requirements for higher speed, lower energy dissipation and denser medium and components are now at the top of the priority research list.

The next generation of electronic devices will be smaller, more robust and have lower energy consumption. One possibility to improve the function of electronic devices may be to use the intrinsic angular momentum or the spin of an electron as an extra degree of freedom. This new field of research has triggered the development of a series of new multidisciplinary researches in which the aim is to integrate spin dependent effects with semiconductor functionalities which have already been developed. The term "spintronics" is used in general to encompass the ideas of coupling electronic spin and charge in physics.

1.2 Definition and Application of Spintronics

Spintronics, also known as "spin electronics" or "magnetoelectronics", is the study of the spin of the electron and its associated magnetic moment, in addition to its fundamental electronic charge, in solid-state devices. Spintronics fundamentally differs from traditional electronics in that, in addition to its charge state, electron spins are exploited as a further degree of freedom, with implications in terms of the efficiency of data storage and transfer.

Spintronics emerged from discoveries in the 1980s concerning spin-dependent electron transport phenomena in solid-state devices. This includes the observation of spin-polarised electron injection from a ferromagnetic metal to a normal metal by Johnson and Silsbee[1] in 1985, and the independent discovery of giant magnetoresistance (GMR) by French and German physicists [2] in 1988, both of whom were awarded the Nobel Prize. It results in spin dependent conduction in magnetic thin films, which cause phenomenon changes in resistivity when the magnetisation state is changed. The best-known application of this effect was the read head incorporating GMR material in hard-disk drives, which would be able to sense much smaller magnetic field changes and greatly increase the storage density on each hard disk.

The simplest method for generating a spin-polarised current in a metal is to pass the current through a ferromagnetic material. The most common application of this effect is GMR devices. A typical GMR device consists of at least two layers of ferromagnetic materials separated by a spacer layer. When the two magnetisation vectors of the ferromagnetic layers are aligned, the electrical resistance will be lower than if the ferromagnetic layers are anti-parallel. This constitutes a magnetic field sensor. Two GMR models have been used in devices: (1) The current -in-plane (CIP) model, where the electric current flows parallel to the layers; and (2) the current-perpendicular-to-plane (CPP) model, where the electric current flows in a direction perpendicular to the layers. The other metal-based spintronics devices include Tunnel magnetoresistance (TMR) and Spin-transfer torque (STT). TMR, where CPP transport is achieved by using quantum-mechanical tunnelling of electrons through a thin insulator separating ferromagnetic layers. STT is where a current of spin-polarised electrons is used to control the magnetisation direction of ferromagnetic electrodes in the device.

Other spintronic applications are spintronic-logic devices and semiconductor-based spintronic devices. Spin-transfer, torque-based logic devices that use spin and magnets for information processing have been proposed. Logic-in-memory applications are in the development stage, with many articles having been written on this over the last decade[3] . Doped semiconductor materials display dilute ferromagnetism. In recent years, dilute magnetic oxides (DMOs), including ZnO based DMOs and TiO_2 based DMOs, have been the subject of numerous experimental and computational investigations. Non-oxide ferromagnetic semiconductor sources (like manganese-doped gallium arsenide GaMnAs), increase the interface resistance with a tunnel barrier, or by using hot-electron injection.

Metallic spintronic devices, such as hard disk read heads and magnetic random-access memory (MRAM) have been one of the most successful technologies of the last decade. However, hybrid spintronic devices consisting of both magnetic metals and semiconductors offer an opportunity to unify processing, communication, and storage within the same technology[3]. Hybrid ferromagnetic and semiconductor structures have demonstrated their theoretical and experimental potential for highly-efficient spin injection at room temperatures by employing a Schottky tunnelling barrier between ferromagnetic metals and semiconductors[4, 5].

1.3 Aims of this PhD Work

To improve the transfer process and storage functions of semiconductor devices, the control of the magnetic properties during thin film growth and understanding uniaxial magnetic anisotropy (UMA) and interface interaction effects within hybrid ferromagnetic (FM)/semiconductor devices are critical issues in current spintronics. This PhD work aims to grow various thicknesses of interlayers with different materials to study the surface structures between the interface and interlayers. An in-situ RHEED (reflection high energy electron diffraction) measurement has been established to monitor the morphology, structure and surface quality during MBE (molecular beam epitaxy) growth of magnetic thin films on semiconductor substrates. TEM (transmission electron microscopy) measurement is subsequently used for the key samples, which have the potential to form TEM images from specimens. TEM images can evidence the thickness of samples and obtain a high resolution of the sample structure and interface surface situation.

Another important aim is to use VSM (vibrating Sample Magnetometer) measurement to research the origin of UMA and the magnetic properties of interlayers or interface interaction. From VSM observations, the change of magnetic properties or uniaxial magnetic anisotropy can be performed intuitively, meaning that these results can be compared with previous researches. Finding that changes of magnetic properties from the interlayer or interface means that the interface interaction and the origin of uniaxial magnetic anisotropy can be fully researched and explained.

Last but not least, XMCD centred projects were included as a contribution. This part of my PhD project uses synchrotron radiation as a powerful tool for analysing the magnetic moment information for individual elements in magnetic films. The values of spin moment, orbital moment and spin to orbital ratios can be calculated using sum rules. These data can be used to understand the atomic scale mechanism of the uniaxial magnetic anisotropy and perpendicular magnetic anisotropy in an amorphous film and the uniaxial magnetic anisotropy in the Fe-GaAs system.

1.4 Thesis Overview

Chapter 2 reviews magnetic ordering, the origin of magnetic anisotropy, and the different structures of the Fe-GaAs and CoFeB systems. The experimental methods used for this project will be described in Chapter 3, which will cover the preparation, fabrication and characterisation of the magnetic thin film samples. In Chapter 4, UMA and PMA effects are studied for the CoFeB-GaAs (100) sample and CoFeB/MgO structures, respectively. The magnetic moment of both Co and Fe elements were separately analysed in terms of the XMCD spectra, and the results are supported by VSM and TEM cross-section inspections to identify the contribution of these two elements. In Chapter 4, the two systems with various thicknesses of Cr interlayer between Fe and GaAs (100) substrate were studied using RHEED, VSM and XMCD measurements. This work has investigated the origins of UMA by engineering the Fe-GaAs interface with the Cr interlayer. In Chapter 6, the heavy metal (Au) interlayer was inserted between Fe and GaAs (100) with various thicknesses. The large spin-orbital coupling of the interface Au might affect the UMA and orbital moment of Fe in the Fe/Au/GaAs system.

The final chapter presents conclusions for my PhD project, and makes recommendations about future work or complementary experiments which could be done using the knowledge generated in this project.

Chapter 2 Theoretical Background and Literature Review

2.1 Introduction

Spintronics is to exploit the fact that electrons have spin as well as charge, whereby electrons' spins and not just their electrical charge can be manipulated within electronic circuits. It is anticipated that spintronic devices will be non-volatile, versatile, fast, and capable of simultaneous data storage and processing, whilst also consuming less energy. Already, they play an increasingly significant role in high-density data storage, microelectronics, magnetic sensors, quantum computing and biomedical applications, amongst other applications.

The main purpose of this chapter is to provide useful background information concerning the understanding of the experimental work presented in this thesis. Initially, a brief review of magnetic ordering and domains will be presented, which will include studies connected to ferromagnetism and antiferromagnetism. Following this will be discussions concerning recent technological advancements in magnetic anisotropy. Finally, the two magnetic heterostructure systems, namely Fe/GaAs system and CoFeB system, both of which are highly relevant to my projects, will be reviewed.

2.2 Magnetic Ordering and Domains

The term 'magnetic materials' is generally used to refer to materials where spontaneous magnetic ordering takes place. The stability of the ordered state is due to the 'exchange interaction', which can be defined as a quantum mechanical effect that describes the change in energy and distance of multiple particles when their wave functions overlap. Indeed, models of magnetic systems and experiments on materials which are well described by such models are central in the study of critical phenomena. This section will, therefore, focus on the types of order and the interaction models that bring about the ordered states.

The simple classification of ordered states into ferromagnets, antiferromagnets and ferrimagnets does not do justice to the rich variety of possible ordered patterns of three-dimensional vectors at the sites of all the crystal lattices which are possible in three dimensions. Initially, these magnets are associated with collinear structures, ↑↑↑↑↑↑, ↑↓↑↓↑↓ and ↑↑↓↑↑↓. However, the angle between neighbouring magnetic moments is not limited to zero and π, and the orientation of moments with respect to the crystal axes is also an important variable – a variable which can vary with the temperature. Aside from the exchange interaction, magneto crystalline anisotropy is also an important factor in determining the nature of the ordered state.

In the rare earth to transition metal ferromagnets, the anisotropy energy of the rare earth component is much larger than that of the transition metal because the spin-orbit coupling is an order of magnitude stronger. Given that the orientations preferred by these anisotropy energies are different, so too are their temperature dependences. The result of this is that the overall effect is also temperature dependent, meaning that the orientation of the net ferromagnetic moment changes with temperature. Similar effects in antiferromagnets are not conspicuous because there is no net magnetisation, although it should be noted that some, most notably α-Fe_2O_3, $MnCO_3$ and CrF_3, do show a small magnetic moment ("weak ferromagnets"), which signals a slight noncollinearity of oppositely oriented moments due to an anisotropic super exchange interaction.

When the exchange interaction between two spins has a positive value, the spins will be aligned in the same direction regardless of whether there is an external field. Spontaneous magnetisation occurs when the material is below its Curie temperature, a type of magnetic ordering known as ferromagnetism. At the microscopic level, these aligned spins should generate a magnetic moment which points in a certain direction, but in fact most macroscopic ferromagnetic materials do not show a net magnetisation unless an external field is applied. This can be explained by introducing the concept of domains.

The domain hypothesis was one of the two concepts introduced by Weiss in 1906, the other being the molecular field. In 1949 came a clear understanding of the domain structure of a real material through Williams, Bozorth and Shockley[6], whose work was undertaken at the Bell Telephone Laboratories on domains in silicon-iron single crystals. Since that time, domain theory has been central to any discussion of the magnetisation processes. However, because Weiss still had to account for the spontaneous alignment of atomic moments within a ferromagnetic material, he developed the so-called Weiss mean field. Here, he assumed that a given magnetic moment in a material experienced a very high effective magnetic field due to the magnetisation of its neighbours. In the original Weiss theory[7], the mean field was proportional to the bulk magnetisation M, so that

$$H_e = \alpha M \tag{2.1}$$

Where, α is the mean field constant. However, this is not applicable to ferromagnets because of the variation of magnetisation from domain to domain. In this case, the interaction field is

$$H_e = \alpha M_s \tag{2.2}$$

Where, M_s is the saturation magnetisation.

Quantum theory made it possible to understand the microscopic origin of the Weiss field, in which the exchange interaction between localised spins favoured a parallel (in ferromagnets) or an anti-parallel (in antiferromagnets) state of neighbouring magnetic moments.

Domains are formed because their configuration minimises the total stray field energy of the bulk material, which is a more energetically favourable state for the coupled spins. When a macroscopic material has all its spins aligned, the magnetostatic energy reaches its maximum value, which is an unfavourable state. To enter a favourable state (the lowest magnetostatic energy), a single domain must break into multiple small units that all contain strongly coupled and aligned spins, but which point in different directions. In the absence of an external field, the preferential directions of each domain are determined by magnetic anisotropy. At the boundary regions of the domains, the direction of the magnetisation is gradually rotated to align with the neighbouring domain. Depending on the thickness of the material, the rotation of the magnetisation can take place on a plane which is either parallel or perpendicular to the domain wall plane. In thin films, it is usually a Néel wall[8], and a Block wall for thick films. The widths of the domain walls are usually within tens of nanometres, and are determined by the exchange and anisotropy energy.

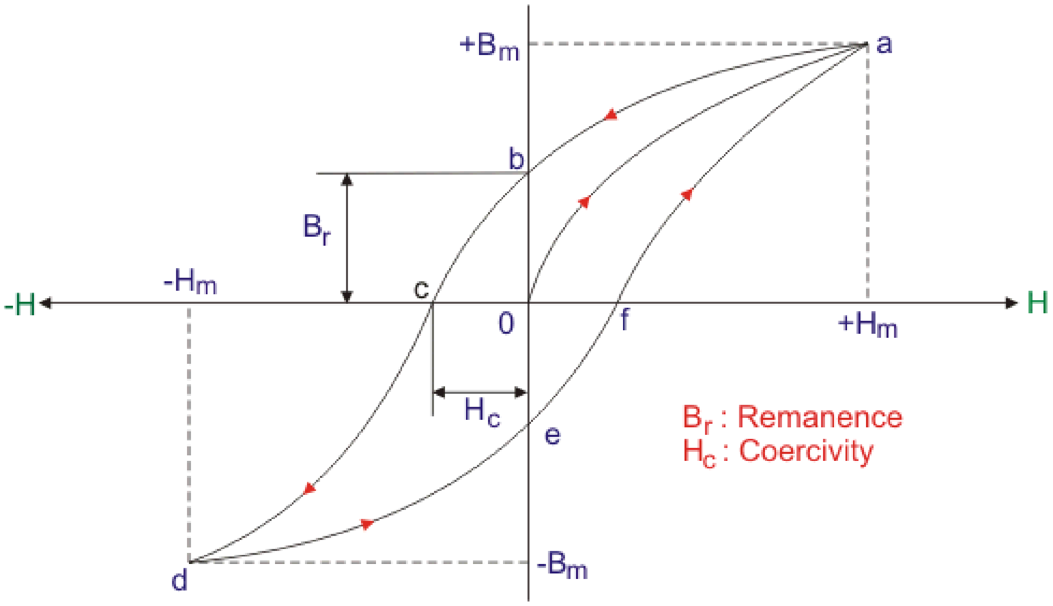

Figure 2.1 Typical hysteresis loop.

If a large magnetic field is applied to a ferromagnetic material, the magnetisation direction of domains will be forced to align, thereby producing a net magnetisation vector. At first, the magnetisation increases significantly, but then as more and more domains are aligned along the field direction, the speed will decrease until all the domains are aligned. Eventually, the magnetisation will reach its maximum value, which is known as its saturation point (M_S). When the magnetic field is decreased, the magnetisation decreases more slowly than the magnetic field, meaning that when the magnetic field reaches zero, the magnetisation does not. The remaining magnetisation is called remanent magnetisation (M_r). To bring any remanent magnetisation back to zero, a negative magnetic field is needed. A small negative field will change the direction of domains, forcing them to be non-aligned. This will result in all the domains summing to zero, meaning the net magnetisation will return to zero. The field required to accomplish this is called coercivity (H_c), and it is considered a very important property of any ferromagnetic material. It is strongly affected by not only the crystalline structure of the material, but also the deposition conditions and processes. If the magnetic field further decreases, the domains will be re-aligned in the opposite direction, and a negative saturation point will eventually be reached. A negative remanence and coercivity will also be present should the field be increased back to zero, and then again when the domain is re-randomised. In general cases, the negative and positive M_s, M_r and H_c are expected to be of the same value, thus the plot of magnetisation against the applied field on the positive and negative regions should be symmetrical and form a closed loop, which is known as the Hysteresis loop.

The alignment of the spins or spontaneous magnetisation can only occur when ferromagnetic materials are below their Curie temperature. The Curie temperature is different for various materials, and it is also dependent on the exchange interaction between spins. If the materials are above the Curie temperature, the thermal energy will exceed the exchange energy. This causes the coupled spin to break up, leading to the ferromagnetic materials eventually becoming paramagnetic.

2.2.1 Ferromagnetism

The term ferromagnetism is used to characterise strongly magnetic behaviour, such as the strong attraction of a material to a permanent magnet. The origin of this strong magnetism is the presence of a spontaneous magnetisation produced by a parallel alignment of spins due to exchange interaction.

Magnetisation curves of iron, cobalt and nickel are shown below in figure 2.2[9]. These curves are presented to emphasise that the shape of curve from $\mathrm{M} = 0$ to $\mathrm{M} = M_S$ and the strength of the field at which saturation is attained are both structure-sensitive properties, whereas the magnitude of M_S is not.

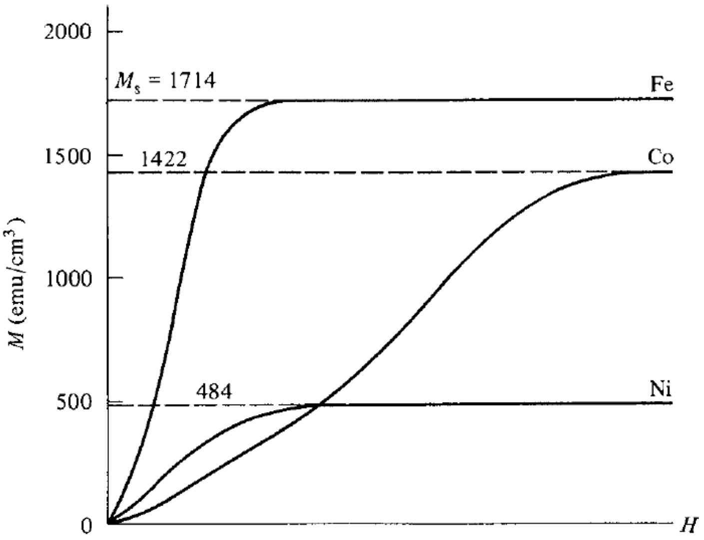

Figure 2.2 Magnetisation curves of iron, cobalt, and nickel at room temperature[9].

A single crystal of pure iron can be brought to near saturation in a field of less than 50 Oe or 4 kA/m along easy axis. Each cubic centimetre then has a magnetic moment of about 1700 emu (or each cubic metre a moment of about 1.7 MAm^2 or MJ/T). In the same field, a typical paramagnet will have a magnetisation of about 1023 $\mathrm{emu/cm}^3$ or 1 A/m. Ferromagnetism, therefore, involves an effect which is at least a million times as strong as any which has yet been considered.

The mechanism for the appearance of spontaneous magnetisation was first clarified in 1906 in Weiss[10], where it was assumed that there must be an effective field in a ferromagnetic material, which he called the molecular field. It was thought that this field aligned the neighbouring spins which were parallel to one another. The ensemble of non-interacting spins is subject to thermal agitation, and can be magnetised only if an extremely high magnetic field is applied. Weiss thought that a molecular field could be produced at the site of one spin through the interaction of the neighbouring spins, and that the intensity of the molecular field is proportional to the magnetisation, or

$$H_m = \gamma \times \mathrm{M} \tag{2.3}$$

where γ is the molecular field coefficient, H_m is the molecular field and M is the magnetisation.

The Curie-Weiss law describe the magnetic susceptibility χ of a ferromagnet in the paramagnetic region above the Curie point:

$$\chi = \frac{C}{T - \theta} \tag{2.4}$$

where C is a material-specific Curie constant, T is absolute temperature, measured in kelvins, θ is directly related to the molecular field (because $\theta = \rho\gamma C$, where ρ is the density, and $H_m = \gamma M$. If θ is positive then so is γ, which means that either H_m and M are in the same direction or the molecular field is helping the applied field in magnetising the substance.

When higher than its Curie temperature, T_C (a ferromagnet) becomes paramagnetic, and its susceptibility then follows the Curie-Weiss law, where the value of θ is approximately equal to T_C. The value of θ is therefore large and positive (over 1000K for iron), meaning that the molecular field is coefficient. This fact led Weiss to make the bold and brilliant assumption that a molecular field acts on a ferromagnetic substance when it is both above and below its Curie temperature, and that because this field is so strong, it can magnetise the substance to saturation even when no applied field is present. On such occasions, the substance is self-saturating, or is "spontaneously magnetised". For example, if iron is self-saturating, the explanation previously given regarding the introduction of domains holds. The Weiss theory therefore contains two essential postulates: (1) spontaneous magnetisation; and (2) division into domains. Subsequent developments have shown that the postulates are correct, and that magnetisation is affected by changes of temperature. Figure 2.3 was plotted with ɑ rather than H_m as a variable in order to observe magnetisation behaviour in temperature.

$$\alpha = \frac{\mu H}{kT} \tag{2.5}$$

where μ is the magnetic moment, H is the magnetic field, k is the Boltzmann constant[11], and T is temperature. Following Weiss, let us suppose that the relative magnetisation is given by the Langevin function[12]:

$$\frac{M}{M_0} = \mathrm{L}(\alpha) = \coth(\alpha) - \frac{1}{\alpha} \tag{2.6}$$

When the applied field is zero, this means

$$\alpha = \frac{\mu H_m}{kT} = \frac{\mu \gamma M}{kT} = \frac{\mu \gamma M}{kT}\frac{M_0}{M_0} \tag{2.7}$$

$$\frac{M}{M_0} = \left(\frac{kT}{\mu \gamma M_0}\right)\alpha \tag{2.8}$$

$M/M_0$is therefore a linear function of ɑ with a slope proportional to the absolute temperature. In Figure 2.3[13], curve 1 is the Langevin function and line 2 is a plot of Equation 2.8 for temperature T_2. Their intersection at P gives the spontaneous magnetisation achieved at this temperature, which is expressed as a fraction M_s/M_0 of the saturation magnetisation M_0. An increase in temperature above T_2 has the effect of rotating line 2 anticlockwise about the origin. This rotation causes P and the corresponding magnetisation to move lower and lower on the Langevin curve. The spontaneous magnetisation vanishes at temperature T_3 when the line is in position 3, tangential to the Langevin curve at the origin. T_3 is therefore equal to the Curie temperature Tc. At any higher temperature, such as T_4, the substance is paramagnetic because it is not spontaneously magnetised.

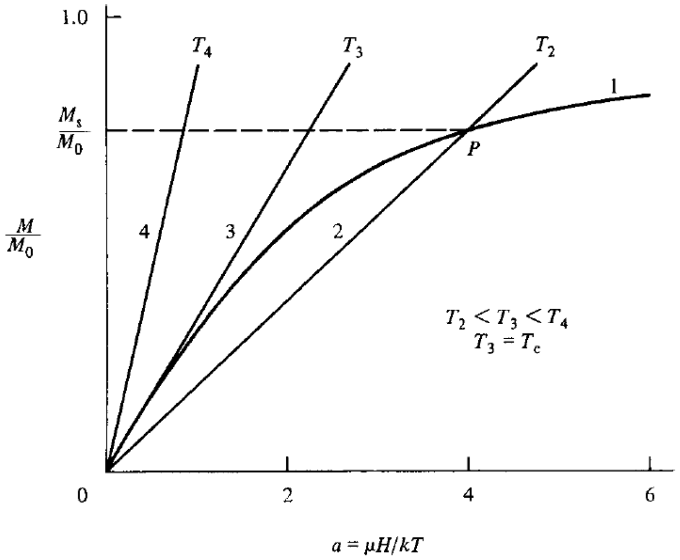

Figure 2.3 Effect of temperature on the value of spontaneous magnetisation. Curve 1 is the Langevin function[13].

The Curie temperature can be evaluated from the fact that the slope of line 3 is the same as the slope of the Langevin curve at the origin, which is $1/3$. Replacing T with T_C results in

$$\frac{kT_c}{\mu\gamma M_0} = \frac{1}{3} \tag{2.9}$$

$$T_c = \frac{\mu\gamma M_0}{3k} \tag{2.10}$$

Therefore, the slope of the straight line representing the molecular field is, at any temperature

$$\frac{kT_c}{\mu\gamma M} = \frac{T}{3T_C} \tag{2.11}$$

However, the slope of the line determines the point of intersection P with the Langevin curve, hence the value of M_s/M_0. Given this, M_s/M_0 is determined solely by the ratio T/T_C. This means that all ferromagnetic materials, which naturally have different values of M_0 and T_C, have the same value of M_s/M_0 for any value of T/T_C. This is known as the law of corresponding states.

This statement of the law is very nearly, but not exactly, correct. In arriving at the Langevin law in Equation 2.6, the number n of atoms per unit volume which is set as $n\mu = M_0$ must be considered. But since n changes with temperature due to thermal expansion, the values of $M = M_0$ at different temperatures are not strictly comparable since they refer to different numbers of atoms. When dealing with magnetisation as a function of temperature, a more natural quantity to use is the specific magnetisation σ, which is the magnetic moment per unit mass, because thermal expansion would then not affect the result.

If n_g is the number of atoms per gram, and $\bar{\mu}$ the average component of magnetic moment in the direction of the field, Equation 2.6 can be written as

$$\frac{n_g\bar{\mu}}{n_g\mu} = \frac{\sigma}{\sigma_0} = \coth(\mathrm{a}) - \frac{1}{\mathrm{a}} \qquad (2.12)$$

If σ_S and σ_0 are then defined as being the saturation magnetisations for a ferromagnetic material at TK and 0K respectively, an exact statement of the law of corresponding states is that all materials have the same value of σ_s/σ_0 for the same value of T/T_C. The relation between the σ and M value is

$$\frac{\sigma_s}{\sigma_0} = \frac{M_s/\rho_s}{M_0/\rho_0} = \frac{M_s\rho_0}{M_0\rho_s} \qquad (2.13)$$

where ρ_s and ρ_0 are the densities at TK and 0K respectively. A change from M to σ also involves a change in the molecular field constant γ.

$$H_m = \gamma M = \gamma\mathrm{\rho}\left(\frac{M}{\mathrm{\rho}}\right) = (\gamma\rho)\sigma \qquad (2.14)$$

Thus (γρ) becomes the molecular field constant, and Equation 2.10 and 2.11 become

$$T_C = \frac{\mu\gamma\rho\sigma_0}{3k} \qquad (2.15)$$

And

$$\frac{kT}{\mu\gamma\rho\sigma_0} = \frac{T}{3T_C} \tag{2.16}$$

Equation 2.8 therefore becomes

$$\frac{\sigma}{\sigma_0} = \left(\frac{kT}{\mu\gamma\rho\sigma_0}\right)\mathrm{a} = \left(\frac{T}{3T_C}\right)\mathrm{a} \tag{2.17}$$

when the magnetisation in expressed in terms of σ.

Experimental data on the variation of the saturation magnetisation σ_s of Fe, Co, and Ni with temperature are shown in figure 2.4[14]. The temperature scales shown in figure 2.5[15] provide the Curie points and the temperatures of phase changes and recrystallization for the three metals. The recrystallization temperatures are the approximate minimum temperatures at which heavily cold-worked specimens recrystallise. It therefore follows that iron and cobalt can be recrystallised while still ferromagnetic but nickel cannot.

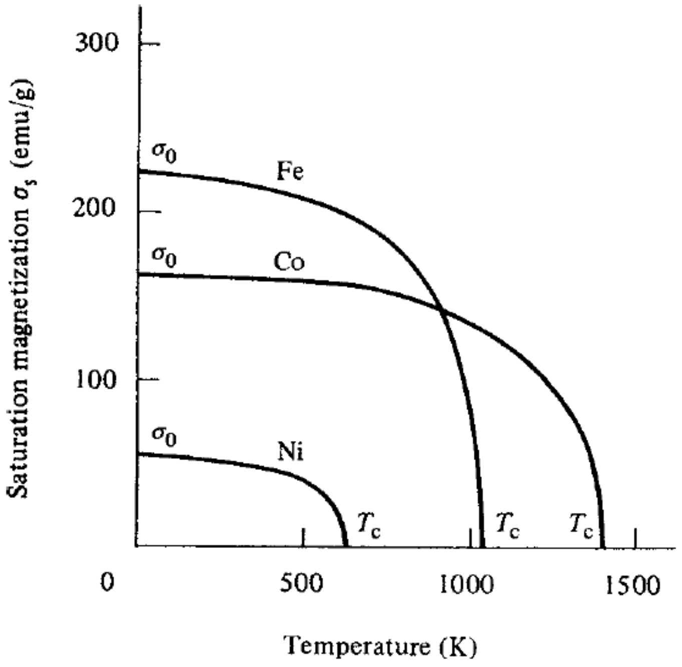

Figure 2.4 Saturation magnetisation of iron, cobalt and nickel as a function of temperature[14].

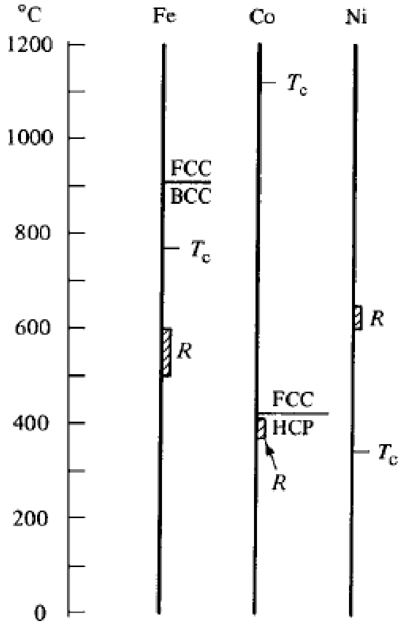

Figure 2.5 Curie points (T_C), recrystallisation temperatures [R], and phase changes in Fe, Co, and Ni. BCC = body-centred cubic; FCC = face-centred cubic; HCP = hexagonal close packed. Ni is FCC at all temperatures[15].

The Weiss theory of the molecular field says nothing about the physical origin of this field. However, the hypothesis that H_m is proportional to the existing magnetisation implies that the phenomenon involved is cooperative. This suggests that the greater the degree of spin alignment in a crystal's region, the greater the force tending to align any one spin in that region.

It was not until 1928 that the physical origin of the molecular field was understood, when Heisenberg[16] showed it was caused by exchange interaction. A year or so earlier, new wave mechanics had been applied to the problem of the hydrogen molecule, i.e., the problem of explaining why two hydrogen atoms come together to form a stable molecule. Each of these atoms consists of a single electron moving about the simplest kind of nucleus, i.e. a single proton. For a particular pair of atoms, situated at a certain distance apart, there are certain electrostatic attractive forces (between the electrons and protons) and repulsive forces (between the two electrons and between the two protons) which can be calculated using Coulomb's law. However, there remains another force, entirely non-classical, which depends on the relative orientation of the spins by the two electrons. This is the exchange force. If the spins are antiparallel, the sum of all the forces is attractive and a stable molecule is formed. In such cases, the total energy of the atoms is then less for a particular distance of separation than it is for smaller or larger distances. If the spins are parallel, the two atoms repel one another.

The exchange interaction is a consequence of the Pauli exclusion principle, applied to the two atoms. This principle states that two electrons can have the same energy only if they have opposite spins. This means that two hydrogen atoms can come so close together that their two electrons have the same velocity and occupy very nearly the same small region of space (i.e. they have the same energy) provided these electrons have opposite spin. If their spins are parallel, the two electrons will tend to remain far apart. The ordinary (Coulomb) electrostatic energy is therefore modified by the spin orientations, which means that the exchange force is fundamentally electrostatic in origin.

The term “exchange” arises as follows. When the two atoms are adjacent, electron 1 can move about proton 1, and similarly electron 2 about proton 2. Electrons, however, are indistinguishable, and so the possibility that the two electrons exchange places must also be considered, whereby electron 1 can move about proton 2 and similarly electron 2 about proton 1. This consideration introduces an additional term – the exchange energy – into the expression for the total energy of the two atoms. This interchange of electrons takes place at a very high frequency, approximately 10^{18} times per second in the hydrogen molecule.

The exchange energy forms an important part of the total energy of many molecules and the covalent bond in many solids. Heisenberg showed that it also plays a decisive role in ferromagnetism. If two atoms i and j have spin angular momentum $S_i h/2\pi$ and $S_j h/2\pi$ respectively, then the exchange energy between them is given by

$$E_{ex} = -2J_{ex}S_iS_j = -2JS_iS_j\cos\Phi \tag{2.18}$$

where E_{ex} is the value of exchange energy, J_{ex} is a particular integral known as the exchange integral, which occurs in the calculation of the exchange effect, and f is the angle between the spins. If J_{ex} is positive, the minimum value of E_{ex} is found when the spins are parallel (cos Φ = 1) and the maximum when they are antiparallel (cos Φ = -1). If J_{ex} is negative, the lowest energy state results from antiparallel spins. As has already been seen, ferromagnetism arises due to the alignment of spin moments on adjacent atoms. Given this, it is a necessary condition for the exchange interval to have a positive value for ferromagnetism to occur. However, since J_{ex} is commonly negative (as in the hydrogen molecule), this is a rare condition.

According to Weiss' theory, ferromagnetism is caused by a powerful "molecular field" which aligns the atomic moments. In modern nomenclature, this would be described as "exchange forces" causing the spins to be parallel, although it would be incorrect to conclude that this terminological change has removed all the mystery from ferromagnetism. The step from a hydrogen molecule to a crystal of iron is enormous, and the problem of calculating the exchange energy of iron is so formidable that it has yet to be solved. Expressions such as Equation 2.18, which is itself something of a simplification and applies only to two atoms, must be calculated using all the atom pairs in the crystal. Exchange forces decrease rapidly with distance, meaning that some simplification is possible by restricting the calculation to nearest-neighbour pairs; this simplification, however, does not yield an exact solution of the problem. As such, given the existing state of knowledge, it is impossible to make predictions from first principles.

Nevertheless, the knowledge that exchange interaction is responsible for ferromagnetism and, as argued below, similarly for antiferromagnetism and ferrimagnetism, has resulted in many conclusions of significant value. For example, it has been possible to rationalise the appearance of ferromagnetism in some metals and not in others. The curve of Figure 2.6, usually called the Bethe–Slater curve[17], shows the postulated variation of the exchange integral with the ratio r_a/r_{3d}, where r_a is the radius of an atom and r_{3d} is the radius of its 3d shell of electrons. In passing, it should be noted that the immediate cause of ferromagnetism in Fe, Co, and Ni is the spin alignment of some of the 3d electrons. The diameter of the atom is $2r_a$, which is also the distance between the centres of the atoms since the atoms of a solid are regarded as being in contact with one another. If two atoms of the same kind are brought increasingly close together without any change in the radius r_{3d} of their 3d shells, the ratio r_a/r_{3d} decreases. When this ratio is large, J_{ex} is small and positive. As the ratio decreases and the 3d electrons approach one another more closely, the positive exchange interaction, which favours parallel spins, becomes stronger before decreasing to zero. A further decrease in the interatomic distance brings the 3d electrons so close together that their spins inevitably become antiparallel (negative J_{ex}), a condition which is called antiferromagnetism.

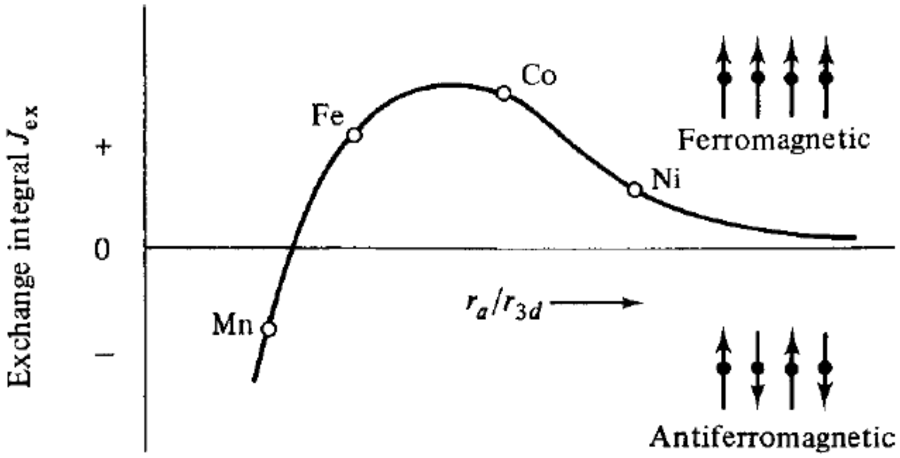

Figure 2.6 Bethe-Slater curve[17].

The curve in Figure 2.6 can be applied to a series of different elements if r_a/r_{3d} is computed from their known atom diameters and shell radii. The resultant points which are found lie on the curve as shown. The curve also correctly separates Fe, Co, and Ni from Mn and the subsequent lighter elements in the first transition series. It should be noted that Mn is antiferromagnetic below 95K, and Cr, the next lighter element, is antiferromagnetic below 37°C; above these temperatures both are paramagnetic. When

J_{ex} is positive, its magnitude is proportional to the Curie temperature (see below) because spins which are held parallel to each other by strong exchange forces can be disordered only by large amounts of thermal energy. The positions of Fe, Co, and Ni on the curve concur with the notion that of the three, Co has the highest and Ni the lowest Curie temperature.

2.2.2 Antiferromagnetism

Antiferromagnetic substances have a small positive susceptibility at all temperatures, but their susceptibilities vary in a peculiar way with temperature. Chiefly it was Néel, in a series of paper beginning in 1932[18], who developed the theory of antiferromagnetism by applying the Weiss molecular field theory to the problem.

The way in which the susceptibility of an antiferromagnetic varies with temperature is shown in figure 2.7[19]. As the temperature decreases, χ increases but reaches its maximum at a critical temperature, T_N, which is known as the Néel temperature. The substance is paramagnetic above T_N and antiferromagnetic below it. T_N often lies far below room temperature, which means that it may be necessary to carry susceptibility measurements down to quite low temperatures in order to discover if a given substance which is paramagnetic at room temperature is antiferromagnetic at some lower temperature. Most, but not all, antiferromagnetics are ionic compounds – oxides, sulphides, chlorides, and the like – and a very large number are known, which makes them much more common than ferromagnetics.

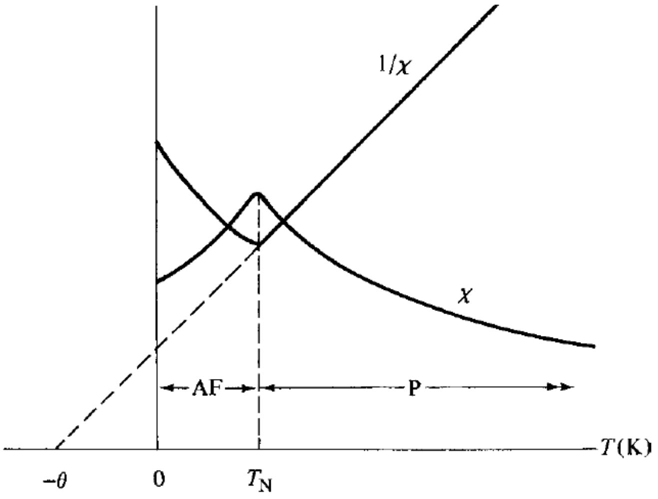

Figure 2.7 Temperature dependence of susceptibility χ and inverse susceptibility $1/\chi$ for an antiferromagnetic material. AF = antiferromagnetic, P = paramagnetic[19].

Figure 2.7 shows that a plot of $1/\chi$ vs T is a straight line above T_N, and that this line extrapolates to a negative temperature at $1/\chi = 0$. The equation of the line is

$$\frac{1}{\chi} = \frac{T+\theta}{C} \tag{2.19}$$

or

$$\chi = \frac{C}{T+\ \theta} = \frac{C}{T-(-\theta)} \tag{2.20}$$

In other words, it can be said that the material obeys the Curie–Weiss law, but with a negative value of θ. Since θ is proportional to the molecular field coefficient γ, the molecular field H_m, in the paramagnetic region, is opposed to the applied field H. Whereas H acts to align the ionic moments, H_m acts to dis-align them. When viewed on a very localised scale, the molecular field shows that any tendency for an ionic moment to point in one direction is immediately counteracted by a tendency for the moment on an adjacent ion to point in the opposite direction. In other words, the exchange force is negative. Furthermore, when below the critical temperature T_N, this tendency towards an antiparallel alignment of moments is strong enough to act even in the absence of an applied field because the randomising effect of thermal energy is so low. The lattice of magnetic ions in the crystal subsequently breaks into two sublattices, designated A and B, the moments of which are more or less opposed. The tendency toward anti-parallelism becomes stronger as the temperature is lowered below T_N. Upon reaching 0K, the antiparallel arrangement is perfect, as shown in Figure 2.8[20, 21]. Only the magnetic metal ions are presented here since at this stage other ions (such as oxygen or sulphur) are nonmagnetic and do need not be considered.

Thus, it can now be seen that at 0K an antiferromagnetic consists of two interpenetrating and identical sublattices of magnetic ions. Each spontaneously magnetised to saturation in the zero-applied field, in opposite directions, just as the single lattice of a ferromagnetic is spontaneously magnetised. It can be deduced that an antiferromagnetic has no net spontaneous moment and can acquire a moment only when a strong field is applied, and further that the Néel temperature T_N plays the same role as the Curie temperature T_C in that each divides the temperature scale into a magnetically ordered region below and a disordered (paramagnetic) region above. Thus, several similarities to ferromagnetism are apparent, meaning that the descriptive term “antiferromagnetism” is entirely appropriate.

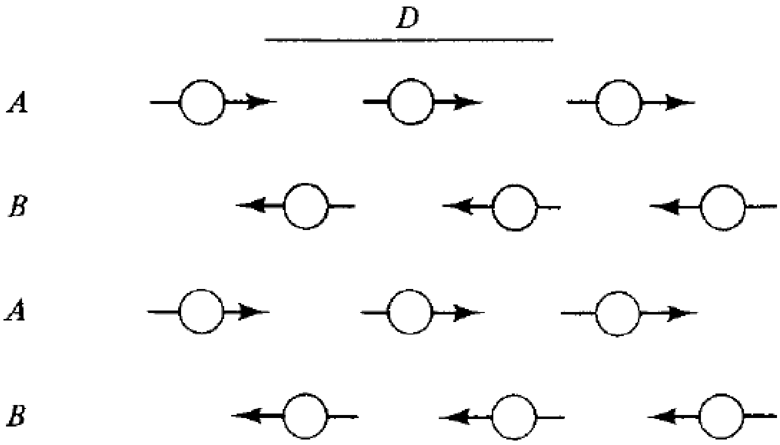

Figure 2.8 Antiferromagnetic arrangement of A and B sublattices[20, 21].

2.3 Magnetic Anisotropy

One factor which may strongly affect the shape of the M-H curve and indeed the shape of the hysteresis loop, is magnetic anisotropy. This term simply means that the magnetic properties depend on the direction in which they are measured. This subject is of considerable practical interest because anisotropy is exploited in the design of most magnetic materials of commercial importance. As such, a thorough knowledge of anisotropy is important to fully understand these materials. There are several kinds of anisotropies, namely:

1. Magnetocrystalline anisotropy (crystal anisotropy);
2. Shape anisotropy;
3. Stress anisotropy;
4. Anisotropy induced by:
    a. Magnetic annealing;
    b. Plastic deformation;
    c. Irradiation.
5. Exchange anisotropy;
6. Magnetic elastic anisotropy

Of these, only magnetocrystalline anisotropy is intrinsic to the material, meaning that, strictly speaking, all the others are extrinsic or “induced.” All the anisotropies identified above (with the exception of 4c) are important in practice, and any one may become predominant in particular circumstances. In this section, only magnetocrystalline and shape anisotropy will be considered.

2.3.1 Magnetocrystalline Anisotropy

A ferromagnetic crystal exhibits different behaviour depending on the direction along which it has been magnetised. This effect indicates that different crystalline directions are not magnetically equivalent, something which can be observed in magnetisation curves by applying an external field along different directions. The results for iron, which has a body-cantered cubic (BCC) structure, are shown in Figure 2.9.

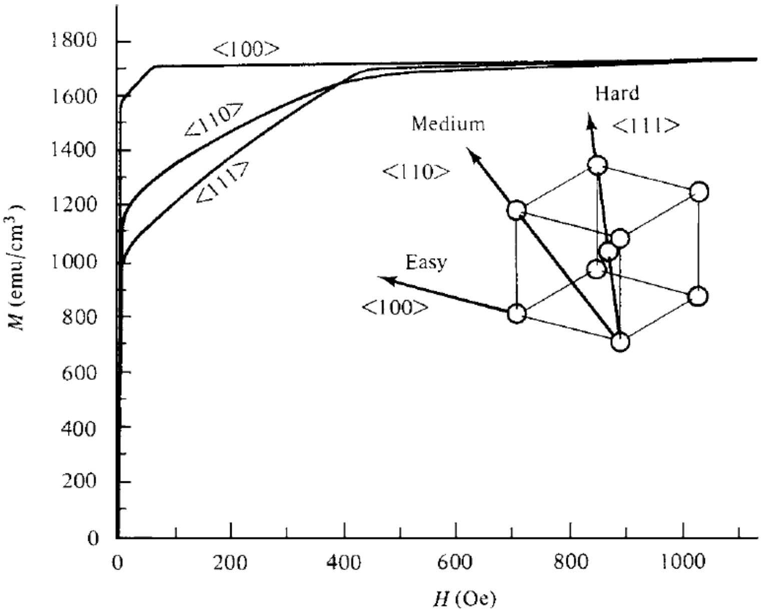

Figure 2.9 Magnetisation curves for single crystals of iron[22].

Iron measurements show that saturation can be achieved with relatively low fields in the ⟨100⟩ direction. Accordingly, this is known as the "easy direction" of magnetisation, and tells us something about domains in iron in their demagnetised state. As discussed below, a domain wall separating two domains in a crystal can be moved by a small applied field. Were domains in demagnetised iron spontaneously magnetised to saturation in directions of the form ⟨100⟩, then a possible domain structure for a demagnetised crystal disk cut parallel to (001) would be that shown in Figure 2.10 (a). Here are shown four kinds of domains, which are magnetised parallel to four of the six possible easy directions, namely, [010], [100], [0$\bar{1}$0], and [$\bar{1}$00].

Were this the case, it would still be true that all these domains would be of only four kinds, namely those with M_S vectors in the [010], [100], [0$\bar{1}$0], and [$\bar{1}$00] directions. If a field H is now applied in the [010] direction, the [010] domain will grow in volume by the mechanism of domain-wall motion, as indicated in Figure 2.10 (b). It does so because the magnetic potential energy of the crystal is lowered. A continued application of the field eliminates all but the favoured domain, and the crystal is now saturated (Figure 2.10 (c)). This has been accomplished simply by applying the low field required for domain wall motion. Since the experiment shows that only a low field is needed to saturate iron in a $\langle 100 \rangle$ direction, it can be concluded that the domain structure postulated is essentially correct and that, more generally, the direction of easy magnetisation of a crystal is the direction of spontaneous domain magnetisation in a demagnetised state.

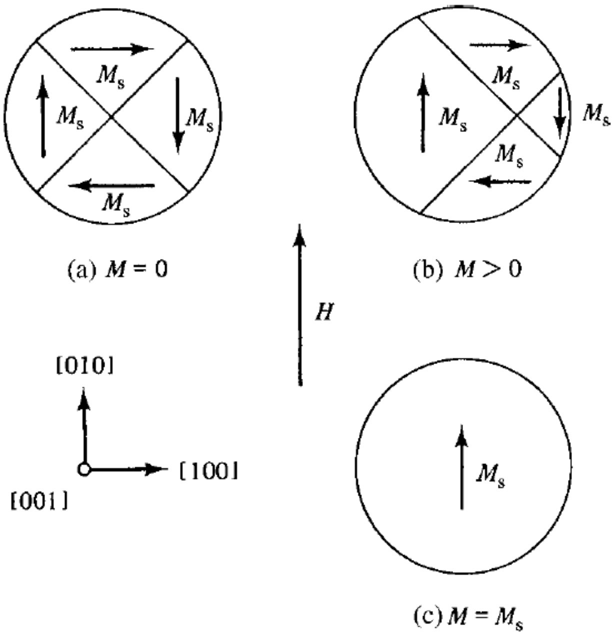

Figure 2.10 Domain structure in a single-crystal disk of iron. The field H is applied in the [010] direction[23].

Figure 2.11 shows the domain structure changes within a field saturating iron in a $\langle 110 \rangle$ direction. In a low field, domain wall motion occurs until there are only two domains left (Figure 2.11 (c)), each with the same potential energy. The only way in which the magnetisation can increase further is through the rotation of the M_S vector of each domain until it is parallel with the applied field. This process is called domain rotation. The domain itself, which is a group of atoms, does not rotate; rather, it is the net magnetic moment of each atom which rotates. Domain rotation occurs only in high fields because in this situation the field is then acting against the force of crystal anisotropy, which is usually fairly strong. Crystal anisotropy may therefore be regarded as a force which tends to hold the magnetisation in certain equivalent crystallographic directions in a crystal. When the rotation process is complete (Figure 2.11(d)), the domain wall in Figure 2.11 (c) disappears and the crystal is saturated.

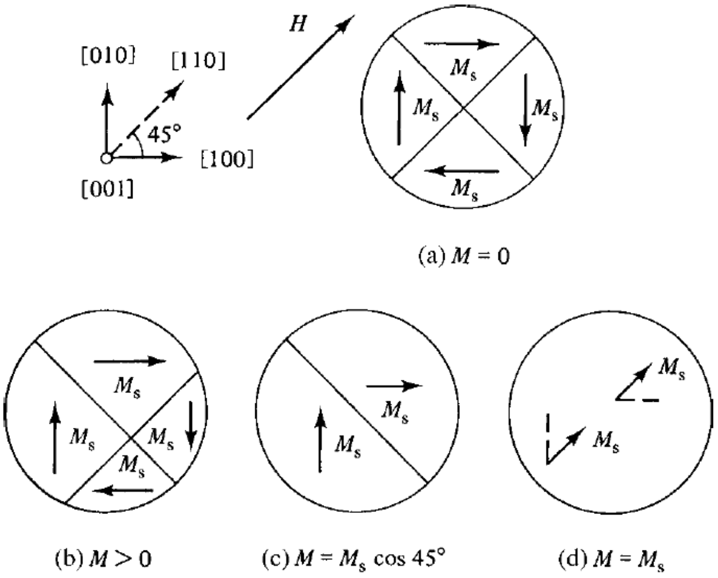

(a) $M = 0$

(b) $M > 0$ (c) $M = M_s \cos 45°$ (d) $M = M_s$

Figure 2.11 Domains structure in a single crystal of iron. The field H is applied in the [110] direction[24].

Given that the applied field must work against the anisotropy force in order to turn the magnetisation vector away from an easy direction, it must be the case that energy stored in any crystal in which M_S points in a noneasy direction. This is known as crystal anisotropy energy E, which the Russian physicist Akulov demonstrated in 1929 could be expressed in terms of a series expansion of the direction cosines of M_S relative to the crystal axes[25, 26]. In a cubic crystal, let M_S make angles a, b, c with the crystal axes, and let $\alpha_1,\ \alpha_2,\ \alpha_3$ be the cosines of these angles, which are called direction cosines. Then

$$\mathrm{E} = K_0 + K_1\,(\alpha_1^2\alpha_2^2 + \alpha_2^2\alpha_3^2 + \alpha_3^2\alpha_1^2) + K_2(\alpha_1^2\alpha_2^2\alpha_3^2) + \cdots \tag{2.21}$$

where K_0, K_1, K_2, . . . are constants for a particular material at a particular temperature, and can be expressed in erg/cm^3 or J/m^3. Higher powers are generally not needed, and indeed K_2 is sometimes so small that the term using it can be neglected. The first term, K_0, is independent of angle and usually ignored because generally speaking only the change in the energy E when the M_S vector rotates from one direction to another is relevant. The in-plane uniaxial magnetic anisotropy and the surface magnetic anisotropy included in the magnetocrystalline anisotropy are now introduced.

In-Plane Uniaxial Magnetic Anisotropy

Strain, oblique deposition, and in-situ magnetic field during growth may induce an in-plane uniaxial anisotropy in a thin film sample. It can be seen in magnetisation curves that a smaller field is required to saturate the sample along one in-plane direction than along others. The axis along which the sample is easily saturated is called the easy in-plane uniaxial axis, while the axis along which the sample is difficult to saturate is called the hard in-plane uniaxial axis. The energy of the in-plane uniaxial anisotropy has the form

$$E_u = -K_u cos^2(\theta_K - \theta) \tag{2.22}$$

where K_u is the uniaxial anisotropy constant, θ_k is the angle between the easy in-plane uniaxial anisotropy axis and the static field H**,** and θ is the angle between M and H. In a bulk material, the magnetisation tends to lie along certain crystallographic axes due to the spin-orbit interaction.

Surface Magnetic Anisotropy

A typical expression for the dominant anisotropy energy in thin film is

$$\mathrm{E} = -\mathrm{K}\, cos^2\theta \tag{2.23}$$

where E is the orientation-dependent energy of the magnetisation, θ is the angle between the magnetisation and the normal of the film, and K is an anisotropy constant[23, 27]. K is positive when the magnetisation prefers to be perpendicular to the plane of film. The second-order uniaxial term $K_2\cos^4\theta$ is usually very small. In order to distinguish the contributions from the surface or interface from the volume or bulk, K_S is defined as surface anisotropy energy per unit area, while K_V is defined as volume anisotropy energy per unit volume. For a magnetic layer where its thickness *t* is much smaller than its exchange length, the average magnetic anisotropy energy can be written as

$$K_{eff} = K_V + 2\,K_S/t \tag{2.24}$$

Equation (2.24) is often used when analysing experiments, and K_V and K_S can be obtained by plotting the product K_t versus thickness *t*. Below a certain thickness, the surface anisotropy contribution outweighs the volume anisotropy contribution, which results in perpendicular magnetisation.

2.3.2 Shape Anisotropy

Due to long-range dipole interaction, shape anisotropy senses the outer boundaries of the sample. It is the main contribution to K_V in equation (2.24). Shape effect can be described via a demagnetising field. For a thin film, the corresponding anisotropy energy per unit volume is

$$E_d = 2\pi M_s^2 cos^2\theta \tag{2.25}$$

where θ is the angle between the magnetisation and the normal of the film[28]. As shown in equation (2.25), this contribution favours an in-plane magnetisation rather than a perpendicular one, and is independent of thickness This means that this anisotropy energy only contributes to K_V.

2.4 Fe/GaAs and Fe/InAs systems

The growth of epitaxial FM/SC hybrid structures was first demonstrated in Fe/GaAs by Prinz's group in the Naval Research Laboratory[29]. In part, this is likely due to the fact that the lattice constant of bcc Fe (2.866 Å) is almost exactly half that of GaAs (5.654 Å). Since then, Fe/GaAs has continued to be a model system for the epitaxial growth of FM metals on SCs. Another interesting system is the Fe/InAs hybrid structure, in which metals on narrow gap SCs, such as InAs which has a direct bandgap as small as 0.36 eV at room temperature (RT), form low resistance contacts[30]. Although the lattice mismatch of Fe and InAs (6.058 Å) at 5.4% is much larger than that of Fe/GaAs (1.3%), high-quality bcc Fe has been demonstrated on InAs (001) by Xu *et al.*[31].

Molecular-beam epitaxy (MBE) is the most commonly used growth technique to synthesise high-quality hybrid FM/SC structures. It is crucial that there is clean and well-ordered SC substrate prior to the growth. As regards the FM/SC systems discussed below, typical substrate cleaning procedures include *ex-situ* chemical cleaning followed by in-situ thermal annealing, with or without argon ion sputtering. Alternatively, to have a well-ordered surface with a specific reconstruction, it is also common to use substrates with an As capping layer; in such cases, the surface reconstructions tend to be controlled by the annealing temperatures[32]. In many earlier studies, the FM layers were grown at elevated temperatures of around 470–500 K. This high temperature growth usually ended up with the formation of a magnetic dead layer at the hybrid interface. In order to reduce – or even eliminate – the intermixing of Fe with Ga, In, or As at the interface, Xu *et al.* were able to demonstrate the epitaxial growth at room temperature (RT).

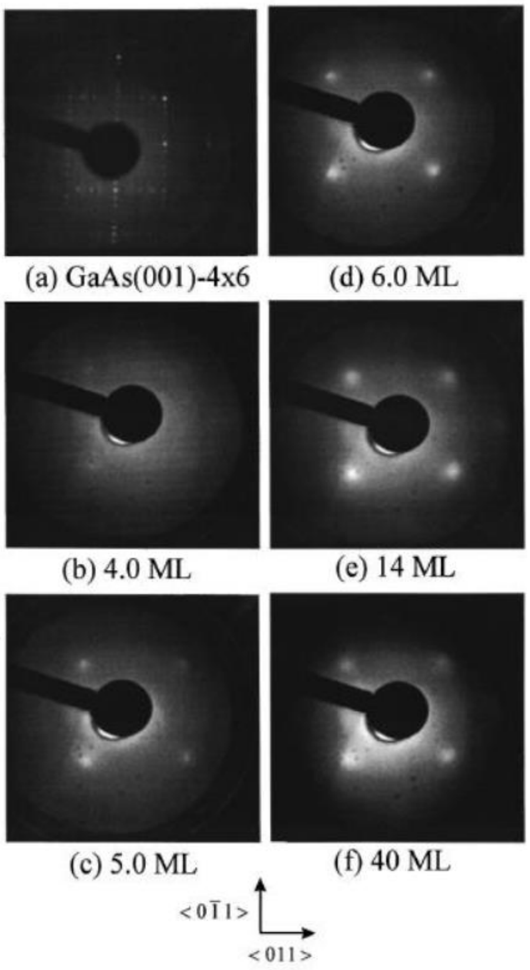

(a) GaAs(001)-4x6

(d) 6.0 ML

(b) 4.0 ML

(e) 14 ML

(c) 5.0 ML

(f) 40 ML

Figure 2.12 LEED patterns of GaAs (001)-(4×6) substrate after As desorption and Fe deposition at room temperature[33].

Growth processes are usually monitored in-situ by either reflection high-energy electron diffraction (RHEED) or low-energy electron diffraction (LEED). Figure 2.12 shows the LEED patterns of Fe/GaAs (001) following the deposition of Fe at RT[33]. These LEED observations demonstrate that the Fe grows epitaxially on GaAs (001) at RT with an epitaxial relationship of Fe(001)<100>||GaAs(001)<100>, and that the lack of Fe LEED patterns for the first 4 ML suggests a 3D Volmer-Weber growth mode. The epitaxial growth of Fe/InAs, as monitored by LEED, indicates an epitaxial relationship of Fe(001)<001>||InAs(001)<001>, similar to that of the Fe/GaAs(001)[34].

The most distinctive feature of a clean SC surface is the formation of a variety of reconstructions and associated atomic scale structures[35-37]. To demonstrate how these atomic scale structures affect the lattice relaxation, the epitaxial growth in Fe/InAs(001)-(4×2) has been studied in detail, using dynamic RHEED, by Xu *et al.*[34].

Zega *et al*. compared the atomic structures of two types of Fe/AlGaAs interface using high-resolution transmission electron microscopy (TEM) (see Figure 2.13): one for an as-grown interface showing an injected spin polarisation of 18% in a full spin-LED device structure, and the other for an annealed interface exhibiting an improved spin polarisation of 26%[38]. An interfacial region ~0.7 nm thick with some disorders was identified for the as-grown sample, whereas the annealed interface was thinner (~0.5 nm) and had no distinguishable disorder. Further measurements using high-angle annular-dark-field microscopy indicated the existence of an atomic layer of intermixed Fe and As for the annealed interface. Through density functional theory (DFT) calculations, it was suggested that the mild annealing step could sharpen the Fe/GaAs interface, which was attributed to a restructuring of the interface into a lower-energy state, thereby reducing the extent of the mixing. LeBeau *et al.*[39] and Fleet *et al.*[40-42] also reported several other types of interfacial atomic structures for the Fe/GaAs system.

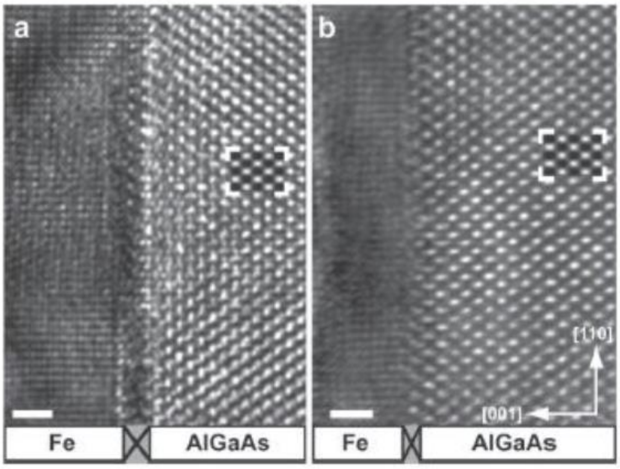

Figure 2.13 High-resolution TEM images of an Fe/AlGaAs spin-LED structure. (a) As-grown, and (b) post-annealed at 500 K for 10 minutes. Scale bar is 1.0 nm[42].

Many researchers have reported the high-quality epitaxial growth of Fe on GaAs, where they have contributed to the long-lasting debate over the presence of a magnetic dead layer at the Fe/GaAs interface[43]. This detrimental effect was historically attributed to the formation of antiferromagnetic Fe_2As[44] and half-magnetised $Fe_3Ga_{2x}As_x$[43] in the vicinity of the interface, until a bulk-like magnetic moment of RT-grown Fe on GaAs (001)-(4 × 6) and its corresponding magnetic phase evolution[33] (see Figure 2.14) were demonstrated. The former result was further confirmed with unambiguous X-ray magnetic circular dichroism (XMCD) down to the ML regime[45].

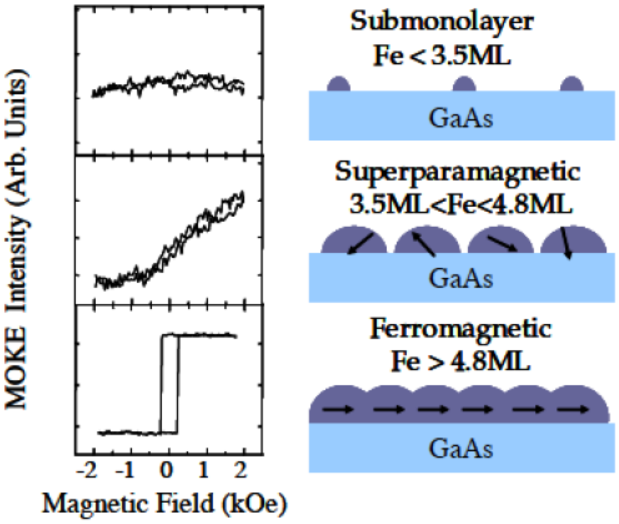

Figure 2.14 Evolution of the magnetic phase of Fe/GaAs, corresponding to the growth morphology[33].

Another open issue over the past two decades concerns the origin of uniaxial magnetic anisotropy (UMA), unexpected based on the crystal symmetry of bcc Fe. It was first observed in the Fe/GaAs (001). The evolution of the hysteresis loops of Fe/GaAs (001)-(4 × 2) and Fe/InAs(001)-(4 × 2) are shown in Figure 2.15[46], where the Fe films grown on both substrates show the existence of UMA, dominating the global magnetic anisotropy in the ultrathin regions. However, when above the critical thickness of about 50 ML for Fe/GaAs and 16 ML for Fe/InAs, cubic anisotropy takes over.

There are three possible mechanisms responsible for the UMA observed in Fe/GaAs and Fe/InAs: (1) shape anisotropy, since the films show 3D island growth; (2) intrinsic anisotropy due to the unidirectional nature of Fe-As, Fe-Ga and Fe-In bonds; (3) magnetoelastic interactions due to strain in the ultrathin epitaxial films caused by lattice mismatch. STM study shows no evidence of shape anisotropy due to 3D island growth[34]. The so-called ‘nearly half-magnetised’ phase at the interface can also be excluded since this phase does not exist in the samples grown at RT[33]. It is now generally believed that the atomic scale structure related to the SC surface is responsible for this UMA.

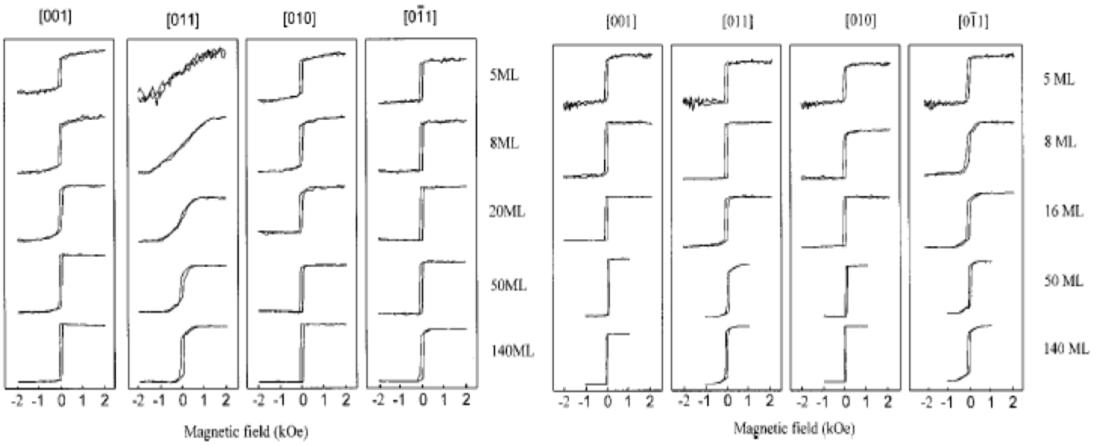

Figure 2.15 MOKE hysteresis loops of Fe/GaAs (001)-(4×2)(left panel) in the thickness range of 5 to 140 ML grown at RT with the magnetic field applied along four major axes, and that of Fe/InAs (001)-(4×2)(right panel)[46].

Based on an examination of magnetic anisotropy of the Fe films deposited on GaAs substrates with different reconstructions, Kneedler *et al.* proposed that the unidirectional nature of Fe-As or Fe-Ga bonds is responsible for the UMA[47]. This might be understood as a “chemical” effect, in which the electronic structure of the Fe atoms near the interface differs distinctly from “normal” bcc Fe. Measurements of the thickness dependence of the anisotropies in Fe/GaAs by Brockmann *et al.*

demonstrated that the UMA is a pure interface term which originates exclusively from the Fe/GaAs interface. This favours the picture of “unidirectional chemical bonding” at the interface[48]. In another study, Tivakornsasithorn *et al.* reported the epitaxial Fe films on GaAs, ZnSe, and Ge, and their results seem to suggest that by controlling surface reconstructions of the semiconductor substrates, it is possible to engineer magnetic anisotropy in the magnetic over-layers[28].

2.5 CoFeB system

CMOS is currently the dominating technology for logic circuits, allowing for fast and powerful microprocessors [49]. However, it is quickly approaching its scaling limits due to increased problems with power dissipation at scaled technology nodes. In this context, the next-generation memory device is required allowing for continued scaling with improved energy efficiency by eliminating static power dissipation. The integration of a fast, energy-efficient non-volatile memory technology with CMOS can help alleviate this problem [50]

The most important three kinds of memories in the memory hierarchy are static random-access memories (SRAM), dynamic random-access memories (DRAM) and NOR Flash. SRAM, it the fastest of the three, but is volatile with a very low density. DRAM has a higher density compared with SRAM, but it is also volatile and needs periodic refresh, which results in power consumption. The NOR flash memories have the highest density among the three and are non-volatile. However, they have very slow write speed and very limited endurance. They also use high power for writing data and high internal voltages are needed for their operation.

Spintronic devices, which exploit the exchange interaction of the electron spins, where magnetic and transport properties are coupled, are strong candidates for non-volatile memory due to the inherent hysteresis in ferromagnetic materials, and the compatibility of some of these materials with the standard CMOS process [51-53]. Magnetoresistive

RAM (MRAM) has exhibited significant advantages as a fast, fairly low-power, high-endurance, radiation-resistant non-volatile memory, which can be integrated to the CMOS as a back-end of line (BEOL) process [54]. The read-out process of the MRAM bits is reliably performed via the tunnelling magnetoresistance (TMR) effect [55, 56] in magnetic tunnel junctions (MTJs). As for the writing process, the first generations of MRAM utilized the Oersted fields generated by running currents in adjacent conducting lines of memory cells to switch the magnetization. The latest technology to switch magnetization of MRAM bits using spin-polarized currents via the spin transfer torque (STT) effect [57, 58] , has a better performance in terms of energy efficiency, scalability and density compared with Oersted fields.

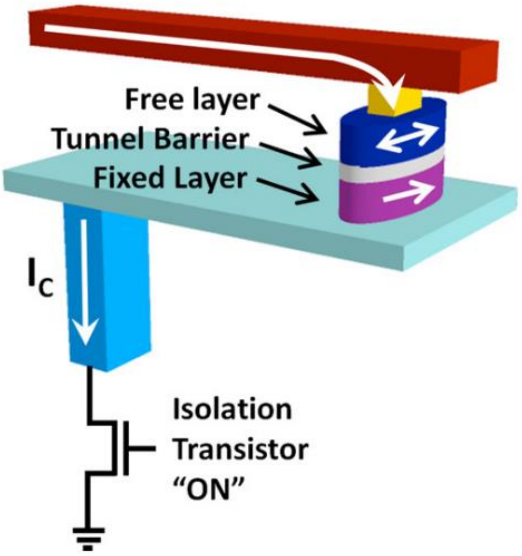

Figure 2.16 Typical architecture for a 1 transistor-1 MTJ (1T-1R) memory cell. The MTJ is composed of a bi-stable free layer and a pinned layer separated by a tunnelling oxide. The device is fabricated as part of the back-end (BEOL) process, compatible with CMOS logic processes [50].

Figure 2.16 shows a typical simplified STT-RAM structure which consists of a free layer which can take two states (parallel or antiparallel) to a pinned (fixed) layer. Both of the layers are separated by a tunnelling oxide, which is usually MgO to allow for read-out via the TMR effect [54, 59]. The writing process is performed by passing a spin-polarized current, which transfers some of its momentum to the nanomagnet, inducing a torque that can result in switching depending on the direction of the current.

The magnetization of the magnetic layers can be either in-plane (IP) or perpendicular to the plane (PP). The simplest and most studied IP and PP STT-MRAM designs are sketched in figure 2.17.

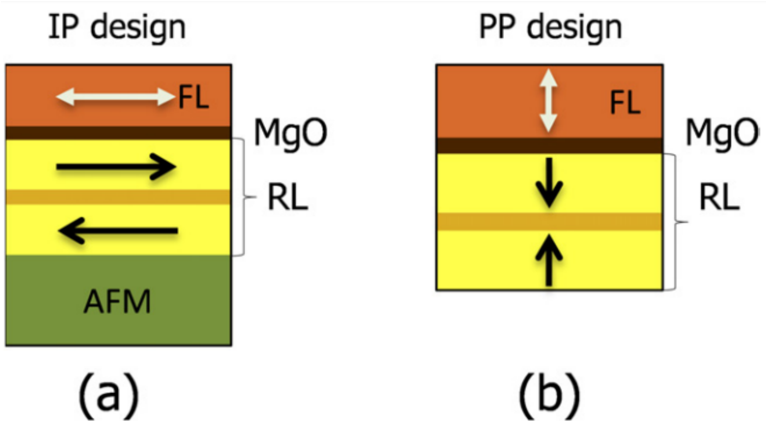

Figure 2.17 (a) In-plane and (b) perpendicular STT-MRAM cell designs [60].

For the in-plane configuration, the switching current density is given by [61]

$$J_{c0} = \left(\frac{2e\alpha M_s t}{\hbar\eta}\right)\left(H_k + \frac{H_d}{2}\right), \tag{2.26}$$

where α is the free layer Gilbert damping factor, η is the spin-transfer efficiency, M_s and t are the free layer saturation magnetization and thickness, H_k is the in-plane shape-induced anisotropy field and H_d is the out-of-plane demagnetizing field. Scaling of STT devices generally requires a trade-off between the switching current density J_{c0} and the thermal stability factor Δ, where the goal is to minimize the ratio J_{c0}/Δ while preserving a given goal for the thermal stability factor. Specifically, the switching current to thermal stability figure of merit is given by

$$\frac{I_{c0}}{\Delta} = (4e\alpha kT/\hbar\eta)(1 + H_d/2H_k), \tag{2.27}$$

Where it can be observed that the switching current is dominated by the out-of-plane demagnetizing field H_d, which typically does not determine the thermal stability, given that $H_k \ll H_d$.

CoFeB is the most studied material for MTJ structures due to its high MR value [62] and low Gilbert damping [63]. The value of TMR effect has been reported as high as $138\% \sim 604\%$ [62, 64-66] in the CoFeB/MgO/CoFeB pseudo-spin-valve MTJ. However, all of these CoFeB-based MTJ is of in-plane configuration. If the perpendicular anisotropy creates an anisotropy field $H_{k\perp}$, the switching current over thermal stability ratio can become much smaller

$$\frac{I_{c0}}{\Delta} = (4e\alpha kT/\hbar\eta)(1 + (H_d - H_{k\perp})/2H_k), \tag{2.18}$$

If the perpendicular anisotropy of the free and fixed layers are large enough to overcome their respective demagnetizing fields (i.e. $H_{k\perp} > H_d$), the magnetizations of the layers become perpendicular, giving rise to a fully perpendicular configuration. In this configuration, the demagnetizing field is fully cancelled and therefore, the switching current density would be given by $J_{c0} = 2e\alpha M_s H_k t/\hbar\eta$, while the switching current over thermal stability figure of merit will be given by

$$\frac{I_{c0}}{\Delta} = 4e\alpha kT/\hbar\eta\,. \tag{2.19}$$

Recently, a significant interface-induced perpendicular anisotropy has been observed in CoFeB/MgO junctions while keeping large TMR values while the CoFeB thickness is very thin [67]. This exciting discovery satisfy high thermal stability at reduced dimension, low-current current-induced magnetization switching and high tunnel magnetoresistance ratio all at the same time. The key to achieve a perpendicular-anisotropy CoFeB/MgO MTJ is the very thin thickness of CoFeB layer as seen in Figure 2.18. The PMA was attributed entirely to the CoFeB-MgO interfacial anisotropy in ref. [67], while the Ta seed layer, not just the MgO at the top interface, is demonstrated to be critical to achieving perpendicular magnetic anisotropy [68]. The origin of the PMA in CoFeB/MgO structure is far from clear and this is why this topic is still of widely interest.

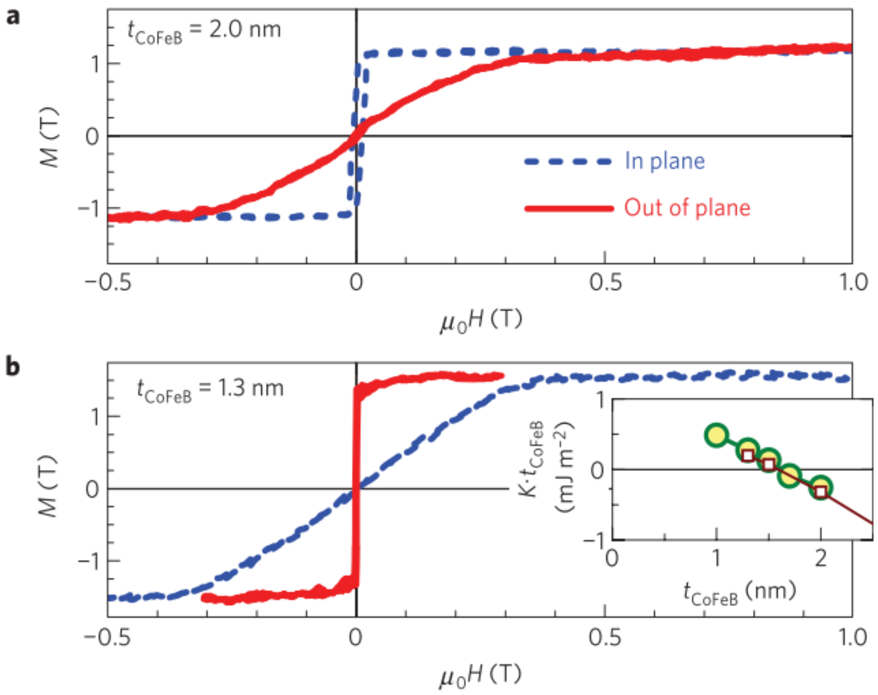

Figure 2.18 In-plane and out-of-plane magnetization curves for CoFeB/MgO. (a), thickness of CoFeB=2.0 nm. (b), thickness of CoFeB=1.3 nm [67].

Chapter 3 Experimental Techniques

3.1 Introduction

Magnetic thin films have been the subject of much study over the last two decades due to the interest from the data storage industry in such materials, both for writing and storing information. There is a wide range of systems regarding the practical applications of these films. Materials suitable for magnetic tapes and hard disks, which are required to display high coercivity and form distinct granules, and lacking inter-granular exchange coupling, have been developed and refined over the last 20 years. Meanwhile, the highly-advanced spin valves of GMR read and write heads, which can store huge amounts of data, have been developed since the mid-1990s. In recent years, next generation spintronic devices, such as magnetic random-access memory (MRAM) and the spin field effect transistor (spinFET), have become very popular, and there have been many studies in this emerging area. A wealth of research has been undertaken and a wide range of experimental techniques have been established and used to fabricate and characterise the sampled studies in all projects. Some of these techniques can be found in York, or in the Diamond Light Source. This chapter will present a description of various experimental techniques that have been utilised in these works, and is divided into three main sections. The film growth machine and techniques are introduced in Section 3.2. Section 3.3 introduces the wafer information and cleanroom facilities, and Section 3.4 discusses the various ex-situ structural characterisation methods.

3.2 Room Temperature Growth Techniques

3.2.1 Molecular Beam Epitaxy (MBE)

The advantages of ultrahigh vacuum (UHV) technology over the last two decades have allowed the development of accurate growth methods like MBE[69-73]. This growth method, by reducing the growth rate to a few atom layers per minute, can grow the sample one monolayer by one monolayer., meaning that the film can be grown with a crystallographic relationship to the substrate. In my project, the MBE system was the predominant growth technique for fabricating samples.

The MBE system has a growth chamber equipped with a load lock chamber and a transfer arm for loading samples, a sample manipulator with a heating filament for annealing samples, a penning gauge and an iron gauge for pressure measurement, a tube with argon for ion milling, as well as an electron gun and a phosphorescent screen for reflection high energy electron diffraction (RHEED). There are three kinds of pump, each for different pressures: the rotary pump, turbo pump and titanium sublimation pumps (TSPs), as shown in figure 3.1.

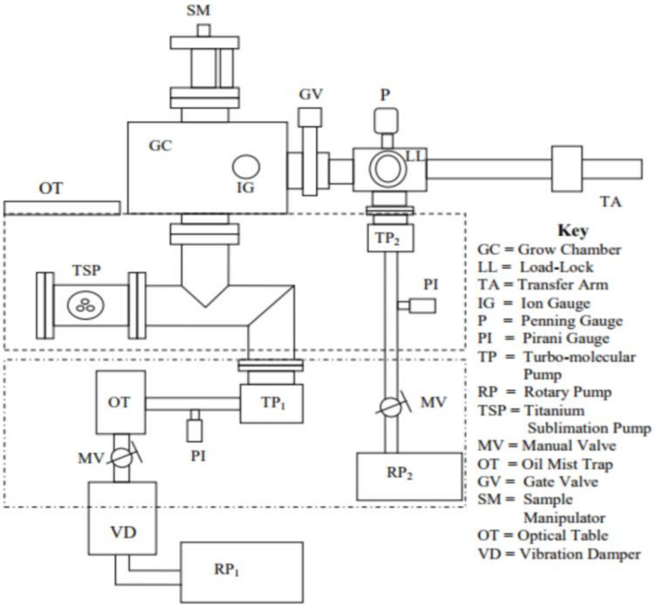

Figure 3.1 The Spintronics Group molecular beam epitaxy vacuum system.

3.2.1.1 Vacuum Pumps and Ultra-High Vacuum

The different pumps are necessary due to the varying range of the pressure. The rotary pump works by reducing the pressure from atmospheric to 1×10^{-3} mbar. The uninterrupted contact of the vanes with the wall of the outer drum allows air to be trapped and, beyond a critical pressure, ejected through oil. The next stage in the pumping system is the molecular pump, which begins pumping from 1×10^{-2} mbar and, depending the system, can achieve chamber pressure around 1×10^{-9} mbar. The speed of the turbo is from 20,000 to 50,000 rpm. If the turbo pump arrives the full speed, any gas molecule or atom which hits the blades have a slight chance of escaping back into the vacuum chamber[74]. Normally, there is another process after turbo pumping: bake-out. The growth chamber is heated to 100˚C, which boils the H_2O molecules in the chamber to a gaseous product, turning the water to steam, and then allows that to leave the chamber through the turbo pump. After this process, the pressure of chamber can achieve 1×10^{-10} mbar. Finally, to reduce the pressure from 1×10^{-10} mbar to 1×10^{-11} mbar, a Ti sublimation pump is used. This pump works by passing current through a Ti filament to raise its temperature to the point of sublimation. The Ti pump traps active elements such as O, N and diatomic H_2, which can then be taken out the chamber, again through the turbo pump. TSPs are not be used when growing the samples, as this process would contaminate the sample.

To arrive at UHV conditions is necessary as it provides good conditions for sample growth, and can result in a high-quality single crystalline film without contamination and oxidization. High quality films are important for the interface structure research and fundamental thin film growth research.

3.2.1.2 Evaporator Design

This MBE system is equipped with three water cooling e-beam evaporators and a large protective shutter. There are two kinds of evaporators: liner driver and crucible (see figure 3.2). That which is chosen depends on the different materials. A crucible design is recommended for materials which easily sublimate, such as Au or Cr, while a material with higher thermal inertia, including Fe, Co, Ni, is suitable to melt from the trip and hence are compatible with a liner driver mechanism. Both design options operate by heating the source material with the top tungsten filament carrying a controlled current at high voltage. Direct current administered via the filament results in an electronic cloud around the filament. After this, high voltage is connected from the bottom and, this time, the point discharge effect being at the top of the materials, the high energy required to heat the materials is produced. When the temperature arrives at the melt point, the materials will evaporate from the rod or crucible. Varying the high voltage and applied current alters the rate of evaporation from the source, which is monitored by means of a calibrated emission current, defined as the current between the evaporator filament and source rod. The major difference between the liner driver design and crucible design is the mechanism for maintaining the emission current. In line drivers this is controlled by the distance between the filament and source: when the distance decreases, the emission current has a high value, which means the rate of evaporation becomes faster than before. In the crucible evaporator, the emission current is controlled by the power supply alone.

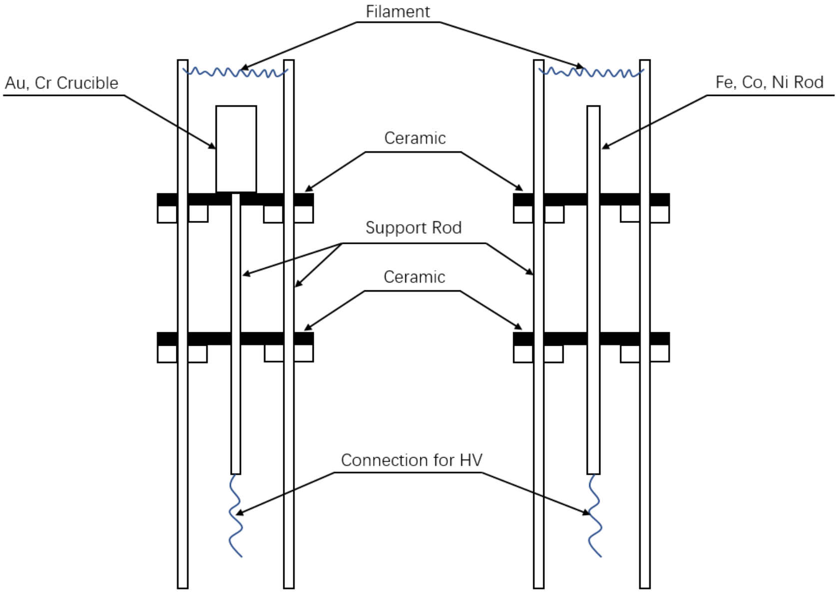

Figure 3.2 Crucible and liner drive evaporators.

The detailed specifications of an e-beam evaporator are shown in figure 3.3. These include the size of flange, source material, cooling jacket and so on. This kind of evaporators are also used by our collaborators in the Nanjing University, China. This design has been proven to be simple and reliable to grow thin film samples.

E-Beam Evaporator

Model: YEBE-001

THE UNIVERSITY of York

All Evaporators are designed to produce ultra-high quality, single crystal thin films via molecular beam epitaxial (MBE) growth from sub-monolayer thickness.

Model	YEBE-001
Flange	DN38CF
Filament	Circular, Tungsten
Sour Material	Rods: 2 mm x 50 mm Crucible: 0.3cc
Cooling Jacket	Water(no vacuum-water welds)
Insertion Length	190 mm Standard
Bakeout Temperature	250 ℃
Growth Rate	0.5ML/min ~ 2ML/min
Filament Current	5.0 ~ 6.0A
High Voltage	700 ~ 1000 V
Base Pressure	$1.1 \times 10^{-10} \sim 3.0 \times 10^{-10}$mbar
Pressure During Growth	$6.0 \times 10^{-10} \sim 1.1 \times 10^{-9}$mbar

Figure 3.3 The evaporator used in Nanjing University MBE system designed by York team.

The sources are essentially degassed to minimise the impurities released into the vacuum chamber during evaporation. Degassing is carried out by applying a small current and voltage, increasing gently until the high voltage required for evaporation may be applied without a substantial rise in pressure.

3.2.1.3 Sample Holder and Annealing Design

There are three grooves on the sample holder, as seen in figure 3.4. The top grove is for the sample transfer arm, which runs the sample holder from the load lock chamber to the growth chamber. The ancipital two grooves are equipped for landing sample holder to the manipulator. This setup ensures that the sample holder transfers from the load lock chamber to the main chamber without running the risk of it dropping into the main chamber.

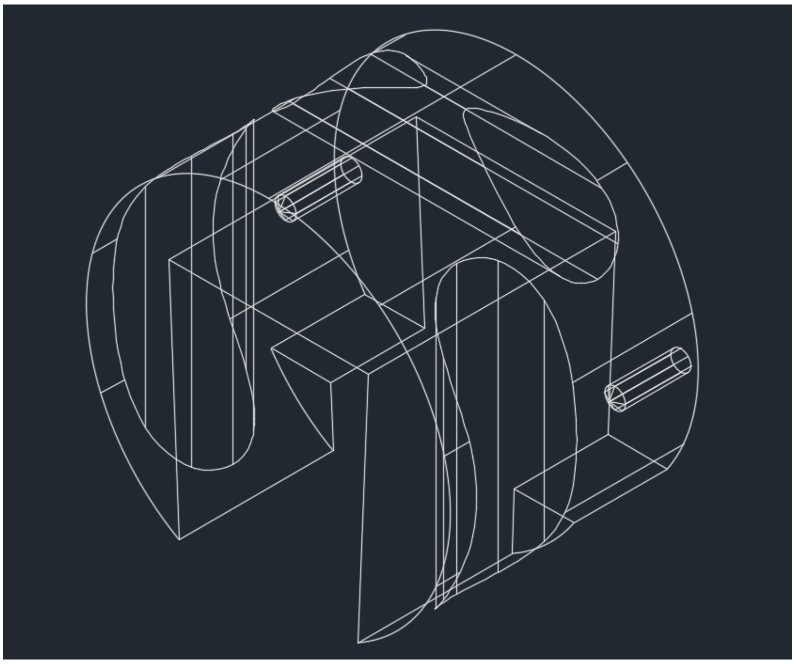

Figure 3.4 3D vision sample holder design.

The sample loading and annealing setup are shown in figure 3.5. There is a clamp with a screw on the sampler holder. This ensures the sample is trapped on the sample holder so that the sample cannot move position. Two tungsten filaments, positioned on both the top and bottom of the sample holder, are controlled by the DC current source and generate thermionic electrons. When the system runs the annealing progress, the 5A current is set on the filament, and the DC voltage source gives a 700V high voltage on the sample holder through the manipulator. After that, with the heating energy focused on the sample holder, the annealing temperature can normally achieve 600 ˚C, and retain this temperature for one hour.

The annealing process is chosen after the iron milling process. There is a sputter ion gun in the front of the MBE system, which ions and electrons are accelerated towards onto the substrate surface. The iron milling process can remove contamination from the substrate surface, but there is a problem. This process will slightly damage the substrate surface, which could make a few small grooves on the substrate. In short, the substrate surface will no longer be a flat surface. The next annealing process is essential for sample growth, not only to remove the surface contamination, but also to prevent a subsequent magnetic dead layer at the surface after film growth[34]. Annealing also forces the substrate to experience a reconstruction process. Reconstruction makes the substrate surface flat and afterwards grow a sample (like iron). Following this, it would display a 4×2 or 4×6 lattice structure on the RHEED pattern[46]. That means this process creates a high-quality sample surface, and as such is very useful for research into surface and interlayer effects.

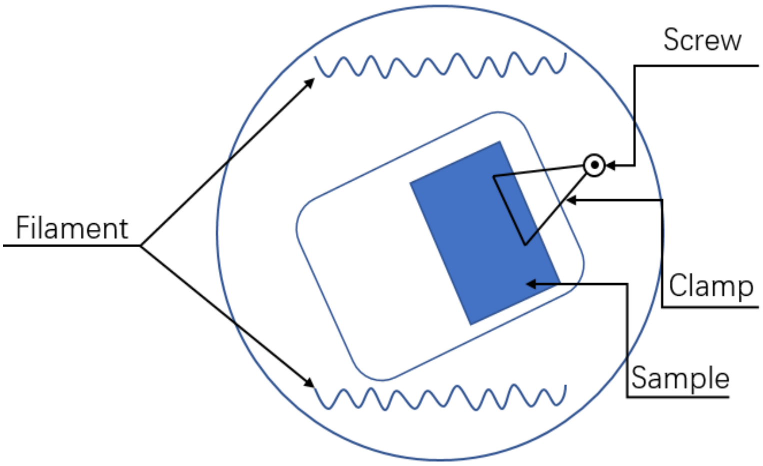

Figure 3.5 Sample holder and annealing setup.

3.2.2 Thermal Evaporator

Thermal evaporation is one of the simplest and most popular method for thin film deposition. The principle of the thermal evaporator is to heat the source material to a high temperature to create vapour, let it be condensed on top of a cool and clean substrate, and then form a layer of thin film. The heating is usually carried out by applying a large current through a filament boat, which has a certain finite resistivity. Tungsten is widely used for the filament because it is chemically stable, meaning that it can easily rise to and withstand temperatures of over 3000˚C. As with most commercial thermal evaporators, the two in the clean room of York University have a distance between the source boat and substrate holder of over 20cm. This requires the vacuum to be sufficient to form a clear path for vapour deposition.

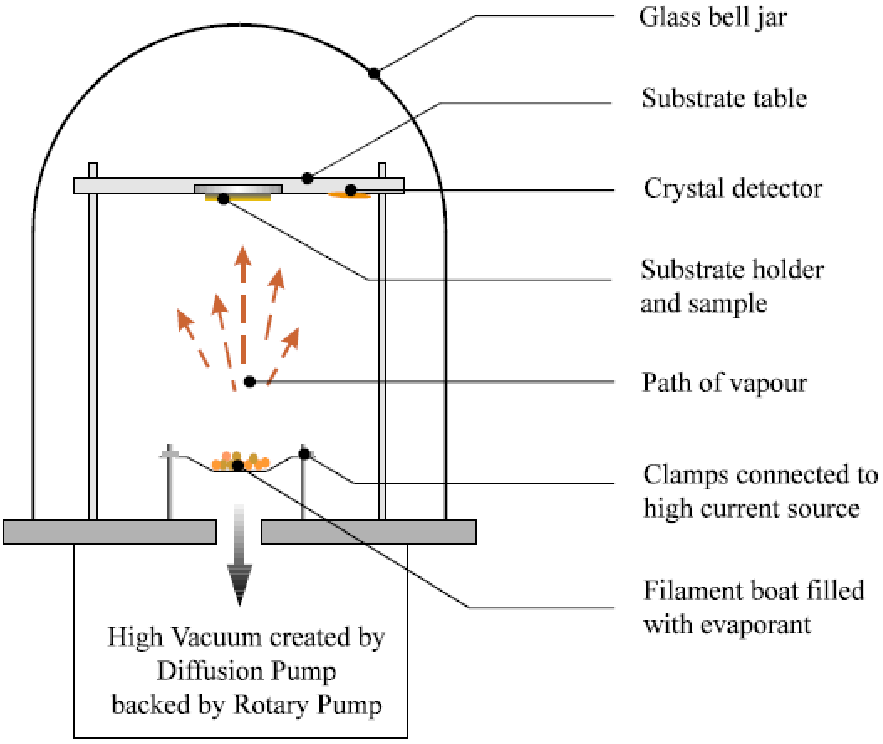

Figure 3.6 system diagram of resistive thermal evaporator.[75]

The growth thickness is monitored by a quartz crystal rate meter. This is a commercial model, which has computer software to control the data analysis from the sensor. Normally, the growth temperature is room temperature (around 25˚C) and the minimum pressure requirement for evaporation is below the 10^{-5} Torr level. The better the vacuum, the better the sample growth, because the contaminations from outside (like water or dust) will be removed, when samples is in a high vacuum situation.

3.3 Cleaning Room Facility

In the Department of Electronics at the University of York, sample fabrication and preparations depend on the availability of a well-equipped class 1000 clean room. In this section, a sample preparation process and the selection of substrate wafer are briefly introduced.

3.3.1 Semiconductor Substrate Preparation

In this project, all the chemical treatments for the samples are performed on the wet bench. The commercial GaAs wafers used were all cleaned using a series of pre-defined chemical etches, by using a mixture of acids and other chemicals as detailed in Table 3.1.

Table 3.1 Substrate preparation process.

Cleaning Process	**Duration**
RBS, Acetone, Isopropanol ultrasonic bath	5 minutes respectively
Acid etching H_2SO_4:H_2O_2: H_2O = 4:1:1	45 seconds
DI water rinse and Nitrogen Blow	Thoroughly and blown dry
Outgassing at 200°C	12 hours

Ion-milling at $5x10^{-6}$mbar	30 minutes
Annealing at 500°C	60 minutes

All substrates were cleaved from the commercial wafer and cleaned with detergent (RBS), action and isopropanol for 5 minutes respectively. The next step is acid etching. The substrate is placed into the H_2SO_4:H_2O_2: H_2O (4:1:1) solution for 45 seconds and the beaker is shaken. The residual solutions were rinsed off with DI water and substrates were blown dry using filtered Nitrogen. All operations were performed in a level 100 clean room and a class 100 wet-bench to prevent any dust particle contamination. The etched substrates were immediately transferred to an MBE chamber with a base pressure of $2x10^{-9}$ mbar, and heated to 200°C for 12 hours to completely remove any water molecules or gas attached to the surface. After that, low energy Argon ion beams were sputtered onto the substrate surface for 30 minutes to gently remove the contamination from the surface. Finally, the substrates were further required to be annealed at 500°C for 60 minutes to remove natural oxides and create unified surface reconstruction as seen in table 3.1.

3.3.2 GaAs (100) Wafer Selection

The most widely used wafer in this project is the commercial epi-ready GaAs (100). These wafers can be purchased from Wafer Technology UK, IDB Technology and Good Fellow Ltd. When purchased, it is vital to confirm how the suppliers classify the product in terms of the substrate crystallography, i.e. EJ or US, as this defines the direction of the main crystallographic axes. According to the EJ definition, the major flat of the wafer refers to [0-11] axes, while for the US it is [011] direction. The definitions of the crystallographic directions are illustrated in Fig 3.7. How the axis is marked will vary with different suppliers.

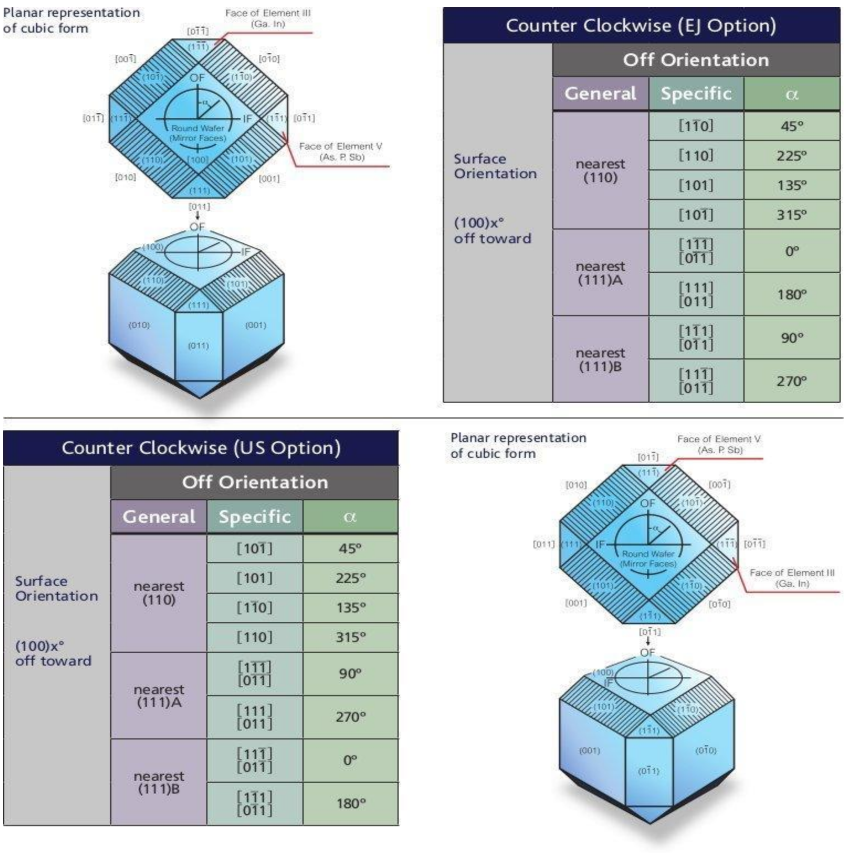

Counter Clockwise (EJ Option)			
	Off Orientation		
	General	Specific	α
Surface Orientation (100)x° off toward	nearest (110)	$[1\bar{1}0]$	45°
		$[110]$	225°
		$[101]$	135°
		$[10\bar{1}]$	315°
	nearest (111)A	$[1\bar{1}\bar{1}]$ $[0\bar{1}\bar{1}]$	0°
		$[111]$ $[011]$	180°
	nearest (111)B	$[1\bar{1}1]$ $[0\bar{1}1]$	90°
		$[11\bar{1}]$ $[01\bar{1}]$	270°

Counter Clockwise (US Option)			
	Off Orientation		
	General	Specific	α
Surface Orientation (100)x° off toward	nearest (110)	$[10\bar{1}]$	45°
		$[101]$	225°
		$[1\bar{1}0]$	135°
		$[110]$	315°
	nearest (111)A	$[1\bar{1}\bar{1}]$ $[0\bar{1}\bar{1}]$	90°
		$[111]$ $[011]$	270°
	nearest (111)B	$[11\bar{1}]$ $[01\bar{1}]$	0°
		$[1\bar{1}1]$ $[0\bar{1}1]$	180°

Figure 3.7 GaAs wafer with different crystallographic direction defined with EJ and US option[76].

3.4 Characterisation Measurement Techniques

3.4.1 Reflection High Energy Electron Diffraction (RHEED)

Growth quality in the main chamber was monitored by RHEED. This technique is used to characterise the flatness and surface crystalline structure of a sample or substrate material. An electron gun with a high energy range, from 10 to 50 keV, provides a beam of electronics which impinges upon a given sample surface at an angle of about 1°, and is diffracted and reflected onto the fluorescent screen, as shown on figure 3.8.

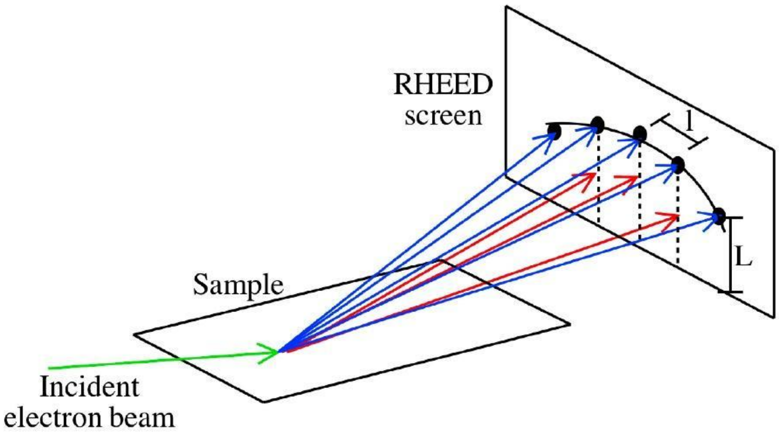

Figure 3.8 RHEED structure. A high energy beam from the electronic gun accelerates electrons onto the sample surface at a very small angle and gets diffracted to form a diffraction pattern on a fluorescent screen.

Typical static RHEED patterns, as in figure 3.10, were recorded in my experiments, and give an immediate indication concerning the structural quality of the film. As noted before, the iron milling process will cause slight damage the substrate surface, so it is expected that the surface would display roughness. Thus, from the RHEED pattern, the spotty model can be seen on the screen, as in figure 3.9. However, if the substrate has gone through the annealing process, the roughness will be fixed due to the surface reconstruction. In this case the whole sample surface will revert to a flat condition, and so the straight line RHEED pattern can be found on the screen. After surface reconstruction, the substrate not only removes the dead layer, which could put off the formation of single crystalline structure, but it also forms a high quality 4×2 lattice structure[31, 34], as in figure 3.10. This could achieve a high-quality single crystalline film. In general, a spotty RHEED pattern indicates a rough three-dimensional (3D) growth, whereas a streaky RHEED pattern indicates smooth two-dimensional (2D) growth.

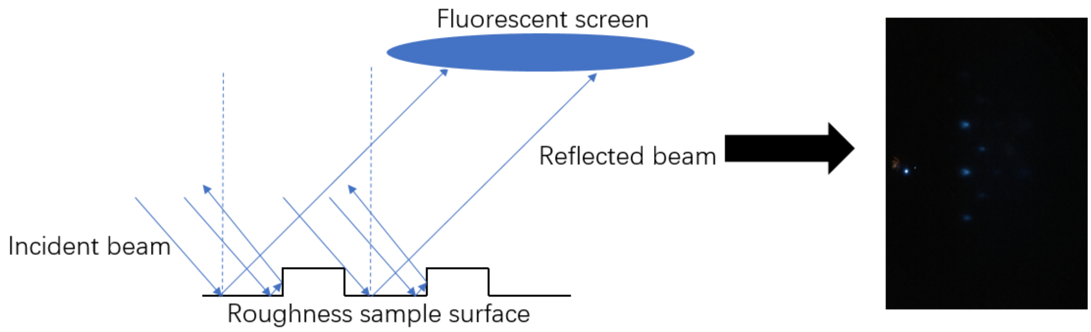

Figure 3.9 GaAs (100) substrate with iron milling process only formed the roughness surface. From the RHEED pattern, a spotty model is shown.

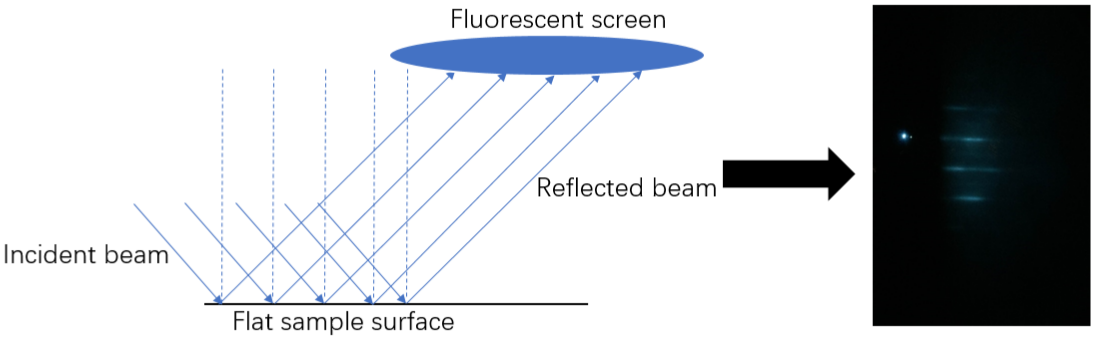

Figure 3.10 GaAs (100) substrate with the iron milling and annealing process formed the flat surface. From the RHEED pattern, a crystalline structure is shown.

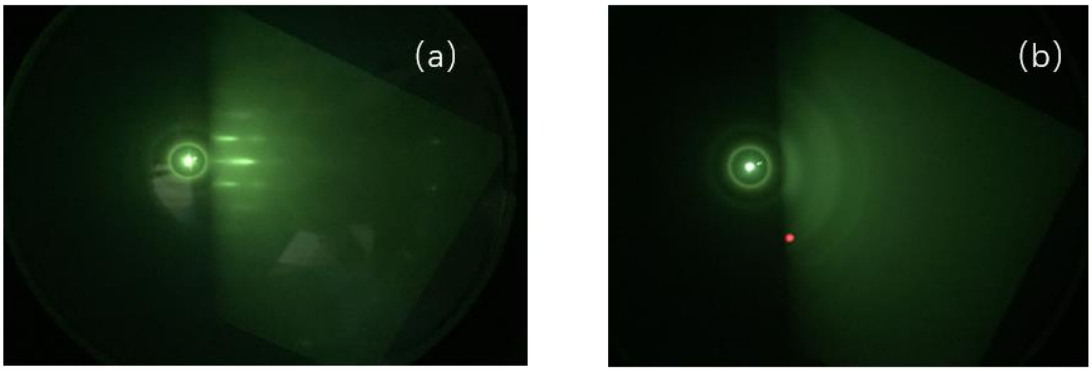

Figure 3.11 RHEED pattern for different crystalline structure. (a) is the 7ML Fe on GaAs (100) substrate, RHEED pattern shows the standard single crystalline structure; (b) is the 7ML Fe on 5nm Au interlayer on GaAs (100) substrate, RHEED pattern shows the typical polycrystalline structure.

The RHEED measurement indicates the crystalline structure of the films. There are two common types of structure seen from RHEED: the single crystalline structure and the polycrystalline structure. Let us take Fe film on GaAs (100) surface as an example. Because the lattice constant of 2.87Å for Fe is almost exactly to half of GaAs (5.65 Å), it is easier to form the single crystalline film when Fe thickness is from 5ML to 20ML, as shown in figure 3.11(a). However, there is a large lattice mismatch between Fe (2.87Å) and Au (4.07Å), so when the same thickness Fe film (7ML) grows on an Au interlayer, the RHEED pattern shows the polycrystalline structure, as shown in figure 3.11(b). Fe films on GaAs substrate should be a single crystalline film when Fe film thickness is between 5ML and 20ML. However, if the GaAs substrate is rough, and the Fe atoms land on the rough GaAs substrate, this will enlarge the lattice mismatch between the GaAs and Fe, so the Fe film could be a polycrystalline structure. The RHEED measure, especially with Fe under 20ML, can let us know the quality of film growth. Fe film over 20ML is different, as the volume contribution will influence the form of the crystalline structure and make the single crystalline structure turn to the polycrystalline structure.

3.4.2 Atomic Force Microscopy (AFM)

Atomic Force Microscopy is a surface technique widely used for investigating surface morphology and thickness. In figure 3.12 we can see a schematic diagram of an AFM system. The AFM image is performed in either contact or tapping mode, using the repulsive Van der Waal force between the atoms at the tip and those of the surface. A laser beam focuses onto the cantilever, and then reflection of the beam from the cantilever is collected by a photodetector consisting of two photodiodes.

For this work, a JEOL Scanning Probe Microscope 5200 was used with a commercial Si tip of 10 to 20 nm radius. The 3D information collected is displayed as a topographic image. AFM can also be used for MBE system film thickness calibration, but in this case, there should be an obvious sharp step on the sample surface, so that when the tip scans the area around the step the thickness data can be derived from the measurement. One way to create such a sharp step when growing a sample in an MBE system is shown in figure 3.13(c). The polished sides of two GaAs substrates are joined face to face, then tightened using a clamp from the sample holder. After the growth process, the sample is removed from the chamber immediately. The top substrate, which was the smaller substrate, started the AFM measurement. The obvious step can be seen in the 2D and 3D diagrams from figure 3.13(a) and 3.13(b). The tip can then be moved to the step area to measure the Z-axis direction. Figure 3.13(d) indicates the height of the step, and also the thickness of growth sample.

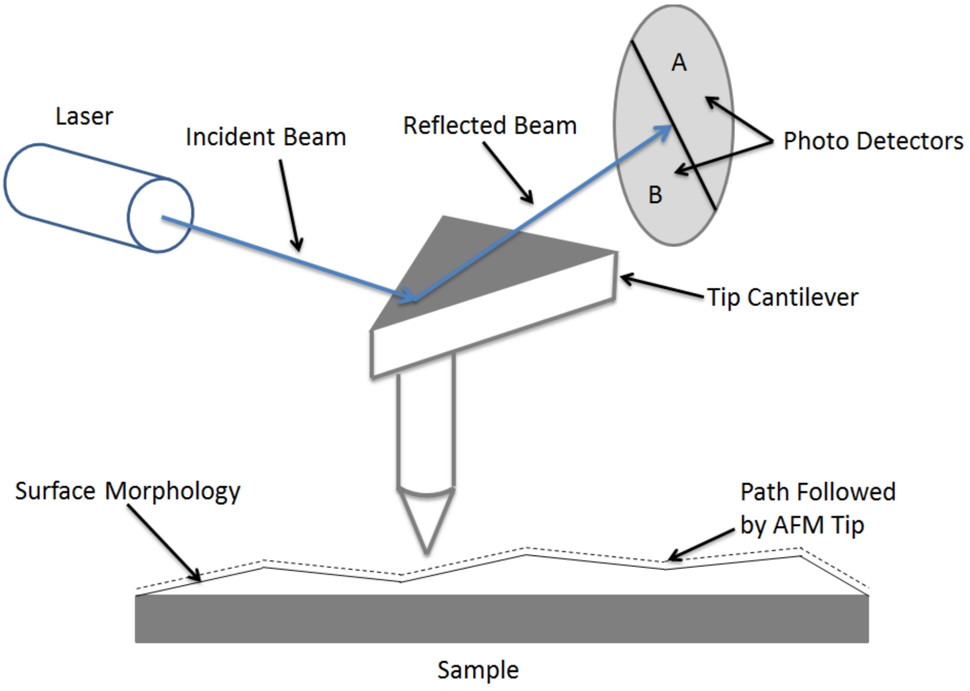

Figure 3.12 Schematic diagram of an atomic force microscopy (AFM). A laser beam is focused onto the cantilever and reflection of the beam from the cantilever is collected by a photodetector consisting of two photo-diodes, A and B respectively, during the raster scan of AFM tip on slightly top of the sample surface.

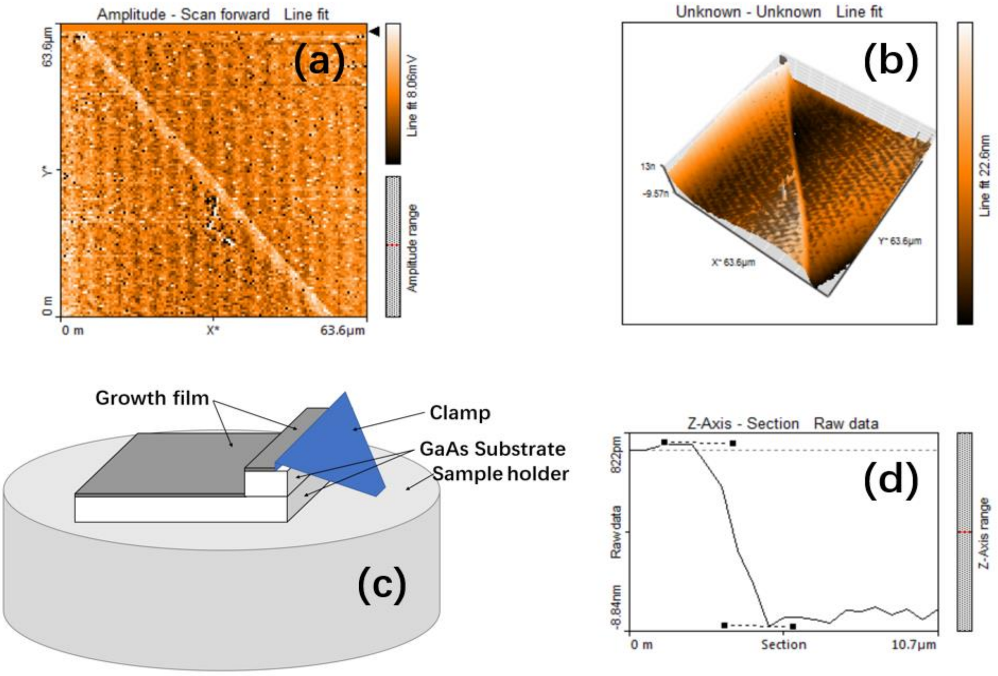

Figure 3.13 (a) and (b) indicate the film morphology with 2D and 3D diagrams respectively; (c) shows the creating sample setup; (d) displays the value of height of the step from Z axis (the film thickness).

The amount of the material deposited on the substrate surface needs to be monitored for steady growth rate and thickness calculation. In my project, the growth rate is measured by a quartz crystal microbalance sensor. Quartz crystal is a type of thin and fragile material which has the property of generating an electrical current with a fixed oscillation frequency when electrically energised. When source material is being deposited on the sample, it is also applied to the sensor surface, which means that the total mass of the crystal is increased, which thus decreases the resonant frequency.

The quartz crystal frequency is 6 MHz, and the digital controller offers a precision of 0.01 Hz. This is a very sensitive measurement device and has the virtue of always being stable. Since the signal from the quartz crystal is very small, the connection wire is equipped in the MBE chamber, which is on the shutter in front of the sample holder.

The growth rate of the e-beam evaporator is controlled by monitoring the emission current of the source material. This makes the thickness monitor calibration easier, as the calculation can be expressed as the equation:

$$\text{Growth rate} = \Delta \text{thickness}/\text{time}$$

$$\text{Relation between QTM and thickness} = \Delta \text{actual thickness}/\Delta \text{frequency}$$

The calibration data for different sources calculated by AFM measurement and quartz crystal frequency are all shown in Table 3.2.

Table 3.2 Growth Rate for various sources from the MBE system

	High Voltage	**Filament Current**	**Emission Current**	**Growth Rate**	**Calibration data**
Bcc Fe (1ML = 1.43 Å)	750 V	4.8 A	10.6 mA	6.13 Hz/min	6.85 Hz/ML
Hcp Co (1ML = 1.26 Å)	750V	5.4 A	17.5 mA	6.31 Hz/min	7.26 Hz/ML
Fcc Ni (1ML = 1.44 Å)	800V	5.1 A	13.2 mA	6.2 Hz/min	7.80 Hz/ML
Bcc Cr (1ML = 1.44 Å)	900V	5.2 A	30.2 mA	6.0 Hz/min	6.25 Hz/ML
Fcc Au (1ML = 2.04 Å)	700V	4.8 A	21.3 mA	7.0 Hz/min	16.10 Hz/ML

3.4.3 Transmission Electron Microscopy (TEM)

3.4.3.1 Introduction

The TEM is a very significant invention, and is the first electron microscope to break through the limits of the optical light microscope and bring us to the world of Nano scales. The TEM has a very high electron beam which transmits through a very thin specimen and projects onto a fluorescent screen. The biggest advantage of the TEM is the high resolution it can achieve. The detailed structure of the TEM is complicated, and so is presented here in more detail. The general layout is illustrated in figure 3.14.

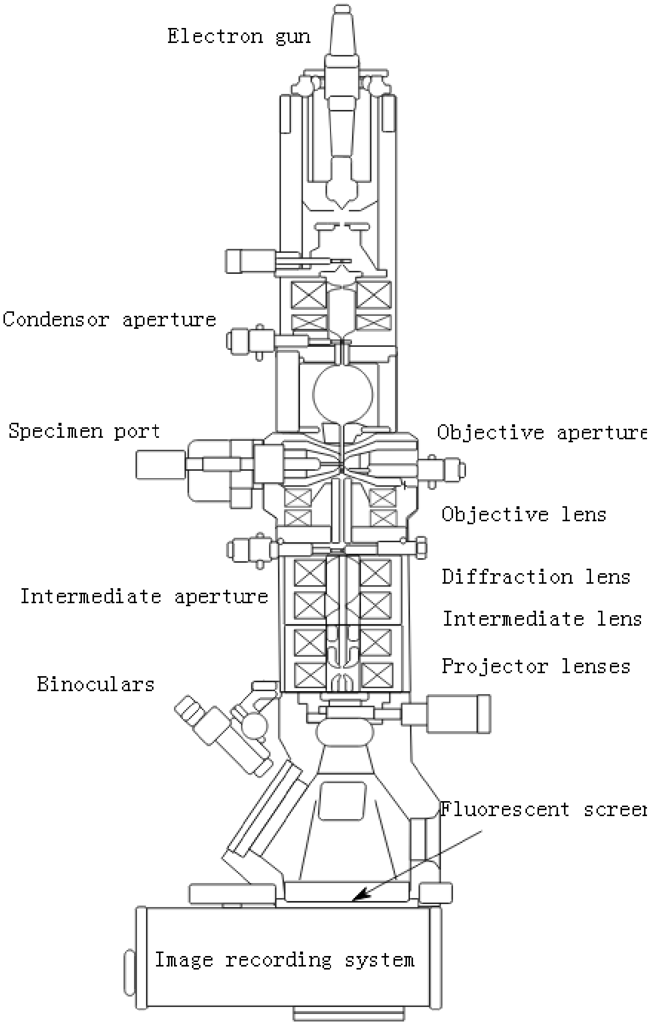

Figure 3.14 Layout of components in a basic TEM[77].

3.4.3.2 Sample Preparation

TEM measurements usually investigate the cross section of the sample, and structure information and thickness data is derived from the TEM image. Because the penetration depth of the beam is under 1μm, a very thin specimen with a small polished hole from the polished cross section of the sample (around 1μm) is required.

The first step is to cut the sample and referential substrate using a Diamond saw blade, then to glue two pieces of sample and substrate together (with substrates as the outside part, the inside part being the sample). This is shown in figure 3.15.

Figure 3.15 the gluing substrates and samples.

The next step is to polish the back and front side of the specimen with Diamond lapping paper (using 1,3 and 6μm polishing pads to give a high quality polished surface and a glue line free from asperities) and the polishing table. When the sample undergoes the polishing process, it is very important to keep the tap open a little bit, which will allow the polishing disks to clean and wash away the polished dropped part. The finished, polished sample cross section surface should look like figure 3.16 (b), which used the silicon substrate and shows a sliver grey colour. If the preferred substrate chosen is the GaAs, then an orange colour would be seen from the reflectance light microscope. After polishing process, the specimen should be mounted on the sample holder for precision ion polishing system (PIPS).

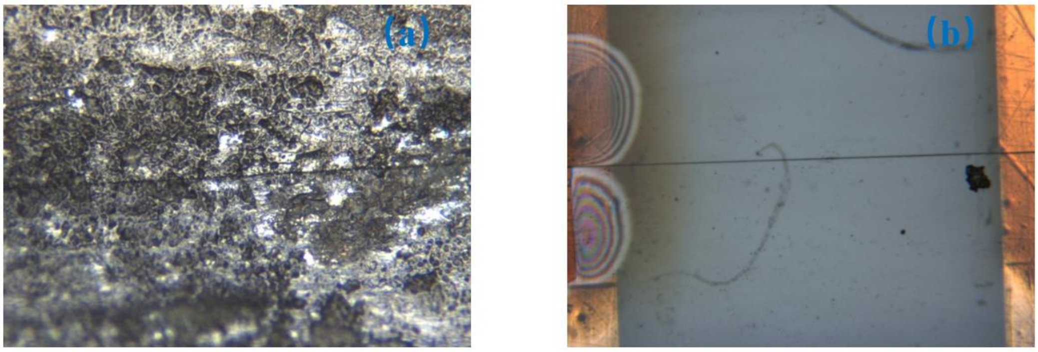

(a) (b)

Figure 3.16 shows the different processes of Si substrates and samples polishing patterns. (a) shows the un-polished sample surface with black and white part on the roughness surface; (b) indicates the polished samples and substrates with the sliver grey colour on flat surface from reflectance light microscope.

PIPS guns could achieve 20μA at 3.5Kev, although a higher value is desirable. PIPS should be run in double mode for x-sections at 3.5Kev with both guns at ±6° until a small hole is visible in the glue line. Once a hole is seen in the glue line, PIPS should be adjusted at 1.0KeV for 3 minutes with guns at both ±8° followed by PIPS at 0.3KeV for 10 minutes with guns at ±8°. The PIPS process helps to polish the cross-section of a small area and form a small hole with several steps on it, which is helpful for monitoring the cross-section on the TEM image. The PIPS polished sample can be seen in figure 3.17 (a) and (b).

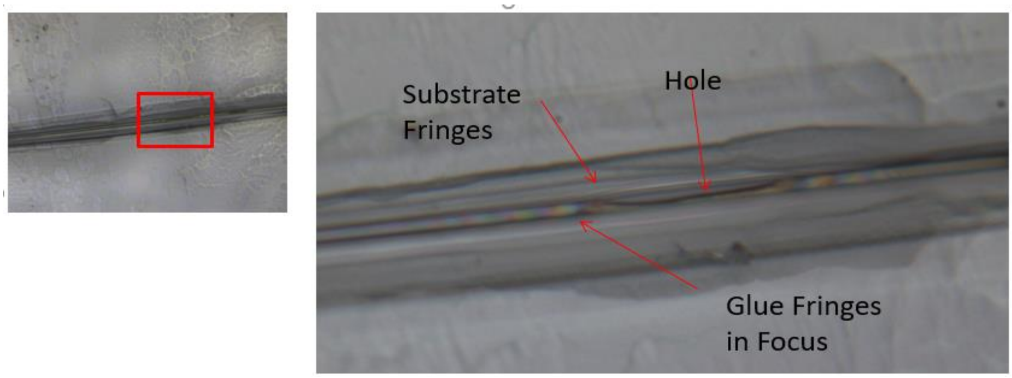

(a) (b)

Figure 3.17 shows the substrate fringes, glue fringes and the hole which experienced the PIPS process on the polished surface.

3.4.3.3 The TEM Image

The Electron Source is at the top of the TEM. It formed with a filament, a Wehnelt cap and an anode. The filament can be made of LaB6, and it connects to a negative power supply. LaB6 filament sources have a special design, which uses a heating coil to heat the LaB6 rod to generate electrons. This type of filament generates more electrons at the same temperature, and hence offers a brighter image at high resolutions. When heated, the Lab6 electron beam is pumped out from the filament surface and forms an electron cloud. The Wehnelt cylinder is cap-shaped, made of metal and covers the filament. As it is also heavily negatively biased, the aperture in the middle can help focus the electron cloud to form an electron beam with a small crossover diameter. The anode plate works like an electron extractor since it is grounded or positively biased compared to the filament.

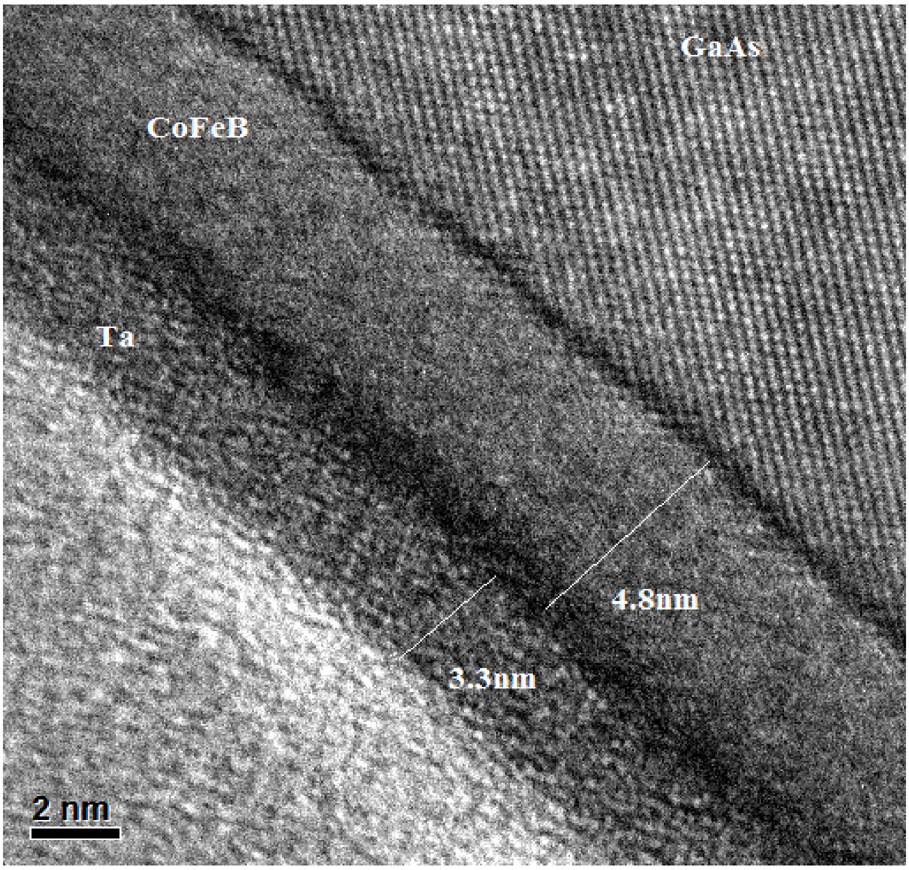

Figure 3.18 Cross-sectional TEM of CoFeB on GaAs (110). The thickness values of CoFeB and Ta are 4.8nm and 3.3nm respectively.

The TEM image has two major functions for the different structure samples. First, the different structure of the sample can be seen from the TEM image, whether it is single crystalline, amorphous or polycrystalline. As can be seen in figure 3.18, it is easy to find the different layers and structures of the sample: the GaAs substrate is the bottom part with a single crystalline structure; the mid grey part is the CoFeB film with the typical amorphous structure; the top area is the Ta capping layer, which has a polycrystalline structure. Another important function is the recalibration of the film thickness. The fundamental thickness calibration measurement is the AFM measurement, with the TEM acting as a secondary means. It can also double check the calibration data compared with the AFM thickness data. From the TEM image, the thickness values of CoFeB and Ta are 4.8nm and 3.3nm respectively, and this thickness data is well matched with the growth settings.

3.4.4 Vibrating Sample Magnetometer (VSM) and Magnetic - Optic Kerr Effect (MOKE)

3.4.4.1 VSM Measurement

A vibrating sample magnetometer (VSM) measures magnetic properties. Simon Foner invented the VSM in 1955, and reported it in 1959[78, 79]. A sample is first magnetized in a uniform magnetic field - commercial systems use linear actuators of some form. In my experiments, the Vector Magnetometer Model 10 VSM machine was used for the measurement. Historically, these systems were developed using modified audio speakers, although this approach was dropped due to the interference caused by the produced in-phase magnetic noise due to the variance in magnetic flux through a nearby pickup coil. The induced voltage in the pickup coil is proportional to the sample's magnetic moment, but does not depend on the strength of the applied magnetic field. In a typical setup, the induced voltage is measured with a lock-in amplifier using the piezoelectric signal as a frequency reference. It is also possible to record the hysteresis curve of a material by sweeping the magnetic field.

The structure of a VSM is shown in figure 3.19. The magnetic field applies from -2T to 2T. The sample holder can be rotated through all angles and it also can measure the temperature from 77 K to 773 K.

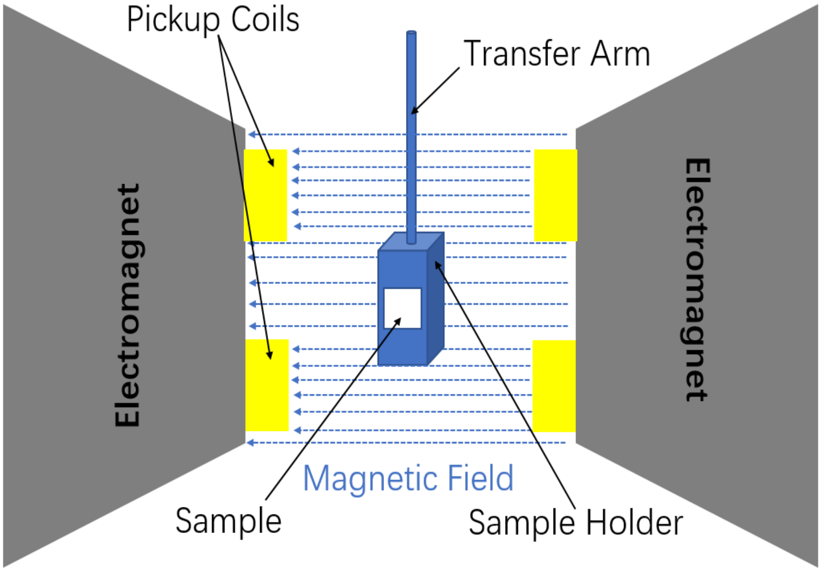

Figure 3.19 VSM internal structure which has two electromagnets, transfer arm, sample holder and coils.

3.4.4.2 The Origin of MOKE

The Magneto-Optic Kerr Effect (MOKE) has been widely used for determining magnetic properties. It observes the optical reflection on a static magnetic material, traces the polarisation rotation as a function of the varying magnetic field applied, and plots the hysteresis loop as the output for studies. The MOKE was discovered by John Kerr in 1877, who while studying the light reflected from a sample subjected to a magnetic field, observed changes in the polarisation and ellipticity of the reflected light. Analogous to the transmission mode Faraday effect, the reflection mode MOKE is now a popular tool in the magnetic characterisation of magnetic thin films[80, 81].

3.4.4.3 Ex-situ MOKE and In-situ MOKE Setup

Both in-situ and ex-situ MOKEs have a similar setup, as shown in figure 3.20 (A) and (C) respectively. The magnetometer utilises a diode laser with a wavelength of 670 nm and an output energy if about 5mW. The laser beam first passes a polariser and is subsequently reflected from a sample surface. Following an aperture for beam path alignment, the reflected beam passes the focus lens and then enters an analyser on the photodiode with an embedded amplifier powered by a pair of 9V batteries. The optical signal collected by the photodiode is converted into an electrical signal by an analogue to digital converter and subsequently sent to a computer.

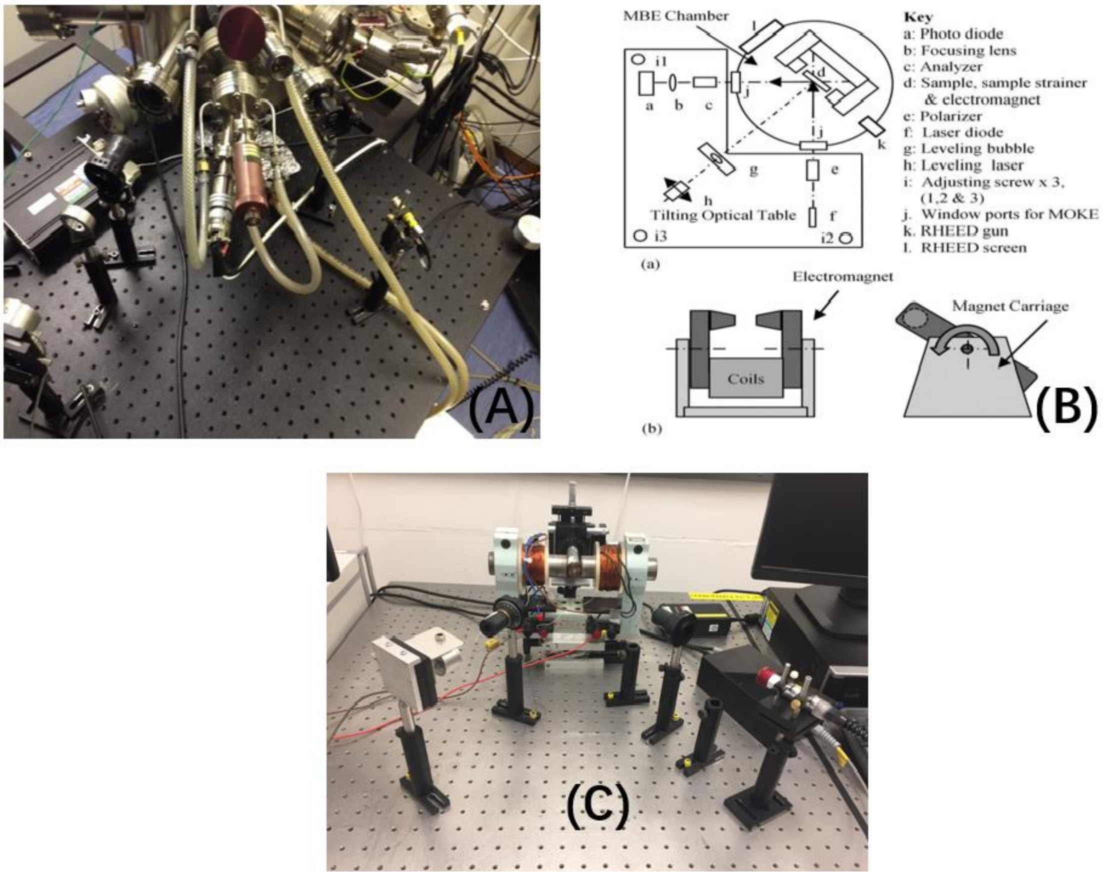

Figure 3.20 (a) and (c) indicate the in-situ and ex-situ MOKE setup; (b) shows the details concerning the laser line, focusing lens, magnet position and so on.

The controlling software used for the MOKE measurement is a LabView programme. The major function of this programme is to output a given voltage to the 1000W amplifier which is used to set the field in the electromagnet and capable of generating a maximum field of 1800 Oe. Another advantage of this setting is the rotating sample holder, which allows for a 360° rotation for ex-situ MOKE and a 180° rotation for in-situ MOKE (using a manipulator). This is particularly convenient for studying the in-plane magnetic anisotropy of samples.

The difference between ex-situ and in-situ MOKE is clear. The ex-situ MOKE needs a sample with a capping layer, which the in-situ MOKE does not require. Some samples, such as Fe, Ni, Co and so on, easily form an oxide layer without a capping layer when samples are taken out of the vacuum. Given this, these samples need an Au or Cr capping layer for ex-situ measurement. Some capping layers like Cr, which is an antiferromagnetic material, will make some impact on the magnetic properties of the sample. This means that the data from ex-situ MOKE slightly differs from the sample's original magnetic properties. The advantages of in-situ MOKE is that the sample can be measured in the UHV chamber without a capping layer, and there are no concerns about oxidisation. Generally, in-situ MOKE is more accurate; its setup is shown in figure 3.20(B).

3.4.4.4 MOKE Configuration

Depending on the various shapes and magnetic orientations of the samples, there are three commonly used configurations for the MOKE set-up: Polar, longitudinal and transverse, each of which is shown in figure 3.21. Polar MOKE measures the magnetisation component vector perpendicular to the reflecting surface plane but parallel to the plane of incidence. Generally, it provides the largest rotation angle and thus the strongest signal, but it also requires a considerably large external field to saturate the films out of the plane. Unlike the polar MOKE, longitudinal MOKE has the magnetic field applied in the same plane of the reflecting surface, measuring the components within the plane parallel to the sample surface. Longitudinal MOKE is the form predominantly used for the author's research as it offers a strong and rather unified magnetic field, which is ideal for thin film properties studies. For the transverse MOKE set up, the magnetic field is applied perpendicularly to the plane of incidence. This configuration measures the reflectivity change which is proportional to the change of magnetisation components within the plane of reflectivity, but normal to the plane of incidence.

The ex-situ longitudinal MOKE systems used in my studies were as follows. The sample holder is adjustable both horizontally (in the plane of the magnetic field) and vertically (perpendicular to both the plane of incidence and applied field), while fine adjustment by three screws is available to ensure precise position in the third axis, about which the sample is also rotatable.

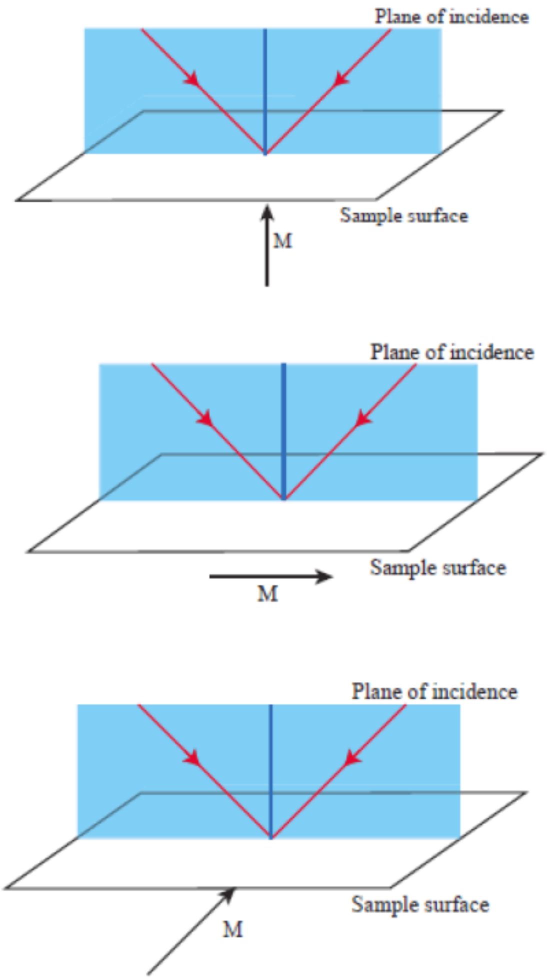

Figure 3.21 Three kinds of MOKE measurements. The top is the polar MOKE, the middle is the longitudinal MOKE and the bottom is the transverse MOKE.

3.4.4.5 Hysteresis Loop

Magnetic hysteresis refers to the irreversibility of the magnetisation and demagnetisation process. When an external magnetic field is applied to a ferromagnetic sample, the domain which is aligned to the axis closest to the field will increase in volume, and will tend to exceed all other domains and form a single domain. If this external field is removed, the single domain will tend to form closure domains, thus reducing any stray magnetic field. A large demagnetising field will be formed due to single domain. Domain walls can be pinned by crystal defects. Without an external reversing field, the domain walls can never be fully reversed when pinning sites exist. This results in the hysteresis phenomenon[82].

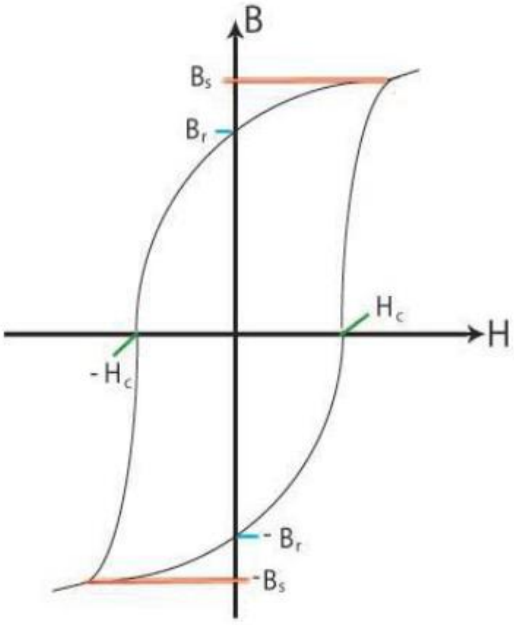

Figure 3.22 Typical hysteresis loops. B_s is the saturation magnetization, B_r is the remanent magnetization, and H_c is the coercivity field[83].

The typical hysteresis loop, shown in figure 3.22, illustrates the different parameters obtained from the loop. These data indicate the magnetic properties of the film, and are extremely useful.

3.4.5 X-ray Magnetic circular dichroism (XMCD)

3.4.5.1 Diamond Light Source Station

The Diamond Light Source station has been serving the global research community for over a decade. The research potential of the synchrotron is based on a linear accelerator and 33 electron beam lines, as shown in figure 3.23. Each beam line has a different beam energy range to allow various fields of study. In my experiments, stations I06 and I10 are used to study the electronic and magnetic structure using soft X-ray resonant scattering (reflection and diffraction) and X-ray absorption. Both beam lines allow a broad range of studies focused on the spectroscopic properties and magnetic ordering of novel nanostructured systems. The only slight difference between them is the energy range. In I06 the energy ranges from 106 to 1300 eV, and the magnet can achieve 6T, while in I10 station, the beam line energy is from 500 to 1600 eV, and it is equipped with the 14T superconducting magnetic[84]. In fact, this has no influence on my experiment since Cr and Fe elements are used, which can be detected in a range from 500 to 800 eV. Even a 2T magnetic field could saturate all my films.

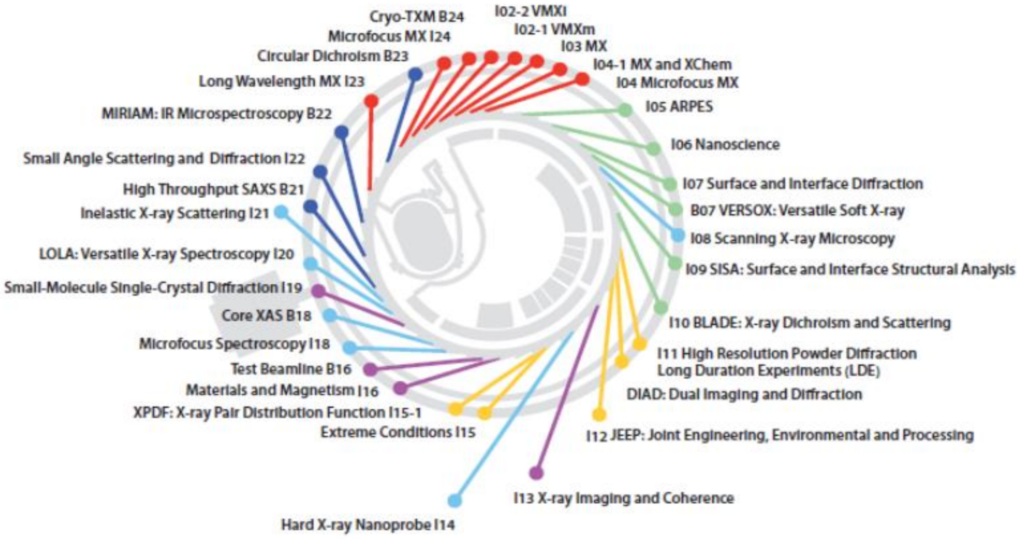

Figure 3.23 Diamond Light Source different energy beam lines. the sample colour beam lines indicate similar energy range[84].

The Diamond Light Source uses an Elliptically Polarizing Undulator (EPU) light source to produce X-ray beams of variable polarisation state. The beam line delivers high flux and the brightness of X-ray light, covering the L-edges of 3d elements, and is therefore the best suited for this project. The analysis station located at the end of the beam line is designated the 'Octupole end station'. An octupole UHV chamber contains eight water-cooled electromagnets which have been specifically engineered to offer unlimited optical access for the X-ray beam. These eight electromagnetic cores were spaced equidistantly over the surface of a sphere, and the effective magnetic field region in the central region is the vector sum of the magnetic field generated by each magnetic pole. This setup allows the magnetic field to be rotated freely without obstructing the X-ray beam path. Working in conjunction with a 5-axis manipulator, and having the option of rotating the entire chamber, allows for the measuring of the magnetic properties with effectively limitless geometry of applied field, X-ray and sample orientation.

3.4.5.2 XMCD Introduction

XMCD is a unique technique that uses X-ray to study magnetism. It offers element-specificity and allows one to identify the origin of the magnetic signal in each material ranging from simple elemental films to complex alloys and compounds.

For the 3*d* transition metals, on which this work focuses, it is necessary to understand the dichroic effect for the L_3 and L_2 edges, which correspond to the $2p_{1/2}$ and $2p_{3/2}$ levels observed in the context of a p to d transition. It is possible to view the situation in terms of energy level diagrams, as seen in figure 3.24. Figure 3.24 (a) shows a non-magnetic material in the no magnetic field. This material demonstrates equal levels of spin up and spin down in its population. In figure 3.24 (b) it can be seen how applying an external magnetic field, H, to magnetic materials provokes a disparity between the population of spin up and spin down bands. The result of this is a configuration where some empty 3*d* spin up states exist which may only be filled by spin up $2p$ electrons, meaning that the empty $3d$ states can act as spin dependent detectors. The situation is complicated by the spin-orbit interaction which causes the $2p$ core state to split into two components, the $2p_{1/2}$ and $2p_{3/2}$ states[85]. As well as the energy separation of these components, which amounts to a few eV in this case, the effect is important because these spin sub-states are now also coupled to the orbital moment. This orbital moment adds to the complication by coupling both parallel and antiparallel to the spin moment in the L_3 and L_2 edges respectively[86, 87].

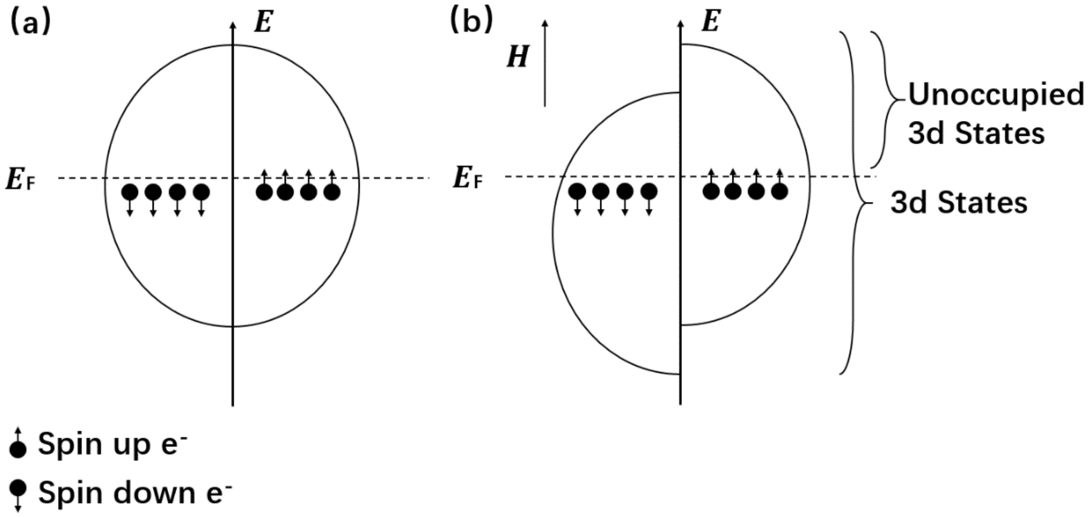

Figure 3.24 Band illustrations of (a) a non-magnetic material and (b) a magnetic material with an external field.

The incident circularly polarised photons have an angular moment of negative for right and positive for left circular polarisation. As such, when illuminating the sample with circularly polarised light, the probability of excitation will be greater if the angular momentum of the x-ray photons is coherent with that of the orbital momentum. A spin up $2p_{1/2}$ electron is most likely to be excited by left circularly polarised light. The difference in detected absorption between left and right circularly polarised light shows the XMCD signal.

3.4.5.3 Preparation for sample measurement

The samples for XMCD measurement should use the sliver pants to glue them to the sample holder. The sliver pants allow some samples (such as two-dimensional materials) to have a good electro-conductive property when glued to the sample holder. After the gluing process, the sample conductivity should be tested by a mustimeter, to make sure the sample surface is conductive, and then the position of the samples can be marked on the sample holder, as in figure 3.25 (a). The position of samples is very important for the later measurement because the sample position should be locked at beginning of the measurement by scanning the horizontal and vertical axis, as in figure 3.25 (b). There are three clear stages in figure 3.25 (b) shown by measuring the vertical axis, and then the beam line can focus on the accurate positions.

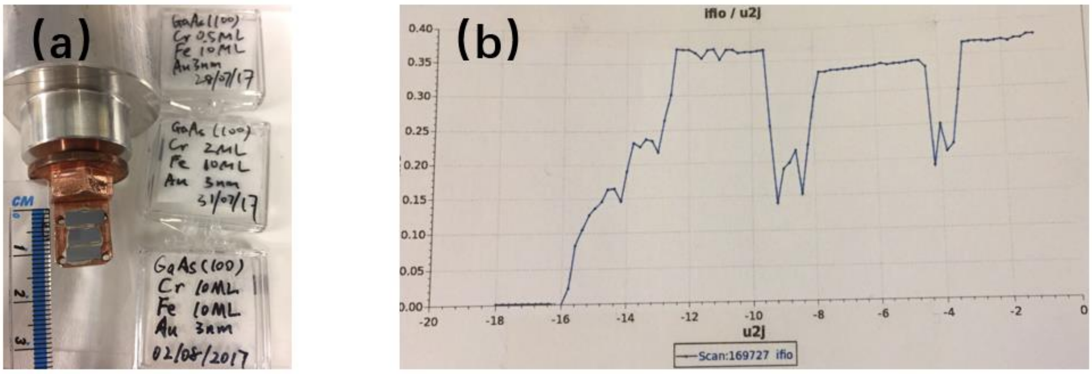

Figure 3.25 Sample preparations for measurement. (a) indicates the sliver paint glued around the samples for electro-conductive property; (b) shows the sample positions from the sample holder measured by scanning the vertical axis, and the horizontal axis shows the distance between three samples (the units is mm).

3.4.5.4 Obtain XMCD Spectra

If one makes two XAS measurements of a magnetic sample exposed to an applied magnetic field for opposite photon polarisations, I^+ and I^-, and then monitors the sample drain current while the photon energy is scanned over an absorption edge, a clear difference in line shape between the two spectra is revealed. Normally the L_3 and L_2 absorption edges are chosen as these are within a convenient energy range for most transition metals, are strong in nature and are well understood theoretically[88]. The difference between the two spectra from the XMCD opposing polarisations can be clearly seen by subtracting one spectrum from other. For spectra of a suitable shape and quality the sum rules can yield site and element specific values for the magnetic spin and orbital moments on a per atom basis.

In an XMCD experiment, a beam line with the ability to output circularly polarised light is fitted with an end station which allows the sample to be exposed simultaneously to the synchrotron beam and to an applied magnetic field, such as the system shows in figure 3.26. In this type of configuration, the magnetic field is applied parallel to the direction of the incident beam, and the end chamber is precisely positioned to ensure that the beam passes through holes drilled through the core of the magnet pole pieces. Other configurations for measuring XMCD spectra also exist. With third-generation light sources, such as the ESRF, the standard method of measurement uses superconducting magnetic from 1 to 14 Tesla. Here the field is flipped at the end of each entire energy scan, and the procedure repeated for the opposite polarisation. The resulting spectra is then averaged to minimise error. This is made possible by the high quality and intensity of the beam from the source, enabling the same measurement to be made in a fraction of the time.

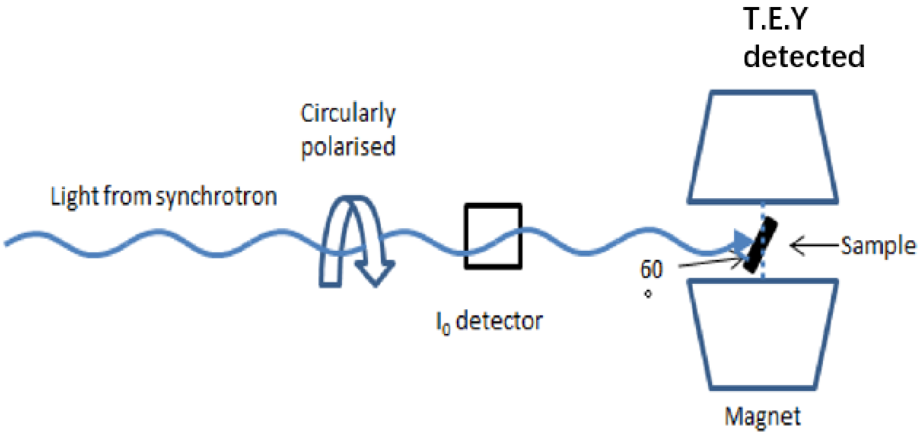

Figure 3.26 X-ray absorption spectroscopy (XAS) and XMCD experiments at the L_2 and L_3 absorption edges were performed at beam line I06 and I10 of the UK National Synchrotron Radiation Laboratory. The XAS experiments were carried out at 300K under an applied field ranging at 1T with total electron yield (TEY) detection. Circularly polarised X-rays with 100% degree of polarisation were used in normal incidence with respect to the sample plane and a 60-degree angle along the perpendicular direction.

All the chamber systems used in my work are equipped with the total electron yield (TEY) mechanism for the detection of the absorption spectra. This equipment measures the drain current between the sample on the sample holder and the chamber. The sample holder is a copper plate which is electrically isolated from the main body of the chamber and the manipulator to which it is attached. Copper is a convenient material for using in these studies as its absorption edges lie far outside of our regions of interest and thus our signals can be more easily identified.

3.4.5.5 Methods of XMCD Analysis

There is one major way for XMCD analysis: The Sum Rules analysis, which is widely used in XMCD measurement. Sum Rules analysis is a well-established quantitative approach, developed from a rigorous theoretical understanding of electromagnetism and the quantum world, which gives precise measurements of spin and orbital moments for the 3*d* transition materials. The theoretical approach had been pioneered by researchers in the early 1990s[89, 90]. By 1995, when Chen *et al* published their experimental confirmation[91], a definite method of applying the Sum Rules was developed. According to the Sum Rules, the orbital and spin magnetic moments can be determined from the XAS and XMCD spectra using the following equations:[92]

$$m_{orb} = -\frac{4\int_{L3+L2} \quad (\mu_+ - \mu_-)d\omega}{3\int_{L3+L2} \quad (\mu_+ + \mu_-)d\omega}(10 - n_{3d}) \tag{3.1}$$

$$m_{spin} = -\frac{6\int_{L3} \quad (\mu_+ - \mu_-)d\omega - 4\int_{L3+L2} \quad (\mu_+ - \mu_-)d\omega}{\int_{L3+L2} \quad (\mu_+ + \mu_-)d\omega}(10 - n_{3d})\left(1 + \frac{7\langle T_z\rangle}{2\langle S_z\rangle}\right)^{-1} \tag{3.2}$$

$$m_{ratio} = \frac{m_{orb}}{m_{spin}} \tag{3.3}$$

$$m_{total} = m_{orb} + m_{spin} \tag{3.4}$$

Where m_{orb}, m_{spin}, m_{ratio} and m_{total} are the orbital magnetic moment, spin magnetic moments, orbital to spin ratio and total magnetic moment in units of $u_b/atom$; n_{3d} is the 3*d* electron occupation number of the respective transition metal atom. The L_3 and L_2 denotes the integration range. $\langle T_z\rangle$ is the expectation value of the magnetic dipole operator and $\langle S_z\rangle$ is equal to half of m_{spin} in Hartree atomic units. To assist in the understanding and evaluation of the required XMCD integrals, Fig 3.27 gives an example that consists of three new terms *p*, *q*, and *r*, as the replacement of integrations in the above equations.

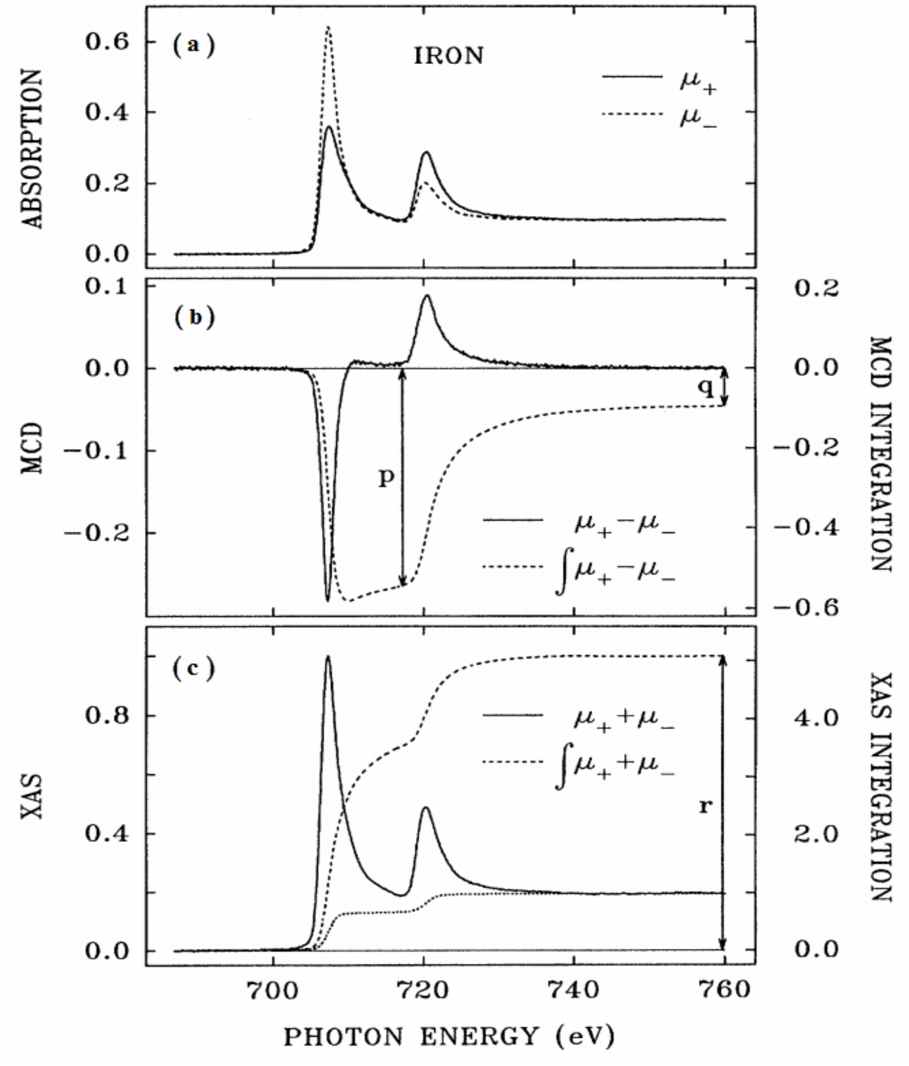

Figure 3.27 Graphs illustrating the practical application of the Sum Rules constants *p*, *q* and *r* which correspond to the integral of the dichroism spectra for the L3 edge, the integral of the dichroism spectra over both the L_3 and L_2 edges and the area of the summed XAS signal after removal of a stepped background respectively[91].

The dotted lines in figure 3.27 indicates the integration area of XMCD and XAS spectra, whereas

$$p = \int_{L3} (\mu_+ - \mu_-) d\omega \tag{3.5}$$

$$q = \int_{L3+L2} (\mu_+ - \mu_-) d\omega \tag{3.6}$$

$$r = \int_{L3+L2} (\mu_+ + \mu_-) d\omega \tag{3.7}$$

To further eliminate sources of error, the XMCD measurement normally performs a complete measurement of each sample a minimum of three times, and sometimes five times or more, so as to reduce the effects of any beam irregularities. The values calculated from these spectra can then be found and the standard deviation between the values quoted as the error. This error does not consider the margin of error within the sum rules themselves, such as the limitations in possible allowed transitions covered by the theory, j-j coupling and radial matrix elements[88], or the overlap between L_3 and L_2 edges. The uncertainty of these features is generally expected to fall within a 10% margin of error. Since there is, as yet, no mathematical way of accurately deriving the degree of error it generally thought safest to sum the standard deviation between spectra with the 10% expected error.

Chapter 4 Magnetic Properties of CoFeB Amorphous Films

4.1 CoFeB Amorphous Film on GaAs (100) Substrate

In this section, the CoFeB amorphous films have been synthesised on GaAs (100) and studied with both X-ray magnetic circular dichroism (XMCD) and transmission electron microscopy (TEM). As a result of this, we found that the ratios of the orbital to spin magnetic moments of both the Co and Fe in the ultrathin amorphous film were enhanced by more than 300% compared with those of the bulk crystalline Co and Fe. Specifically, a large orbital moment of 0.56 u_B from the Co atoms was observed. Simultaneously, the spin moment of the Co atoms was comparable to that of the bulk hcp Co. These results indicate that the large uniaxial magnetic anisotropy (UMA) observed in the ultrathin CoFeB film on GaAs (100) is related to the enhanced spin-orbital coupling of the Co atoms in the CoFeB. This work offers experimental evidence of the correlation between the UMA and the element specific spin and orbital moments in the CoFeB amorphous film on the GaAs (100) substrate.

4.1.1 Introduction

Owing to the development of next generation spintronics devices, such as magnetic random access memory (MRAM)[28-30] and spin field effect transistor (SpinFET)[31, 32], magnetic CoFeB amorphous alloys have attracted renewed interest. The structure and magnetic properties of various ferromagnetic (FM) thin films on top of semiconductors (SC), such as GaAs and Si, have been extensively studied over the last two decades, aiding the development of SpinFET[33, 93-96]. One of the most interesting discoveries is uniaxial magnetic anisotropy (UMA), observed in several FM/SC[31, 97], when the thickness of the FM layer is reduced to a nanometre scale. For example, the bcc Fe films on GaAs (100) substrates display the UMA from 1.4 nm to 11.5 nm[98], and for bcc CoFe on GaAs(100), the UMA has been found between 1.1 and 1.7 nm[99]. In the crystalline FM/SC systems, the magnetocrystalline anisotropy (MCA) might also change with the reduction of the film thickness[100]. Generally speaking, the UMA and MCA have been found to co-exist in most of the common FM/SC film systems[34]. To exclude the contribution from MCA, and thus focus on the UMA in the FM/SC film system, one effective method would be to alloy the ferromagnetic film with metalloid material to create an amorphous magnetic thin film. Approximately 20% Boron, alloyed with a CoFe compound, has been proven desirable. The additional Boron only slightly reduces the film's Curie temperature and saturation field, while destroy its crystallinity[101].

Recent research has proven that amorphous CoFeB films deposited on top of GaAs still exhibit the UMA[102, 103]. Several models have been proposed in order to explain the origin of the UMA in CoFeB/GaAs. These include bond-orientational anisotropy (BOA)[93, 104], Neel-Taniguchi directional pair-ordering model and random anisotropy model[105]. According to the BOA model, a medium-to-long range microstructural anisotropy is responsible for the UMA. The Neel-Taniguchi directional pair-ordering model introduces anisotropy via the dipole-like coupling between individual atom-pairs, leading to the anisotropic chemical ordering of near-neighbour atoms in a randomly oriented coordination. The random anisotropy model emphasises the break of the rotational symmetry of the Hamiltonian, which gives rise to the hard-magnetic behaviour even in random amorphous magnets. The origin of the UMA, it has been suggested, is due to the enhanced spin-orbit coupling and interface interaction[106], which is controlled by the orbital moment and the substrate crystal lattice[107].

The orbital moment has been found to have a more important role than the spin moment in giving rise to uniaxial magnetic anisotropy[108, 109]. Hindmarch *et al* [106] compared the UMA of CoFeB on different substrates of AlGaAs/GaAs and AlGaAs. They found a far stronger UMA (50 Oe) for AlGaAs/GaAs substrate, associated with an enhancement of the orbital to spin magnetic moments ratios m_{ratio} of both the Fe and Co sites. The uniaxial magnetic anisotropy field H_K of the UMA was found to be proportional to the m_{ratio}. Very recently, a larger H_K has been found, up to 270 Oe, in a CoFeB/GaAs (100) system, which is far stronger than any previously reported values[110]. In this project, I have studied the spin and orbital moments for a CoFeB/GaAs (100) system, using XMCD along with TEM and VSM. The large UMA observed in the CoFeB/GaAs (100) calls for a closer study of the spin and orbital moments and the spin-orbital coupling, which may play an important role in this system. It is well known that the orbital angular moment plays a dominant role in determining the strength of magnetocrystalline and uniaxial magnetic anisotropy[109]. The XMCD technique is capable of directly probing the element specific orbital and spin moments[108, 111-113].

4.1.2 Sample Growth

The $Co_{56}Fe_{24}B_{20}$ films were grown on GaAs (100) substrates by our collaborators in Nanjing University, China. Before the deposition of the CoFeB film, the substrate surface was etched and cleaned. First the substrate surface contaminants were removed using acetone, ethanol and deionized water. The second step was to remove the oxide layer by immersing the substrate into an HCl/H2O (1:1) solution for 50 seconds. The third step was to create a flat surface for film deposition, which was achieved by inducing substrate surface reconstruction. The cleaned substrate was loaded into an ultrahigh-vacuum chamber with a base pressure lower than 8×10^{-9} mbar and heated to 450 °C for 15 minutes, and a further 30 minutes at 580 °C (with the annealing pressure lower than 8×10^{-8} mbar) to achieve a clean and smooth surface[103]. The surface then cools to room temperature prior to film growth. The CoFeB films were prepared using DC magnetron sputtering deposition in 0.3 Pa argon (99.99%) at room temperature, with a base pressure lower than 8×10^{-6} Pa. A target containing $Co_{56}Fe_{24}B_{20}$ was used to deposit the magnetic CoFeB layer, with a thickness of 3.5 nm. Finally, a 2 nm Ta film was deposited as a capping layer to prevent the CoFeB film oxidising.

4.1.3 TEM Measurement results and Analysis

Structural properties of the grown films were studied using a JEOL 2200FS double aberration corrected (scanning) transmission electron microscope (S) TEM. Cross-sectional TEM specimens were prepared using conventional methods, including mechanical thinning and polishing, followed by Ar ion milling to achieve electron transparency[114].

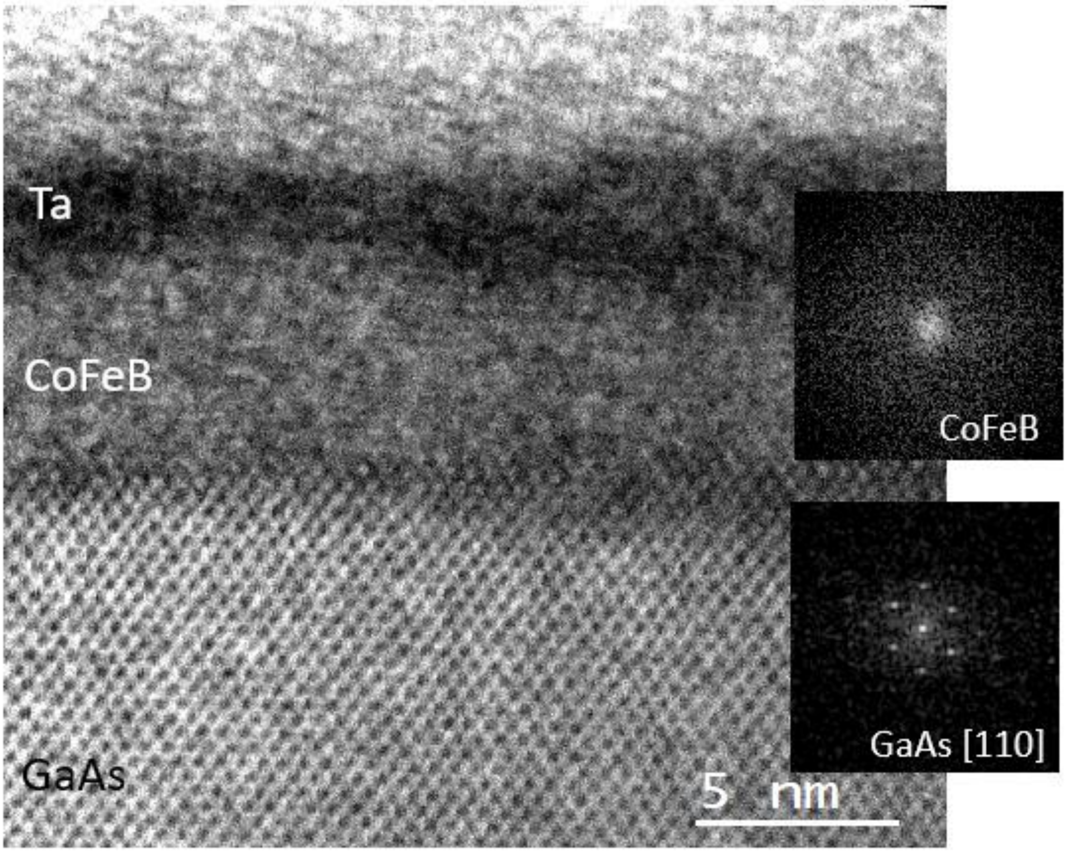

Figure 4.1 Cross-sectional bright-field scanning TEM micrograph of CoFeB/GaAs (100) in [110] view. The amorphous nature of the CoFeB is clearly shown by the inset digital diffractogram calculated from the film area in contrast to single crystal structure of the GaAs shown by atomic planes cross fringes and Bragg reflection in digital diffractogram (inset).

A high resolution cross-sectional TEM image of the structure is shown in Fig 4.1. The film thicknesses, of 3.5 nm for CoFeB and 2 nm for Ta, matches well the growth settings. The missing lattice fringes and the lack of distinctive rings or diffraction spots in the digital diffractogram from the film area show that the CoFeB film structure is amorphous. We also note, similarly to[115], that the formation of CoFeB crystalline monolayers at the very interface cannot be ruled out. Due to mass contrast, a clear distinction between the Ta and CoFeB can be observed, as well as between the CoFeB and GaAs, owing to the single crystal structure of the GaAs substrate and the amorphous structure of the CoFeB.

4.1.4 VSM Measurement results and Analysis

The in-plane magnetic hysteresis (*M*-*H*) loops were measured using a Vector Magnetometer Model 10 VSM and Vector measurement system. As a strong uniaxial anisotropy field (H_K), as large as 270 Oe, was expected[110], the VSM measurement was conducted using a maximum magnetic field of 400 Oe, to ensure the samples were fully saturated. The samples were measured at angles 0° and 90°, *i.e*. along the hard and easy axis. The magnetisation hysteresis loop of the CoFeB film along the out-of-plane direction was measured using a Polar MOKE. The saturation field was found be to as high as 12000 Oe.

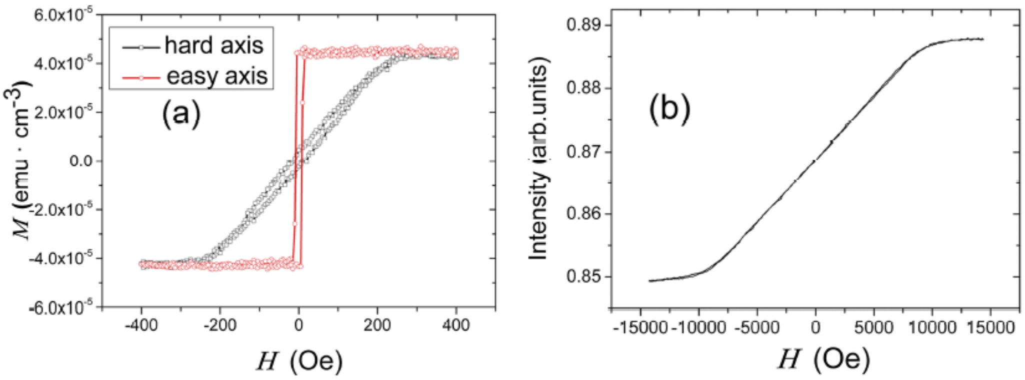

Figure 4.2 (a) In-plane M-H loops along both the EA (easy axis) and HA (hard axis) for the CoFeB film deposited on GaAs (100) substrates by VSM measurement. M and H represent the magnetic moment and applied magnetic field respectively. Figure 4.2 (b) shows the Polar MOKE loop for the out of plane direction of the CoFeB film.

Fig 4.2(a) shows the in-plane magnetic hysteresis (M-H) loop measured by VSM along the EA (easy axis) and HA (hard axis) axis of the CoFeB/GaAs (100) sample. The figure shows a clear UMA with a well-defined EA and HA. The value of the UMA field (H_K) can be obtained from the saturation field along the HA. Furthermore, the effective uniaxial anisotropy constant K_u^{eff} can be calculated by

$$K_u^{eff} = \frac{H_K \cdot M_S}{2} \tag{4.1}$$

where M_S is saturation magnetisation and H_K is the saturation field along the HA. It can be seen from the Fig 4.1(a) that H_K has a value of 270 Oe, confirming our previous observation of a large UMA in the CoFeB/GaAs (100) system. According to the saturation moment and thickness measurement, the value of M_S is estimated to be 977 *emu/cm*^{3}. The value of K_u^{eff} is thus determined to be 1.3×10^5 *erg*/c*m*^{3}, which is much larger than the values of 2×10^4 *erg*/c*m*^{3} and 8×10^4 *erg*/c*m*^{3} respectively reported by [101, 116]. It is also worth noting that the K_u^{eff} value of the CoFeB films on GaAs (100) achieved the largest value when compared to films grown on GaAs (110) and GaAs (111) substrate orientations, which achieved values of 1×10^4 *erg*/c*m*^{3} and 6×10^3 *erg*/c*m*^{3} respectively[96, 106, 117]. As Fig 4.1(b) indicates, the hysteresis loop for the CoFeB/GaAs (100) sample along the perpendicular (out of plane) direction, measured by a Polar MOKE, shows that the hard magnetisation axis is along this direction. As stated above, when making the XMCD measurement along the perpendicular direction, the applied magnetic field of 2000 Oe was not high enough to saturate the sample. From the perpendicular loop shown in figure 4.1(b), the saturation magnetic field is determined to be far higher at 10189 Oe. Hence, the data of spin and orbital moments from the XMCD have been scaled up by a factor of 5.09, as based on a comparison of the magnetisation at 2000 Oe and that at saturation. These figures are included in Table 4.1.

4.1.5 XMCD Measurement results and Analysis

XMCD measurements were performed at normal incidence to the Ta/CoFeB/GaAs (100) sample in the MAX Lab I1011 station. The XMCD spectra were measured at both positive and negative applied fields[91]. The data was collected by a Total Electron Yield (TEY) detector in the analysis chamber under a magnetic field of 2000 Oe. This was the operational limit of the magnet in the station, as the magnetic field should be set at a relatively low value in order to prevent the magnet overheating[118]. It is apparent, from Fig 4.1(b), that for the out-of-plane direction, the magnetic field used during the XMCD measurements was not sufficient to saturate the sample. It is for this reason that the spin and orbital moments obtained from the XMCD were scaled up to achieve the saturation value. During this work, all the measurements were performed at room temperature.

X-ray absorption spectra (XAS) of the Co and Fe L_2 and L_3 edges for CoFeB on GaAs (100) are shown in Fig 4.3(a) and (c) respectively. In this, u^+ and u^- are the absorption coefficients under magnetic fields antiparallel and parallel to the photon incident direction. Figure 4.3 shows the XMCD spectra for the Fe and Co L-edges of the CoFeB film. According to XMCD sum rules, the orbital (m_{orb}) and spin (m_{spin}) magnetic moments and the ratio (m_{ratio}) of m_{orb} to m_{spin} can be determined from XAS and XMCD spectra using the equations from 3.1 to 3.7, mentioned previously in chapter 3. The spin and orbital moments are also dependent on the d-band hole density in CoFeB and the intensity of the polarised x-ray in the XMCD measurement.

It should be noted that there is a degree of controversy regarding the 3*d* hole numbers of Fe and Co in magnetic amorphous films. While Cui *et al* [92] use the m_{orb}/n_h to present their data, Kanai *et al* [119] have calculated the hole numbers of Co and Fe in the amorphous films by first-principles calculations, and have found the similar values to those of the bulk Fe and Co films[117, 119]. In this work, we have used the values of n_{3d} for Fe as 6.61 and Co as 7.51, taken from [119], to calculate the spin and orbital moment of Co and Fe in the CoFeB film.

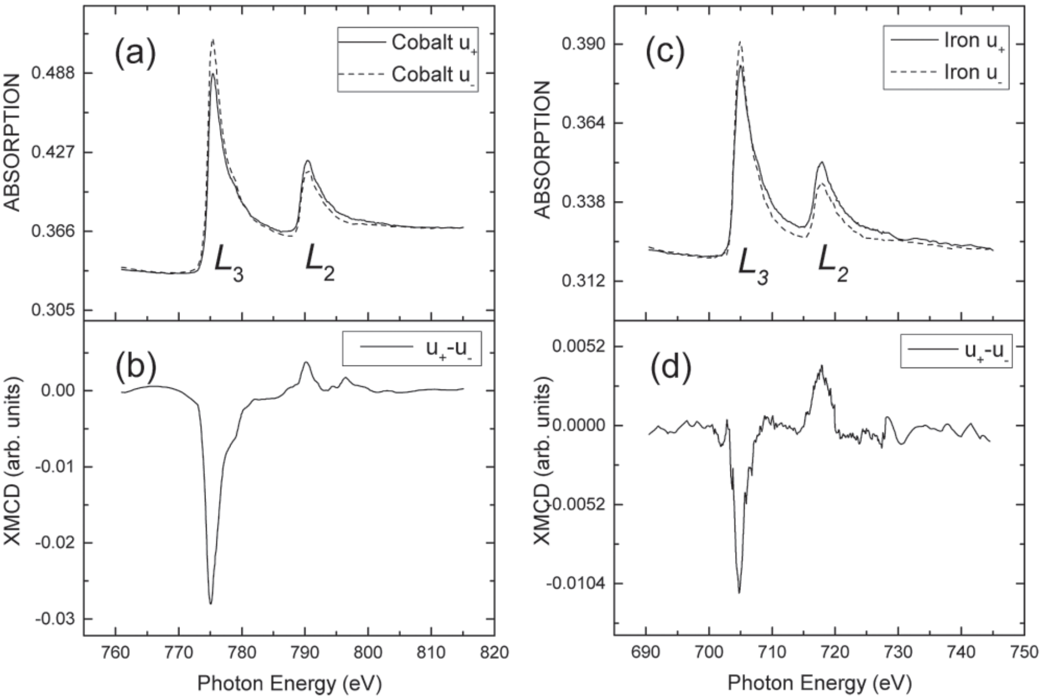

Figure 4.3 XAS and XMCD spectra of the Co and Fe atoms at the L_2 and L_3 edges in the CoFeB/GaAs (100): (a) and (c) are the XAS absorption spectra and (b) and (d) are the XMCD for Co and Fe, respectively.

Table 4.1 Orbital moments, spin moments and orbit to spin ratio of the Fe and Co from various CoFeB samples (the first one is my sample, and the others are from literature) in units of $u_B/atom$.

Sample	Saturation magnetic field for HA (Oe)	Element	$m_{orb}(u_B)$	$m_{spin}(u_B)$	m_{ratio}
Ta/$Co_{56}Fe_{24}B_{20}$(3.5nm)/ GaAs (100)	270	Fe	0.30 ± 0.03	1.17 ± 0.03	0.26
		Co	0.56 ± 0.03	1.53 ± 0.03	0.36
Ta/$Co_{40}Fe_{40}B_{20}$(3.5nm)/ GaAs (100)/AlGaAs (100) (Ref.[120])	50	Fe			0.45
		Co			0.38
Ta/$Co_{40}Fe_{40}B_{20}$(3.5nm)/ AlGaAs (100) (Ref.[120])	25	Fe			0.34
		Co			0.19
Ta/$Co_{40}Fe_{40}B_{20}$(2.0nm)/ MgO (Ref.[119])		Fe	0.27 ± 0.03	1.77 ± 0.03	0.15
		Co	0.17 ± 0.03	0.90 ± 0.03	0.19
Bulk bcc Fe (Ref.[121, 122])	100	Fe	0.09 ± 0.05	1.98 ± 0.05	0.04
Bulk hcp Co (Ref.[121, 122])	450	Co	0.15 ± 0.05	1.55 ± 0.05	0.10

The values of m_{orb}, m_{spin} and m_{ratio} are all determined from the XMCD data, and the results are listed in Table 4.1, along with those reported in the literature. Firstly, by comparing the amorphous films and the crystalline elements, one result can be confirmed: the orbital moments of the Fe and Co in the amorphous films are larger than that of the crystalline bcc Fe and hcp Co. While the spin moment of the Fe atoms in the

CoFeB is much reduced, compared with that of bcc Fe, the spin moment of the Co atoms remains as large as $1.53u_B$, which is almost the same as that of the hcp Co. As shown in Table 4.1, the orbital to spin ratios m_{ratio} of the Co and Fe in the amorphous CoFeB film have been enhanced by 300%, compared with those of the hcp Co and the bcc Fe. Previous work indicates that the stronger UMA for CoFeB on GaAs(100)/AlGaAs(100) is due to the enhancement of the m_{ratio}, as it was found that the m_{ratio} increased from 0.19 to 0.38 for Co and 0.34 to 0.45 for Fe when the UMA was increased from 25 Oe to 50 Oe[101, 110, 119]. Though the UMA in our sample was found to be as large as 270 Oe, the values of the m_{ratio} show a comparable enhancement of 0.36 for Co and 0.26 for Fe. This shows that the UMA is associated with the enhancement of the orbital moments, but does not vary linearly with the m_{ratio}.

One of the most striking results observed from the measurement (as shown in Table 4.1) is that the spin and orbital moments of the Co atoms are significantly larger than those of the Fe atoms. When considering the value of the m_{ratio}, we can see that the Co atoms also have a larger value than that of the Fe atoms. The orbital moment of the Co atom in the CoFeB has been enhanced by more than 370%, in comparison to the orbital moment of the crystalline hcp Co. This suggests that in the CoFeB (100) amorphous film, the Co atoms at the interface with the GaAs contribute more than Fe to the UMA. Our results indicate that the large UMA observed in the CoFeB (100)/GaAs (100) system comes from the large spin-orbit coupling of the Co atoms.

Spin-orbital coupling is a desired property in terms of the controllability by an electric field in spintronic operation. The orbital moment of the Co atoms in the CoFeB/GaAs (100) was found to be as large as $0.56u_B$, which is the largest orbital moment reported in any amorphous magnetic alloys, to the best of our knowledge.

4.1.6 Summary of Findings

In this part, we have investigated the uniaxial magnetic anisotropy and the element specific spin and orbital moments in the CoFeB/GaAs (100) system by way of magnetisation measurement, XMCD measurement and sum rule calculations. The results obtained by VSM measurements confirmed that the UMA can rise as high as 270 Oe, which is among the largest UMA observed in any CoFeB amorphous alloys. XMCD measurements revealed that the UMA correlates with a strong spin-orbit coupling, related to the enhanced orbital to spin moment ratios of both Fe and Co in the CoFeB. More importantly, the spin moment of the Co was found to remain as large as that of the crystalline hcp Co, and the orbital moment is enhanced by more than 370%. This suggests the dominant contribution of the spin-orbit coupling of the Co atoms to the UMA in the CoFeB/GaAs (100) amorphous film. These results would be useful for understanding the fundamental magnetic properties of the amorphous CoFeB films, which could be important for the application of this class of materials in next generation spintronic devices, including MRAM and SpinFET.

4.2 Magnetic Properties of CoFeB/MgO Structure

In this section, the structure of CoFeB/MgO has been researched using X-ray magnetic circular dichroism (XMCD) and vibrating sample magnetometer (VSM). We have observed that the ratios of the orbital to spin magnetic moments of Co atoms in CoFeB/MgO structure films with PMA have been enhanced by more than 200%, compared with those of the samples without PMA or a MgO layer. More importantly, a large orbital moment of $0.30u_B$ from Co atoms has been observed and, at same time, the orbital moment of the Fe atoms remains comparable to others. The results indicate that the origin of PMA observed in CoFeB/MgO structure is related to the increased spin-orbital coupling of Co atoms. This work offers experimental evidence of the correlation between PMA and the element specific spin and orbital moments in CoFeB/MgO systems.

4.2.1 Introduction

A major breakthrough in MRAM is the discovery of perpendicular magnetised CoFeB films, sandwiched by MgO and Ta layers, which exhibit not only the perpendicular magnetic anisotropy, but also strong orbital moment and spin-orbital coupling[123, 124]. At the same time, current-induced spin-transfer torque (STT) is very important in high density magnetic media and spintronics devices[125-129]. Because of the importance of lowering the energy consumption, it is necessary to discover a method to reduce the critical current required to switch the spin direction in STT-MRAM application. The perpendicular magnetic anisotropy (PMA) materials, integrated into a magnetic tunnel junction (MTJ)[130-132], allow for a small critical current density for current-induced magnetisation switching[133-135]. These materials are found to have a good balance of thermal stability and low magnetic anisotropy energy. In this part of the project, I have studied the effect of the layered structure and in particularly the role of the element-specific orbital moments on the PMA in Ta/CoFeB/MgO structures.

4.2.2 Sample Growth

We prepared three samples, these three samples were prepared by our collaborators in Beijing Institute of Physics, China. The first was substrate/Ta (5)/MgO (3)/CoFeB (1.2)/Ta (5) named sample A. The second was substrate/Ta (5)/CoFeB (1.2)/MgO (3)/CoFeB (1.2)/Ta (5) named sample B. The last was substrate/Ta (5)/CoFeB (1.2)/Ta (5) named sample C. All the numbers indicate thickness in nanometres.

The capping layer and $Co_{40}Fe_{40}B_{20}$ films were deposited on Si (001)/SiO_2 substrate by dc sputtering, whereas the MgO layer was deposited using RF sputtering. The background vacuum was about 4×10^{-5} Pa and the working argon pressure was 0.5 Pa.

After the thin film was deposited, a post-annealing process, at 300 °C in a vacuum at 4 × 10^{-5} Pa, was performed for half an hour on both samples.

4.2.3 VSM Measurement and Analysis

The magnetic hysteresis loops of all the samples were measured with both the in-plane and perpendicular magnetic fields using a Vector Magnetometer Model 10 VSM, shown in figure 4.4. The PMA effect was observed in sample A and B: the in-plane loops show the hard axis and the perpendicular loops show the easy axis. Meanwhile, in sample C, the film without the MgO layer, there is no PMA effect. The VSM measurement was conducted using a maximum magnetic field of 15000 Oe to ensure the samples were fully saturated.

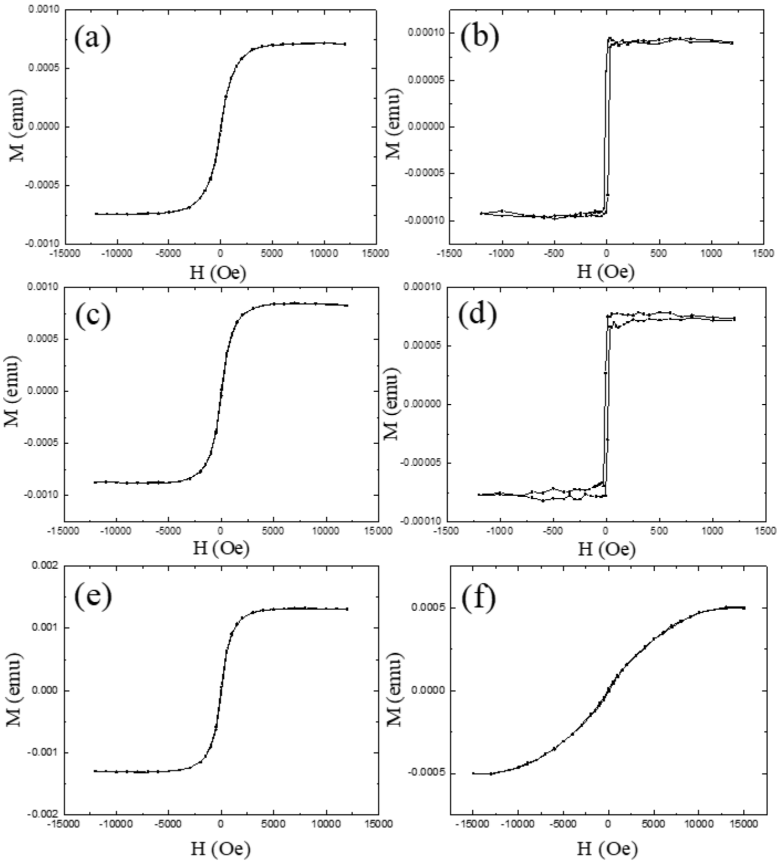

Figure 4.4 Both in-plane [011] and perpendicular hysteresis loops of all three samples. (a), (c) and (e) are the in-plane hysteresis loops for A, B and C, respectively. (b), (d) and (f) are the perpendicular hysteresis loops for A, B and C, respectively.

Figure 4.4(b), (d) and (f) show the perpendicular hysteresis loops for A, B and C. The figures show the clear difference between the samples. The loops for samples A and B show the easy axis on perpendicular direction, and the saturation field along the sample hard axis is 6500 Oe and 8000 Oe for A and B, respectively. The loop for sample C, the CoFeB without the MgO layer, shows the hard axis on perpendicular direction, and the saturation field is 13000 Oe. Furthermore, the effective magnetic anisotropy K_u^{eff} can be calculated by equation 4.1. According to the saturation moment and thickness measurement, the saturation magnetisation M_S can be calculated using [136]

$$M_S = M/V \tag{4.2}$$

where M is the saturated magnetic moment and V is the volume of samples.

Table 4.2 the values of saturation field, saturation magnetisation and the effective magnetic anisotropy are shown for three samples.

Sample	Saturation field for HA	M_S	K_u^{eff}
Ta/MgO/CoFeB/Ta (A)	6500 Oe	381 emu/cm^3	+1.24 $Merg/cm^3$
Ta/CoFeB/MgO/CoFeB/Ta (B)	8000 Oe	456 emu/cm^3	+1.60 $Merg/cm^3$
Ta/CoFeB/Ta (C)	13000 Oe	309 emu/cm^3	-2.01 $Merg/cm^3$

It can be seen from Table 4.2 that the values of the saturation field, saturation magnetisation and effective magnetic anisotropy for sample A are 6500 Oe, 381 emu/cm^3 and 1.24 $Merg/cm^3$ respectively, which are very similar values to the previous report[137]. There are two layers of CoFeB separated by the MgO layer in sample B, yet it still shows the PMA. According to the previous results, there are two key points needed to form the PMA with CoFeB[132]. One is a very thin CoFeB film, under 1.5 nm and the other is the MgO layer, which has induced the CoFeB to form the PMA. The thickness of CoFeB in sample B is 2.2nm, so, according to previous researches[119], it cannot form the PMA. However, when the CoFeB layer was divided into two parts, the PMA was shown, as in figure 4.4 (c) and (d), and the M_S and K_u^{eff} are both slightly enhanced in sample B. It should be noted that the value of K_u^{eff} for sample C marked as the negative value, which because the sample C has not formed the PMA, the values of effective magnetic anisotropy were calculated for researching the PMA, so for distinguishing the samples with and without PMA, the value of K_u^{eff} for sample A and B marked as the positive value and sample C marked as the negative value. The values of the saturation field, saturation magnetisation and effective magnetic anisotropy for sample C are similar to the values reported before[117]. When comparing samples A and B, it is apparent that the saturation field, M_S and K_u^{eff} values for sample B were enhanced. The saturation field along perpendicular direction increased from 6500 to 7000 Oe, and the M_S and K_u^{eff} improved by 20%.

4.2.4 XMCD Measurement Results and Analysis

XMCD measurements were performed at normal incidence on the CoFeB/MgO structure samples in the I06 station of the Diamond Light Source. The XMCD spectra were measured at both the positive and negative applied fields. The data were collected by a Total Electron Yield (TEY) detector in the analysis chamber at a magnetic field of 2T. The 2T magnetic field used during the XMCD measurement fully saturated the samples. During this work, all measurements were performed at 300K.

X-ray absorption spectra (XAS) of the Co and Fe L_2 and L_3 edges for CoFeB/MgO structure are shown in Fig 4.5. In this, u^+ and u^- are the absorption coefficients under antiparallel and parallel magnetic fields to the photon incident direction. Figure 4.5 shows the XMCD spectra for the Fe and Co L-edges of the various CoFeB films. Figure 4.5 (a), (c) and (e) indicate the Co element XMCD diagrams, where the L_3 photon energy of Co is around 778.4 eV. Figure 4.5 (b), (d) and (f) give the XMCD diagrams for Fe, where the L_3 photon energy of Fe is around 707.4 eV. According to XMCD sum rules, the orbital (m_{orb}) and spin (m_{spin}) magnetic moments and the ratio (m_{ratio}) of m_{orb} to m_{spin} can be determined from XAS and XMCD spectra by the equations from 3.1 to 3.7, which were previously illustrated in chapter 3. The spin and orbital moments are also dependent on the d-band hole density in CoFeB and the intensity of the polarised x-ray in the XMCD measurement. In this work, we have used the n_{3d} values from [60] - 6.61 for Fe and and 7.51 for Co - to calculate the spin and orbital moment of Co and Fe in the CoFeB film.

Table 4.3 Orbital moments, spin moments and orbit to spin ratio of the Fe and Co from various CoFeB samples in units of $u_B/atom$

Sample	Element	$m_{orb}(u_B)$	$m_{spin}(u_B)$	m_{ratio}
Ta/MgO/$Co_{40}Fe_{40}B_{20}$(1.2nm)/Ta (A)	Fe	0.31 ± 0.02	1.69 ± 0.02	0.19
	Co	0.30 ± 0.04	0.59 ± 0.01	0.52
Ta/$Co_{40}Fe_{40}B_{20}$(1.2nm)/MgO/CoFeB(1nm)/Ta (B)	Fe	0.26 ± 0.03	1.61 ± 0.03	0.16
	Co	0.30 ± 0.01	0.58 ± 0.02	0.51
Ta/$Co_{40}Fe_{40}B_{20}$(1.2nm)/Ta (C)	Fe	0.20 ± 0.04	1.68 ± 0.02	0.12
	Co	0.17 ± 0.05	0.60 ± 0.03	0.28
Ta/$Co_{40}Fe_{40}B_{20}$(2.0nm)/MgO/Ta (Ref.[119])	Fe	0.27 ± 0.03	1.77 ± 0.03	0.15
	Co	0.17 ± 0.03	0.90 ± 0.03	0.19

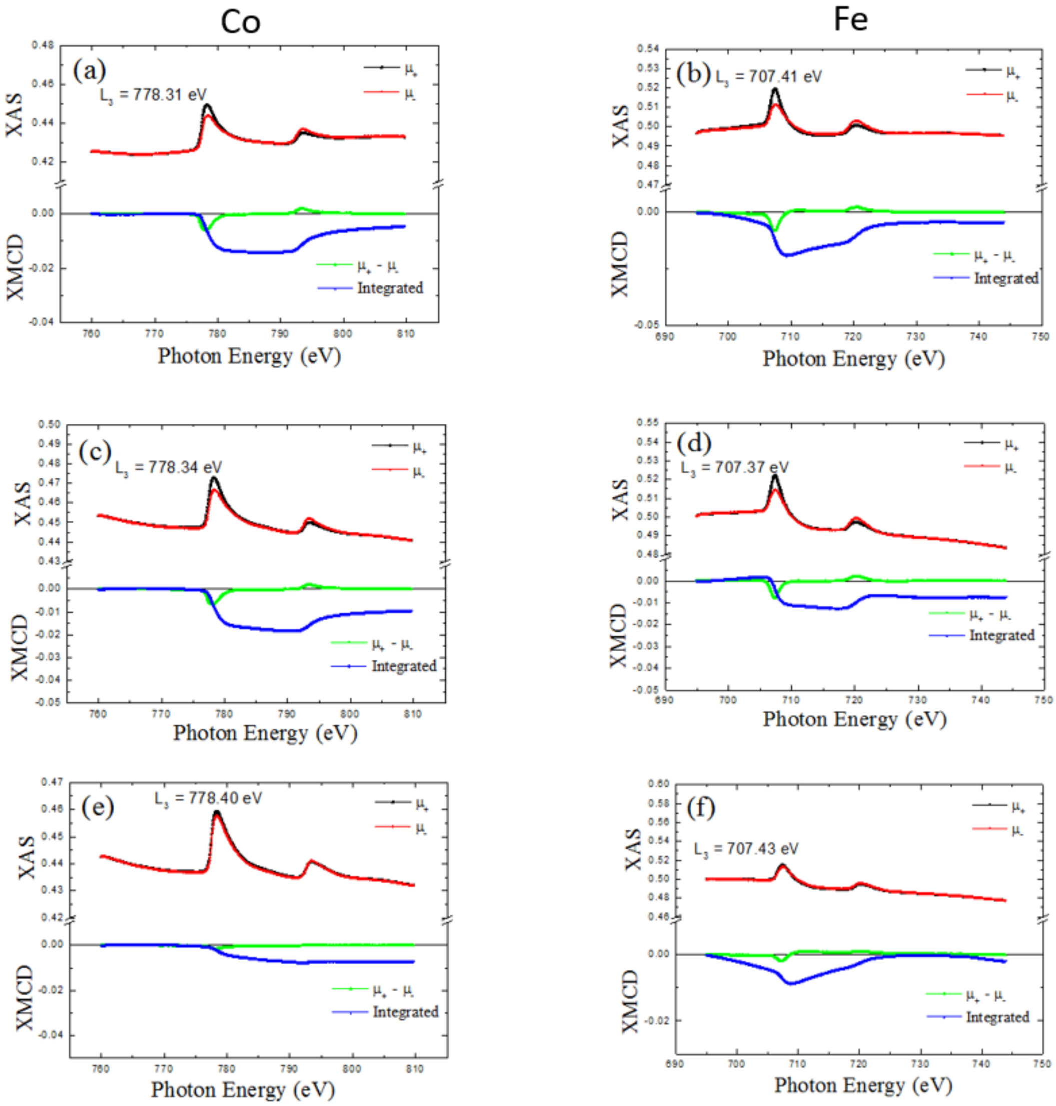

Figure 4.5 XAS and XMCD spectra of the Co and Fe atoms at the L_2 and L_3 edges in the CoFeB various films: (a), (c) and (e) are the XMCD for Co; (b), (d) and (f) are the XMCD for Fe.

The values of m_{orb}, m_{spin} and m_{ratio} are all determined from the XMCD data, and the results are listed in Table 4.3, along with some reported in the literature. Firstly, by drawing a comparison between the films with MgO (A and B) that formed PMA and the film (C) without MgO, one result can be confirmed: the orbital moments of the Fe and Co elements in both samples with the MgO layer which formed PMA are larger than those of sample C (without the MgO layer). This is especially pronounced in the orbital moment of Co, which is shows an almost 200% enhancement in samples A and B compared with sample C. The spin moments of both Co and Fe in the three samples do not show such dramatic changes, with values around $1.68u_B$ for Fe and $0.58u_B$ for Co.

Previous research has indicated that a CoFeB layer in CoFeB/MgO as thick as 2nm would not be able form the PMA, and gave the value of orbital and spin moments. However, in my work, the CoFeB layer was 2.2nm, but when divided into two parts it did form the PMA. By comparing the value of moments of sample B with previous work[119], it can be seen that the orbital moments of Fe have not dramatically changed, but the orbital moments of Co have increased from $0.17u_B$ to $0.30u_B$. It should be noted that the value for the Co orbital moment from Shun Kanai el is $0.17u_B$, which is the same as the value from sample C. Neither of these two samples have the PMA, and the one with MgO has only slightly increased the orbital moment of Fe, but not changed the orbital moment of Co. This suggests that the enhancement of Co orbital moments is associated with the origin of PMA in the CoFeB/MgO system.

Spin-orbital coupling is a desired property in terms of the ability to use an electric field to control spintronic operation. One of the most striking results from the measurement (as shown in Table 4.3) is that the orbital moments and m_{ratio} of Co atoms are significantly larger than those of Fe atoms. This suggests the Co atoms at the interface with MgO have more contribution than Fe atoms in spin-orbital couplings. The spin to orbital ratio of Co atoms in samples A and B (which formed the PMA) is $0.52u_B$. This shows an enhancement by more than 200% compared to those of sample C and previous work which did not form the PMA, while the spin to orbital ratios of Fe have not shown significant change in all samples. This study suggests that the strong PMA in the CoFeB/MgO system is related to the large enhancement of the orbital moment of Co element rather than Fe. This is consistent with what observed in the CoFeB/GaAs system, where the strong UMA is related to the enhanced orbital moment of Co.

4.2.5 Summary of Findings

In conclusion, we have investigated perpendicular magnetic anisotropy and the element specific spin and orbital moments in the CoFeB/MgO system by using magnetisation measurement, XMCD measurement and sum rule calculations. The results obtained by VSM measurements confirmed that the PMA can be found in a split layer of 2.2 nm CoFeB, with a MgO layer, and the saturation field along perpendicular direction can rise as high as 7000 Oe, which enhanced 10% compared with sample A, while the M_S and K_u^{eff} are enhanced by 20%. XMCD measurement revealed that the PMA is correlated with the strong spin-orbital coupling of Co atoms, related to the enhanced orbital to spin moment ratios of Co atoms in CoFeB. More importantly, compared with the samples without PMA (sample C and previous work), the sample with the PMA (sample A and B) shows the orbital moment of Co atoms enhanced from $0.17u_B$ in sample C to $0.30u_B$ in samples A and B. Meanwhile the orbital moment of Fe atoms has not shown significant change, suggesting the dominant contribution of spin-orbital moment coupling of Co atoms to PMA in CoFeB/MgO structure. According to our findings, these results would be very useful for understanding the origin of PMA in CoFeB/MgO films, which could, in turn, be very important for later researches into new generation spintronics devices like STT- MRAM.

Chapter 5 Growth, Structure and Magnetic properties of Fe/Cr/GaAs (100) Systems

5.1 Cr/Fe/Cr/GaAs (100)

5.1.1 Introduction

Interface magnetism in ferromagnetic metal (FM)/ semiconductor(SC) heterostructures is still an important topic for the study of fundamental magnetic properties of ultrathin films, and for the development of next generation magnetoelectronic devices[138-143]. At present, semiconductor device technology is only used for the presence or the absence of charge, whereas in the future, electronic spin application, in particular spin injection, will be important for performance promotion. As such, it is necessary to investigate the interface magnetism between FM and SC[144-146].

An Fe/GaAs structure is used in a device because the lattice mismatch between Fe and GaAs is very small compared to other transition metal-III-V semiconductor combinations; at present, GaAs is the most popular semiconductor in use[47, 147]. In previous research, high quality single crystalline Fe on GaAs substrate were grown without any dead layer[46, 148]. Xu *et al* [33] used in situ magneto-optical Kerr effect measurements to find that the earliest UMA was shown when Fe was 4.8ML on GaAs substrate. One issue which has not yet been clarified with regards to the Fe/GaAs system, is the origin of in-plane uniaxial magnetic anisotropy. Some researchers have indicated that UMA originates from a volume effect induced by the angle of incidence of Fe atomics flux, and that the lattice mismatch related film stress might be important for magnetic behaviour close to the interface[149-153]. Another research, however, presented results which postulated that the Fe-As chemical bonding is the key factor which influences UMA. In this case, the Fe and As atom densities which are present appear to be large enough to overcome the problems which potentially arise from the presence of Fe-As bonds. This would cause the quenching of the Fe moment were there to be two or more As bonds per Fe atom, irrespective of the number of Fe nearest neighbours[32, 45, 112, 154].

In this work, to determine the origin of UMA, Cr films of different thicknesses were inserted between the GaAs substrate and 10ML Fe films. Cr layer is an antiferromagnetic film which is normally used in the investigation of antiparallel coupling[155-157]. Fe and Cr have a similar lattice constant, meaning the Cr interlayer only slightly affects the formation of the Fe structure, meaning that if the lattice mismatch related film stress existed and induced UMA, the Cr interlayer would slightly influence UMA. We have carried out the XMCD, RHEED, SQUID-VSM and TEM investigations into the properties of ultrathin films grown on substrate with various Cr interlayers. Lattice mismatch or film stain will induce the formation of poly-crystalline structure, but from TEM image, it is a clear evidence that both Cr interlayer and 10 ML Fe film are all single-crystalline structure. From our studies, we conclude that UMA is from the interface interaction between Fe and As atoms, and rule out the reason from either lattice mismatch or film stain.

5.1.2 Sample Growth

10 ML Fe films with Cr interlayers of different thickness were grown on GaAs (100) substrates. Before the deposition of the Cr interlayer, the substrate surface was etched and cleaned. Firstly, any contaminants on the substrate surface were removed using acetone, iso-propyl alcohol (IPA) and deionized water. The second step was to remove the oxide layer by immersing the substrate into an $H_2SO_4/H_2O_2/H_2O$ (4:1:1) solution for 45 seconds. All these were performed in a level 100 clean room to prevent any contamination by dust particles. The third step was to create a flat surface for film deposition. The etched substrate was immediately transferred into an MBE chamber with a base pressure of 2.3×10^{-10} mbar, before the substrate was treated with ion-milling before annealing (low energy Argon ion beams were sputtered onto the

substrate surface for 30 minutes so that they gently removed a thin layer of surface material, exposing the virgin layer of the substrate). The final step is annealing, whereby the substrate was required to be annealed at 480°C (at an annealing pressure lower than 8×10^{-9} mbar) for 60 minutes to further remove natural oxides and create the surface reconstruction[93]. The surface then cooled to room temperature prior to film growth. The Cr interlayer and 10 ML Fe layers were grown by the two different source evaporators in the MBE system, where the pressure was lower than 2.1×10^{-9} mbar. Finally, a 3 nm Cr capping layer was deposited to prevent the Fe film from oxidisation.

5.1.3 RHEED Patterns and Analysis

Since the substrates remain in a UHV environment, only way to examine the surface quality in our MBE system is to observe the RHEED (Reflection High Energy Electron Diffraction) patterns. The advantages of RHEED are mainly that it is in-situ, fast, and surface sensitive. Multiple RHEED patterns were recorded throughout the film deposition for monitoring purposes.

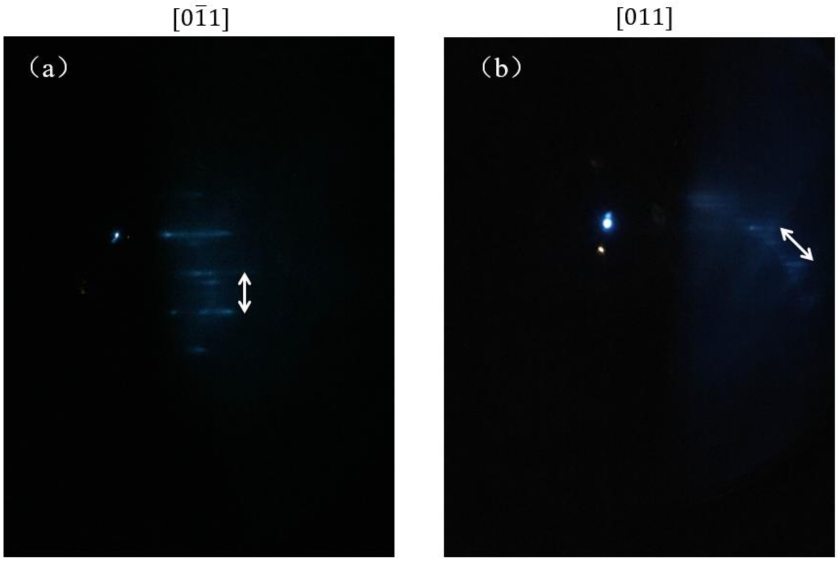

Figure 5.1 (a) and (b) indicate the RHEED patterns for $[0\bar{1}1]$ and [011] directions of GaAs (100) substrate respectively. There is a well-ordered (4×6) reconstruction.

Figure 5.1 (a) and (b) show the GaAs (100) substrate patterns from $[0\bar{1}1]$ and [011] directions respectively. All GaAs (100) substrates experienced the cleaning, ion-milling and annealing process. The same setting processes ensure that all substrates have formed the similar reconstruction. Figure 5.1 (a) shows four short lines between the two major lines, and Figure 5.1 (b) shows six short lines. From this two-directional observation, it can be confirmed that the substrate indicates the typical 4×6 Ga diffusion reconstruction[33]. Kneedler *et al* [47] demonstrated that the onset of ferromagnetism occurred at 6 ML when Fe was grown on both GaAs (001)-(2×4) and (4×4) substrates. 4×6 GaAs reconstruction may have some benefits compared to the other reconstructions: first, it removed the dead layer between the GaAs substrate and film, and second, when the Fe film grows on this substrate it will form UMA as early as 4.8 ML.

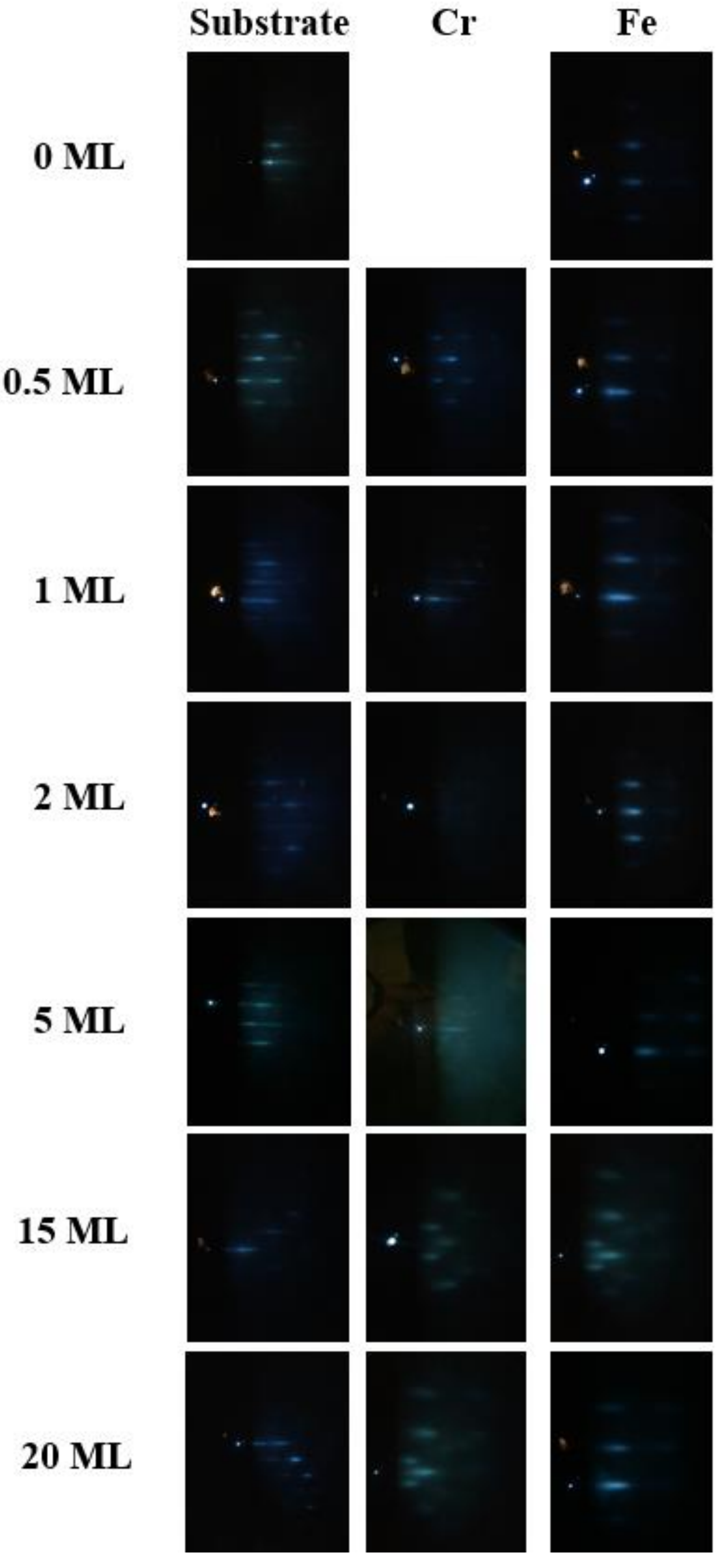

Figure 5.2 shows the RHEED patterns from GaAs (100) substrates ([0$\bar{1}$1] view), and the substrate RHEED patterns are slightly different, but they are all the single crystalline structure. The various thickness Cr interlayers and 10 ML Fe films which grow on the Cr interlayer. The thickness of the Cr interlayer ranges from 0ML to 20ML while the Fe thickness remains at 10ML.

Figure 5.2 shows the RHEED images of GaAs (100) substrates, the different thicknesses of Cr interlayer and 10 ML Fe films which grow on the Cr interlayer. From the RHEED patterns of all 10 ML Fe films, one result which can be confirmed is that the all 10 ML Fe films have a single crystalline structure, and the different thicknesses of Cr have not changed the structure of 10 ML Fe films. The lattice constant of 2.87Å for Fe is almost exactly equal to half of GaAs (5.65 Å). The lattice constant of Cr is 2.88 Å, which is almost no different to the Fe value, meaning that the lattice mismatch between Fe and Cr is very small. Even when the thickness of the Cr interlayer is 20 ML, 10 ML Fe remains as a single crystalline structure, and the Cr interlayer makes no contribution to the formation of a Fe single crystalline structure[31, 158]. The RHEED patterns for the various thicknesses of Cr interlayer are also very interesting. Between 0.5 ML and 1 ML, the RHEED images show a single crystalline structure, which might come from the substrate. When the thickness achieved is 2 ML, the RHEED pattern disappears, showing the island growth. Finally, between 5 ML and 20 ML, the RHEED images show a single crystalline structure again, especially when the Cr thickness was at 5 ML, the point at which the RHEED pattern changed to a single crystalline structure, showing that the Cr films are continuous after 5 ML.

In order to research the change of the Cr interlayer RHEED patterns in detail, especially when the thickness of the Cr interlayer is 5 ML, we grew a special sample, where the Cr interlayer was developed half monolayer by half monolayer, and which focused around 5 ML, before growing to 10 ML Fe on the Cr layer. The RHEED patterns can be found in Figure 5.3. For the interlayer from 0.5 ML to 1 ML Cr, only a small area of GaAs (100) substrate is covered, meaning that from the screen the substrate RHEED pattern can still be seen, but these two RHEED patterns become blurry due to the increased Cr interlayer. From 2 ML to 4.5 ML, the RHEED patterns from the screen is fully dark, and the Cr interlayer should be in progress, which is from an island film to be a continuous film (a single crystalline film). This means the RHEED patterns are not evident. It is not until the Cr interlayer grows to 5 ML that the single crystalline

RHEED pattern of Cr can be seen from the screen, and even then the pattern is week on the screen. The interlayer Cr become a single crystalline film from 5 ML, and it fully covers the GaAs (100) substrate, blocking UMA from interface. That UMA in Fe-GaAs (100) is from the interface interaction and not from the stress induced is an important discovery. It is easy to see that the Cr interlayer films (from 5.5 to 7 ML) are all single crystalline due to the clear RHEED patterns, and these RHEED patterns become clearer compared to the RHEED pattern from the 5 ML Cr interlayer. The last RHEED pattern is from 10 ML Fe growth on 5 ML Cr interlayer, which shows this 10 ML Fe film is still a single crystalline film from the RHEED pattern.

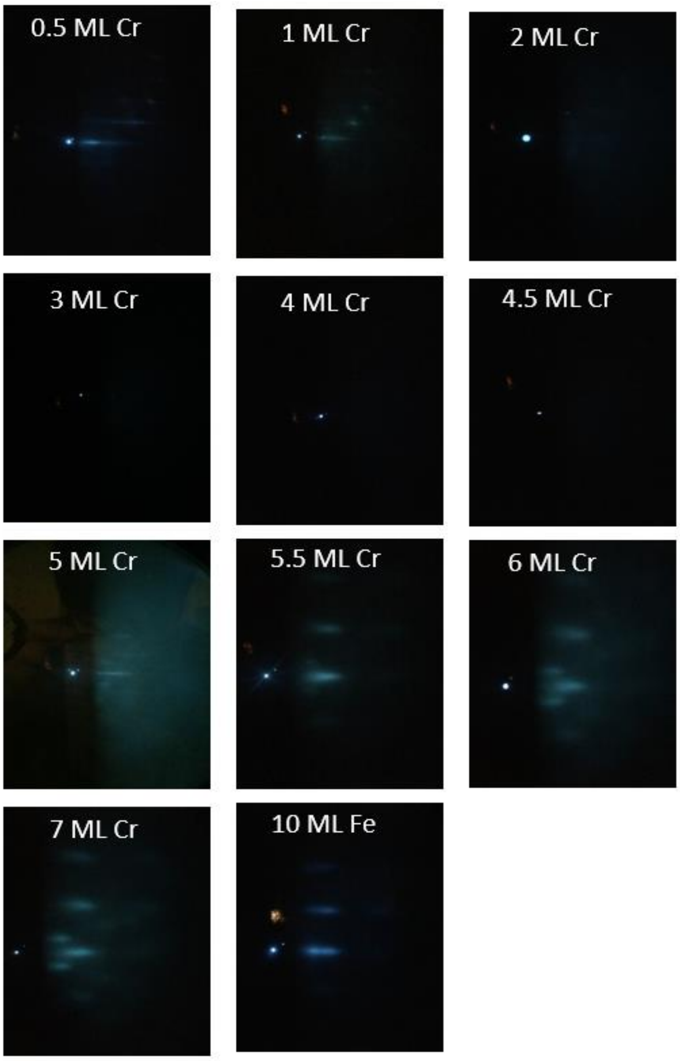

Figure 5.3 indicates the RHEED patterns of Cr thickness change from 0.5 ML to 7 ML, and then grow a 10 ML Fe film on it. The 10 ML Fe shows the single crystalline structure from the RHEED pattern.

The reason for using Cr as an interlayer is that the lattice mismatch between Fe and Cr is quite small, and so Cr cannot be a major reason which influences the Fe lattice structure. Thus, the origin of UMA is not from the stress induced because the structure of Fe is not change compared to the 0 ML Cr interlayer RHEED pattern. This means the only reason that UMA can be changed is from the interface, meaning that interface bonding is the only reason for the formation of UMA.

5.1.4 VSM Measurement and Analysis

The in-plane magnetic hysteresis (M-H) loops were measured using a superconducting quantum interference device-vibrating sample magnetometer (SQUID-VSM; Quantum Design) system. It measured at 4000 Oe to ensure the film saturated. A decreased trend in the uniaxial magnetic anisotropy field (H_k) was found, wherein the value of the saturation field dropped from 1799.295 Oe to 56.804 Oe by the increasing Cr interlayer thickness (from 0 ML to 5 ML). Table 5.1 shows that when the thickness of the Cr interlayer is from 0 ML to 5 ML, there is a sharp decreased drop, but when the Cr interlayer reaches 20 ML, the value of the saturation field shows a tiny change. This result indicates that when the thickness of Cr interlayer reaches 5 ML, the Cr interlayer is from an island film to a continue film, and fully blocks UMA above 5 ML.

Table 5.1 The saturation fields of the Cr interlayers at different thickness for 10 ML Fe single crystalline film and GaAs (100) substrate.

Sample	Saturation field (Oe)
Cr(3nm)/Fe(10ML)/GaAs (100)	1799.295± 20.586
Cr(3nm)/Fe(10ML)/Cr(0.5ML)/GaAs (100)	1326.698± 13.274
Cr(3nm)/Fe(10ML)/Cr(1ML)/GaAs (100)	1022.284± 11.231
Cr(3nm)/Fe(10ML)/Cr(2ML)/GaAs (100)	910.212± 14.057
Cr (3nm)/Fe(10ML)/Cr(3ML)/GaAs (100)	599.732 ± 10.873

Cr(3nm)/Fe(10ML)/Cr(5ML)/GaAs (100)	56.804± 3.792
Cr(3nm)/Fe(10ML)/Cr(15ML)/GaAs (100)	59.901 ± 3.572
Cr(3nm)/Fe(10ML)/Cr(20ML)/GaAs (100)	52.352± 3.281

The 10ML Fe films grown on the different thicknesses of Cr interlayer, shows the existence of uniaxial magnetic anisotropy. Figure 1, especially when the Cr is 0 ML, clearly shows that UMA is large from the [011] direction (hard axis). From the 0.5 ML Cr interlayer to 5 ML, UMA decreased quickly, and when it reached 5ML UMA almost disappeared entirely (there is no clear difference between the easy and hard axis). This shows that the increased Cr interlayer has a huge influence on UMA. Comparing the 5 ML and 0 ML hard axis loop, it can be seen that while the loop displays no difference, the saturation field shows a slight change. This result indicates that when the Cr interlayer reaches 5 ML, it fully blocks UMA, although when the thickness of the Cr interlayer is increased to 20 ML, it does not change significantly.

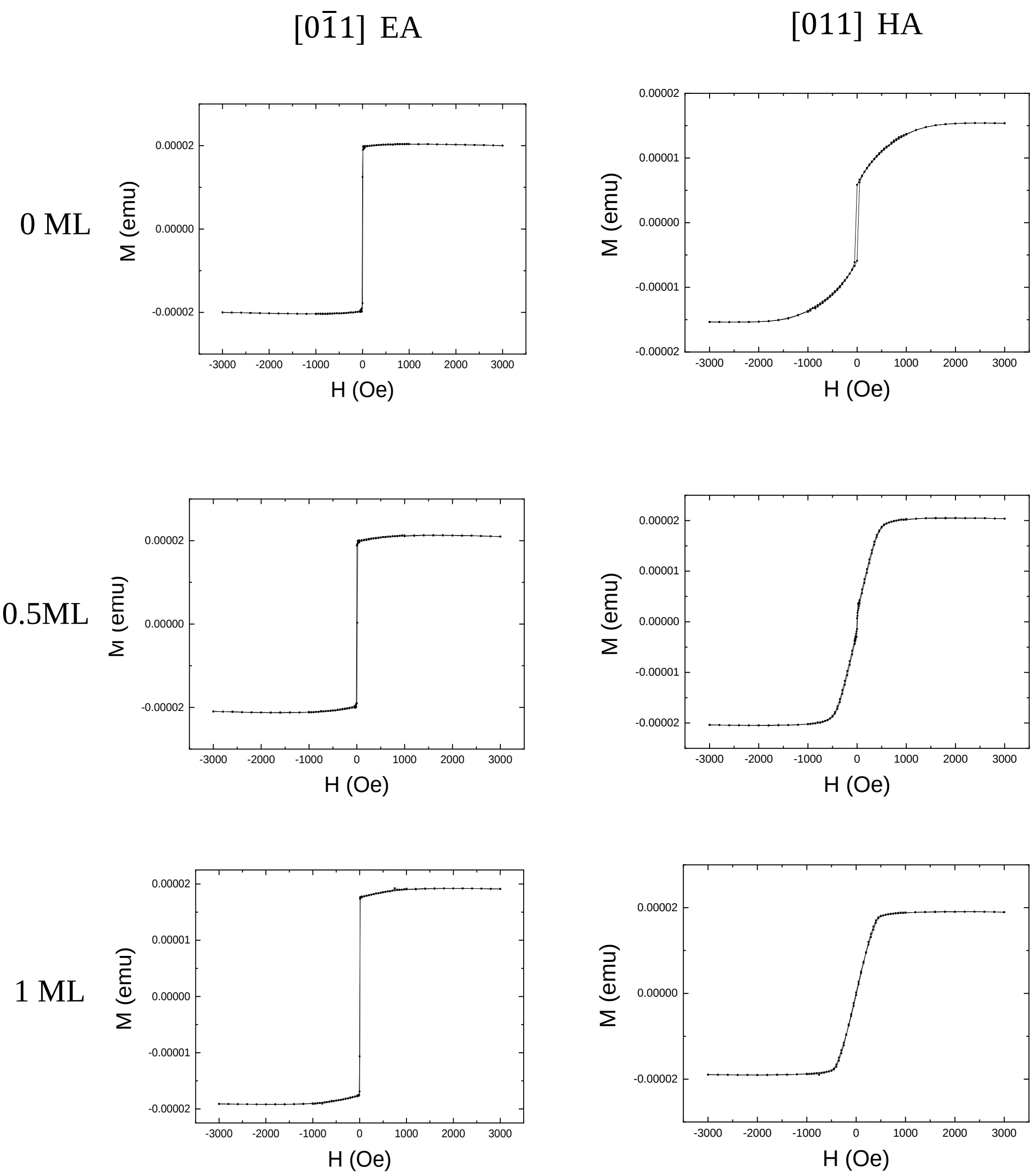
[0$\bar{1}$1] EA
[011] HA
0 ML
0.5ML
1 ML
M (emu)
H (Oe)
0.00002
0.00001
0.00000
-0.00001
-0.00002
-3000
-2000
-1000
0
1000
2000
3000

2 ML

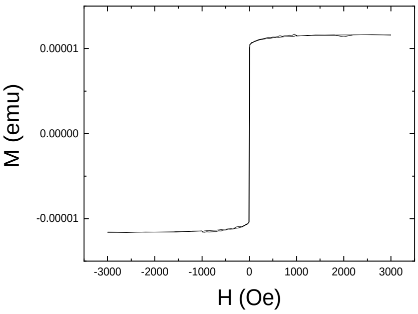

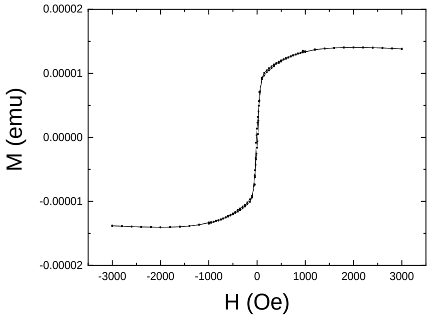

3 ML

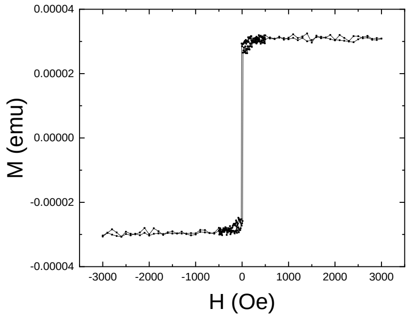

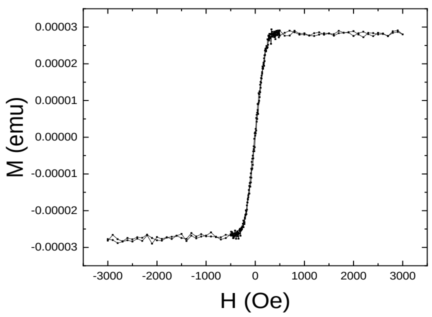

5 ML

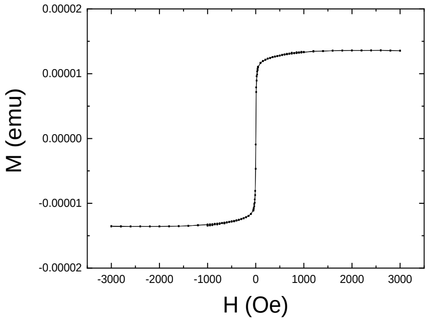

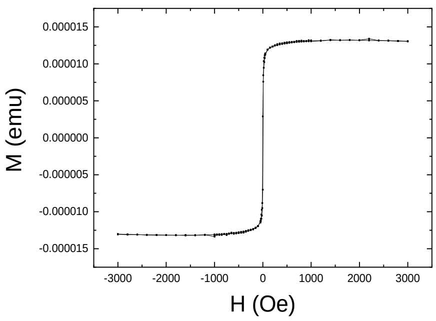

15 ML

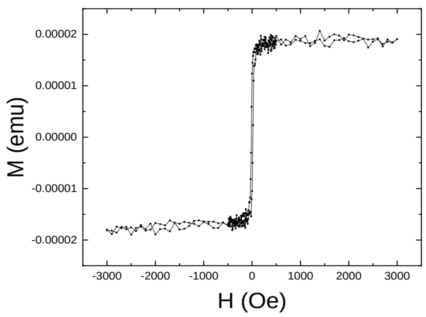

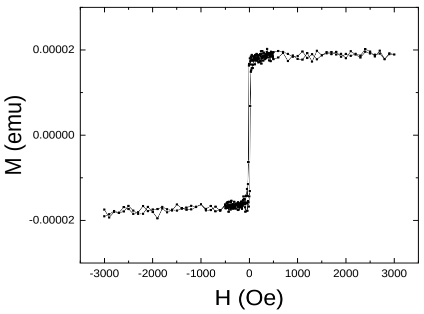

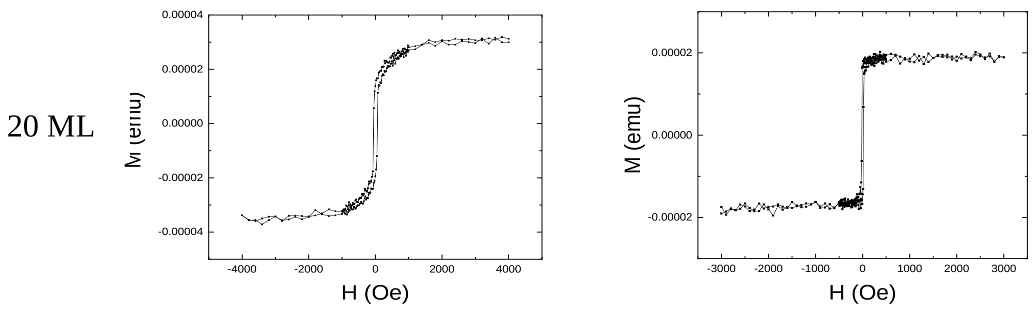

Figure 5.4 SQUID-VSM hysteresis loops from Cr(3nm)/Fe(10ML)/Cr(0-20ML)/GaAs (100) samples. These loops are all measured at room temperature with the 4000 Oe magnetic field applied along [011] and $[0\bar{1}1]$ (the hard axis and easy axis respectively).

Figure 5.4 shows the in-plane magnetic hysteresis (M-H) loops measured by SQUID-VSM along the EA and HA for Cr(3nm)/Fe(10ML)/Cr (different thickness)/GaAs (100) sample. The figure shows a clear UMA with a well-defined EA and HA axis. According to the 15 ML of Cr interlayer thickness from the VSM data, there is a 45-degree rotation from the bulk anisotropy, but the reason for rotation is not clear now. The value of the UMA field (H_k) can be obtained from the saturation field along the HA direction. Furthermore, the effective uniaxial anisotropy constant K_u^{eff} can be calculated using equation 4.1, which is described in chapter 4.

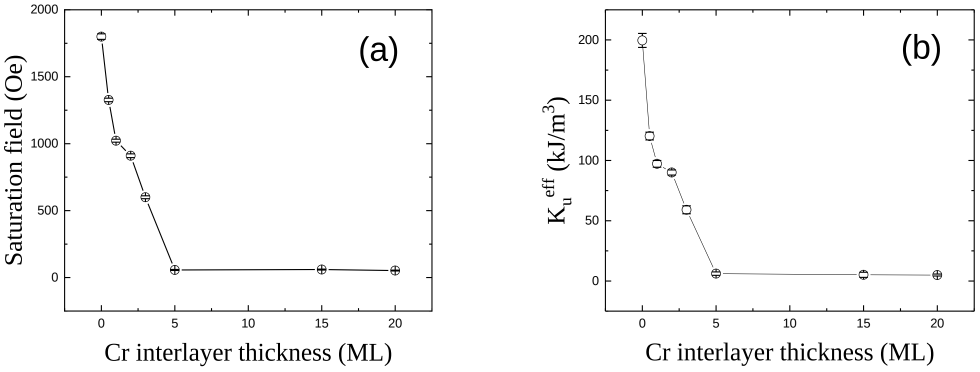

Figure 5.5 (a) indicates the saturation field from HA (hard axis) for 10 ML Fe film deposited on different thickness Cr interlayers. Figure (b) shows the tendency of the effective uniaxial anisotropy constant.

Figure 5.5 (a) and (b) show that the trend of H_k and K_u^{eff} is almost identical as expected. When the Cr interlayer became thicker, the values of H_k and K_u^{eff} dropped almost until 5 ML, but from 5 ML to 20 ML, the values only decreased slightly. This means that the 5 ML Cr interlayer represents the end of the decreased trend, and that after 5 ML it does not drop too much. In previous research, Xu et al[33] showed a transition from a superparamagnetic to ferromagnetic phase at around 4.8 ML Fe, at which point the structure begins to change from a large island into a continuous film. The lattice constant of 2.87Å for Fe is almost exactly half of GaAs (5.65 Å). Since Cr (2.884 Å) and Fe have the similar lattice constant[45], 5 ML Cr might be the point where Cr becomes a single crystalline film, and that after 5 ML the substrate is fully occupied with Cr. This is a reasonable explanation why the Cr interlayer from 5 ML to 20 ML did not change significantly, and why from 0 ML to 5 ML it dropped sharply.

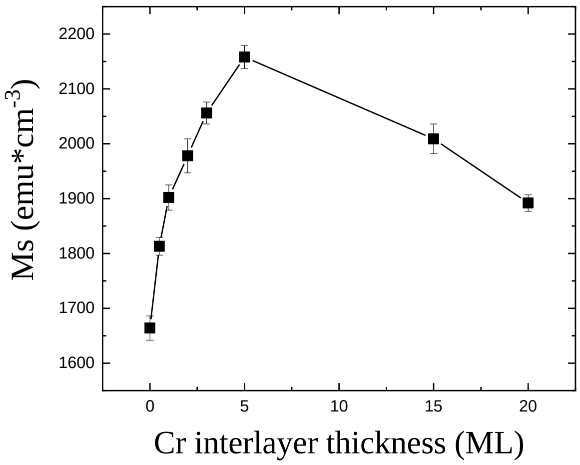

Figure 5.6 The value of M_s from 0ML Cr interlayer to 20ML. These data are calculated from the value of the saturated magnetic moment and the volume of samples.

The saturation magnetisation M_s can by calculated using equation 4.2, which was described in chapter 4. From Figure 5.6, especially when the thickness of Cr is 0 ML, the value of M_s is 1664.32 emu/cm^3, a value which matches the previous results of other researches[136, 159]. From 0 ML to 5 ML, with the increase of Cr interlayer thickness, the value of M_s rose to 2158.78 emu/cm^3, almost a 50% improvement. However, from 5 ML to 20 ML, the value of M_s decreased slightly. The 15 ML and 20 ML Cr films are the bulk films, and compared to single crystalline Cr films, the spin moment of Cr increased from -1.32u_B (single crystalline Cr) to -0.49u_B (bulk Cr)[160]. This is why the m_{spin}, m_{total} of Fe and saturation magnetisation decreased after 5ML. Detailed information pertaining to this will be discussed in section 5.2.

5.1.5 XMCD Measurement and Analysis

X-ray absorption spectroscopy (XAS) and XMCD experiments at the Fe $L_{2,3}$ absorption edges were performed at beamline I06 of the UK National Synchrotron Radiation Laboratory. The XAS experiments were carried out at 300K under an applied field ranging at 1T, with total electron yield (TEY) detection. Circularly polarised X-rays with a 100% degree of polarisation were used in normal incidence with respect to the sample plane, and a 60-degree angle along the perpendicular direction[161].

XAS and XMCD spectra of Fe L_2 and L_3 edges for 10 ML Fe film with different thicknesses of the Cr interlayer on GaAs (100) are shown in Figure 5.7 from (a) to (i). For XAS, u_+ and u_- are the absorption coefficients under antiparallel and parallel magnetic fields to the photon incident direction. For XMCD, the value of $u_+ - u_-$ and the integrated value of $u_+ - u_-$ are shown; these data are used for calculating XMCD sum rules. According to XMCD sum rules, the orbital (m_{orb}) and spin (m_{spin}) magnetic moments as well as the ratio (m_{ratio}) of m_{orb} to m_{spin} can be determined from XAS and XMCD spectra using equations 3.1 to 3.7, which were described in chapter 3. Because these films are all single crystalline films, according to Chen *et al*[91, 116], the value of n_{3d} for Fe of 6.61 to calculate all results has been used.

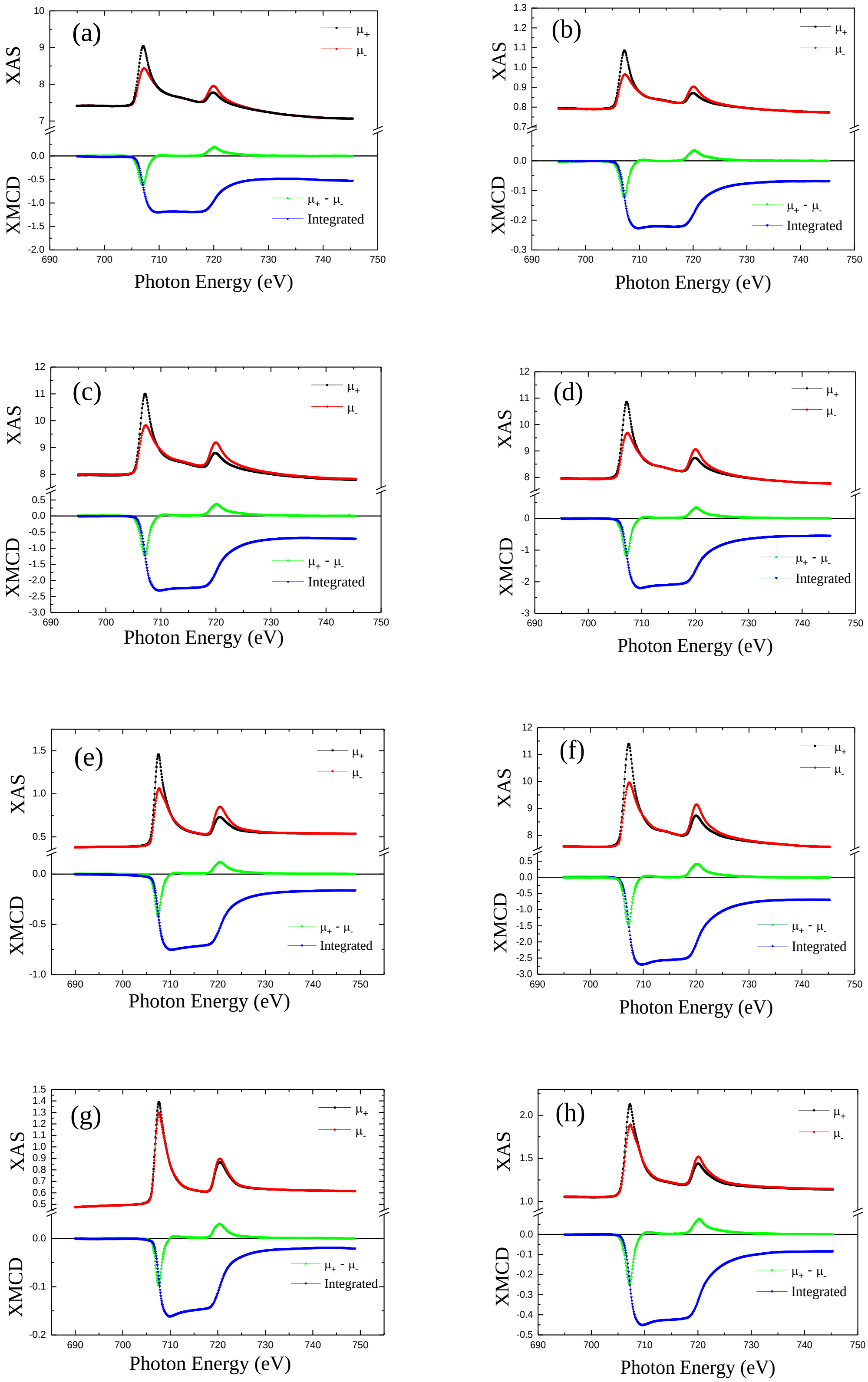

Figure 5.7 XAS and XMCD spectra of Fe atoms at L_2 and L_3 edges in Cr(3nm)/Fe(10ML)/Cr/GaAs (100) from (a) to (h): (a), (b), (c) are the thickness of Cr interlayer for 0ML, 0.5 ML and 1 ML films

respectively. (d), (e), (f), (g), (h) are the thickness of Cr interlayer for 2 ML, 3 ML, 5 ML, 15 ML and 20 ML films.

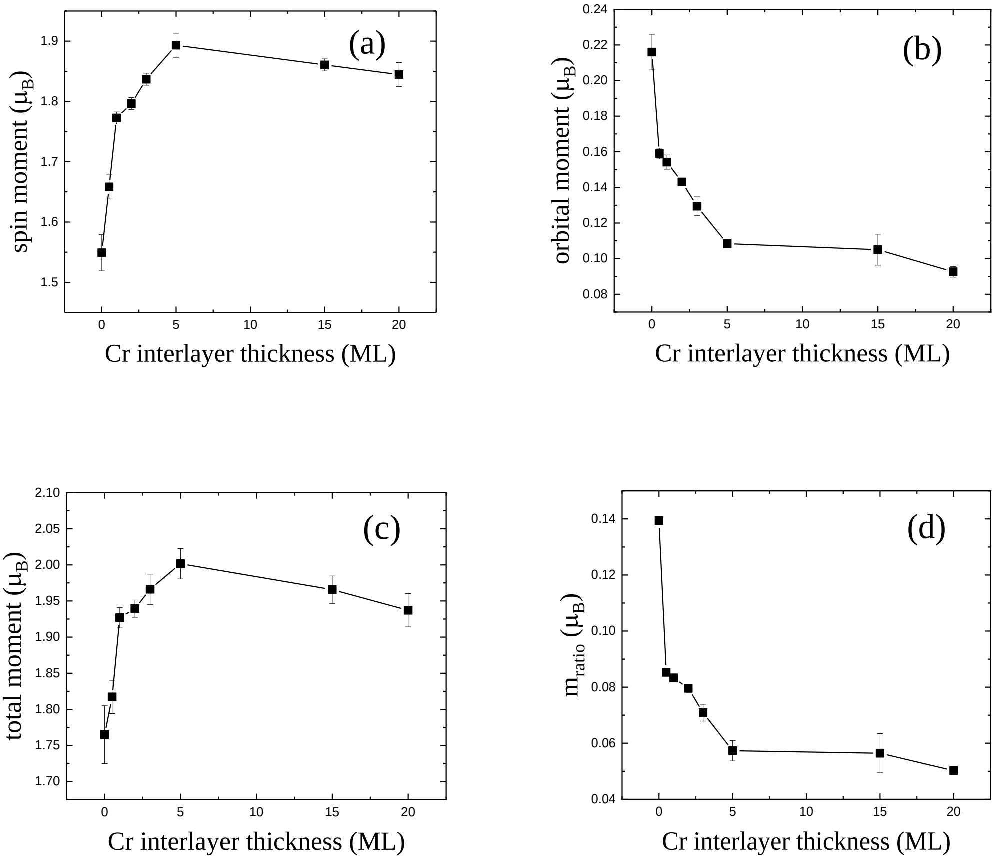

Figure 5.8 (a) and (b) show the spin moment and orbital moment of Fe atoms with different Cr interlayer thickness respectively. (c) and (d) present data about the total moment and orbital to spin ratio respectively.

Figure 5.8 clearly shows that (a) and (c) follow the same trend, and that (b) and (d) have a similar tendency. Since the total moment is equal to the orbital moment plus the spin moment, the values of spin moment are clearly much larger than the orbital moment, meaning that the trend of the total moment should follow the spin moment. M_s is the saturated magnetic moment which has a close connection with the total moment, meaning that the trend of M_s should be similar to the total moment. When comparing Figure 5.6 and Figure 5.8 (c), these two figures show a similar tendency, suggesting that all the experimental results are right and reasonable.

One interesting point to note is that when the interlayer Cr was 0ML, the value of 10 ML Fe of spin moment was smaller than the regular value (1.98μ_B). In comparison with previous results (Cr capping layer on Fe/GaAs), this value is similar, and symmetry breaking makes the contribution inside. To be more specific, magnetic films that are in contact with an antiferromagnetic layer capping layer often show large two-magnon scattering because of spatially inhomogeneous exchange bias[162-165]. In the case of the 3nm Cr capping layer on 10 ML Fe film, these defects are caused by step induced magnetic frustration between the magnetic moment of Fe and the spin density waves in Cr film[28, 162]. This effect will decrease the spin moment with only a 3nm Cr capping layer, but when the Cr interlayer is from 0 ML to 5 ML, this symmetry breaking is repaired. At this point the Fe spin moment values were enhanced. Finally, when the Cr was a continuous film (5 ML), the symmetry breaking was fully repaired, resulting in the 10 ML Fe spin moment values (1.893μ_B) being restored to their regular value. The spin moment value of 10 ML Fe with a 20 ML Cr interlayer does not change to much, and is also very close to the regular 10 ML Fe spin moment value.

Concerning (b) and (d), Figure 5.8(b) is the orbital moment while Figure 5.8(d) is the orbital to spin ratio. Many previous researches presented the results that the orbital moment is the key point which influences UMA, and that the orbital to spin ratio (spin-orbital coupling) has a relationship with interface interaction. Out results seem to fully match these data. Compared with UMA and orbital moment (Figure 5.5(a) and Figure 5.8(b) respectively), a similar trend can be identified: when the Cr interlayer was 0 ML, they all had the highest value, and when the Cr interlayer is increased, there was a similar decreased tendency, and when the Cr interlayer reached 20 ML, they were all at their lowest point. This reflects the fact that the orbital moment dropped when increasing the Cr interlayer, and that UMA and orbital moment were all blocked by the 5 ML Cr interlayer. Figure 5.8 shows the decreased trend of orbital to spin ratio, which indicates that the interface interaction effect is also weakened by increasing the Cr interlayer. The Cr interlayer impairs UMA and the interface interaction by the Cr area on GaAs (100) substrate when Cr reaches 5 ML. At this point, this layer cut all connections between the substrate and Fe, meaning that Fe and As atoms cannot have any chemical bonding, which is the reason why UMA disappeared.

Table 5.2 Orbital moment, spin moment, total moment and orbital to spin ratio of Fe atom from various Fe single crystalline samples in units of u_B/atom.

Sample	$m_{orb}(u_{\mathrm{B}})$	$m_{spin}(u_{\mathrm{B}})$	$m_{total}(u_{\mathrm{B}})$	m_{ratio}
Cr(3nm)/Fe(10ML)/GaAs (100)	0.216±0.010	1.549 ±0.03	1.765±0.04	0.140
Cr(3nm)/Fe(10ML)/Cr(0.5 ML)/GaAs (100)	0.159±0.003	1.658±0.02	1.817±0.02	0.085
Cr(3nm)/Fe(10ML)/Cr(1ML)/GaAs (100)	0.154±0.004	1.773±0.01	1.927±0.01	0.083
Cr(3nm)/Fe(10ML)/Cr(2ML)/GaAs (100)	0.143±0.002	1.796±0.01	1.940±0.01	0.080
Cr(3nm)/Fe(10ML)/Cr(3ML)/GaAs (100)	0.129±0.005	1.837±0.01	1.966+0.02	0.070
Cr(3nm)/Fe(10ML)/Cr(5ML)/GaAs (100)	0.108±0.001	1.893±0.02	2.001±0.02	0.057
Cr(3nm)/Fe(10ML)/Cr(15 ML)/GaAs (100)	0.105±0.009	1.861±0.01	1.966±0.02	0.056
Cr(3nm)/Fe(10ML)/Cr(20 ML)/GaAs (100)	0.093±0.003	1.845±0.02	1.937±0.02	0.050
Au(20ML)/Fe(8ML)/GaAs (100)[112]	0.26±0.030	2.03±0.14	2.29±0.17	0.128
Cr(15ML)/Fe(7ML)/GaAs (100)[32]	0.184±0.025	1.43±0.18	1.614±0.21	0.129
Bulk bcc Fe[91]	0.085	1.98	2.065	0.043

The values of the spin and orbital moments are found using the sum rule analysis whilst those of the other research values are described in Table II. It is well known that the orbital angular moment plays a dominant role in determining the uniaxial magnetic anisotropy[109]. It can be seen from orbital moment that the Fe single crystalline samples without Cr interlayer were all significantly enhanced compared to the Fe with Cr interlayer, but compared to the Fe single crystalline film and Fe bulk film, it is shown that the Fe bulk film dramatically decreased, a result confirming previous researches.

The situation of spin to orbital ratio is similar to the orbital moment. The values of spin to orbital ratio on the three samples Cr(3nm)/Fe(10ML)/GaAs (100), Au(20ML)/Fe(8ML)/GaAs (100) and Cr(15ML)/Fe(7ML)/GaAs (100) are all around 0.13μ_B, and larger than bulk Fe film and 10 ML Fe with Cr interlayer. The spin moment indicates that the Cr as a capping layer can decrease the spin moment, as noted previously. When the Cr interlayer rose from 0 ML to 5 ML, the spin moments were significantly enhanced. Up until 5 ML, symmetry breaking was fully repaired, so that the value of the spin moment on 5 ML and 20 ML Cr interlayer samples recover and return to the regular 10 ML Fe spin moment value (around 1.98u_B).

5.1.6 TEM Measurement and Analysis

Structural properties of the grown films were studied using a JEOL 2200FS double aberration corrected (scanning) transmission electron microscope (S) TEM. Cross-sectional TEM specimens were prepared using conventional methods, including mechanical thinning and polishing, followed by Ar ion milling to achieve electron transparency.

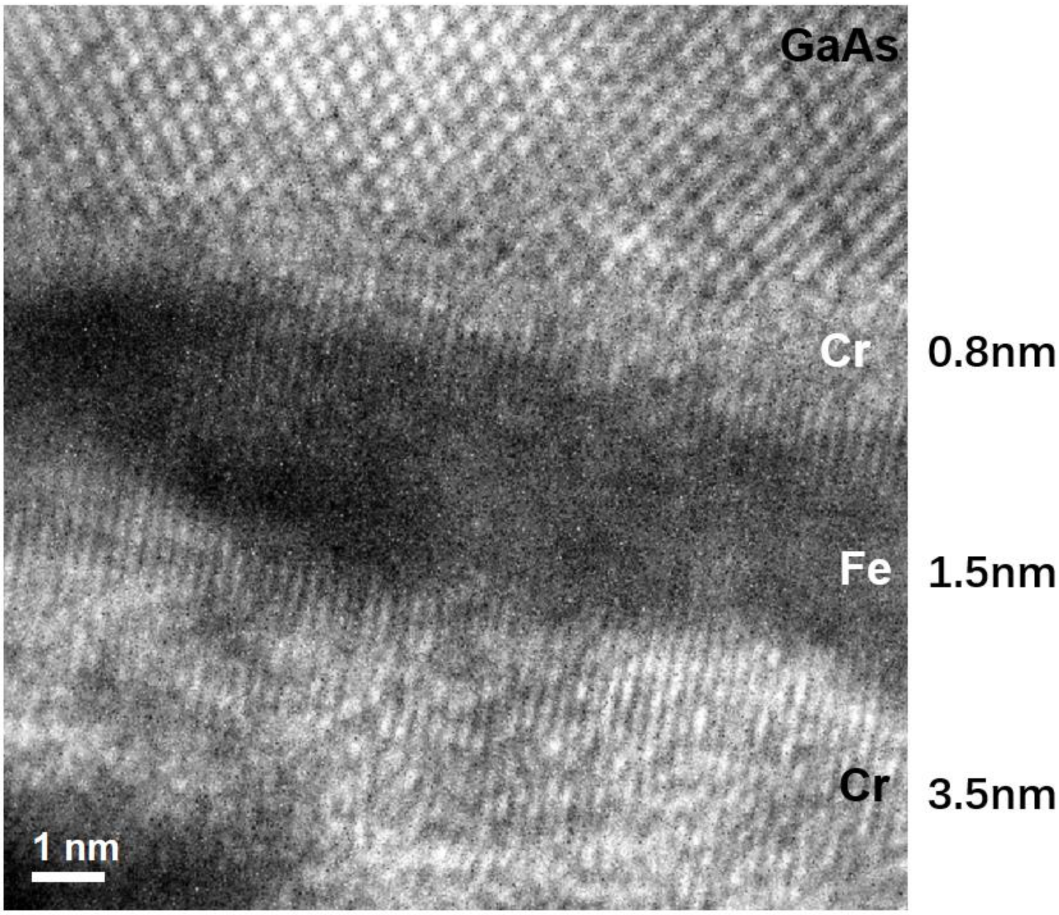

Figure 5.9 Cross-sectional bright-field scanning TEM of Cr(3nm)/Fe(10ML)/Cr(5ML)/GaAs (100) sample in [110] view.

A high-resolution cross-section TEM image of the structure is shown in figure 5.9. The film thickness, of 0.8 nm for Cr interlayer, 1.5 nm for Fe, matched with the growth settings. The 3.5 nm Cr capping layer is a little thicker than the set value, which because the oxidation of Cr capping layer. Due to the mass contrast, a clear distinction between GaAs and Cr can be observed, as well as between Fe and Cr interlayer or the Cr capping layer. This image evidenced the 5 ML Cr interlayer is the single crystal structure and the Cr interlayer formed the continuous film at 5 ML, and then the 10 ML Fe film remained the single crystal structure due to the lattice mismatch is very small between Fe and Cr atoms, which could support our conclusion.

5.1.7 Summary of Findings

Figure 5.10 shows the model of our conclusion. At the start, as shown in Figure 5.10(a), Fe film grows on the GaAs substrate, and it has Fe-As bonding and UMA, so the spin-orbital coupling from the interface is strong, and the orbital moment of Fe is as large as $0.22u_B$. As shown in Figure 5.10(b), in several island Cr interlayer films there is growth between the Fe layer and GaAs substrate. The island Cr interlayer films blocked Fe-As bonding, meaning that the orbital moments of Fe and the values of spin-orbital ratio and UMA were decreased. Finally, as can be seen in Figure 5.10(c), when the Cr interlayer reached 5 ML, the Cr interlayer formed a continuous film. This fully blocked UMA and completely cut Fe-As bonding, resulting in values of Fe orbital moments and spin-orbital ratio declining to their lowest value, before UMA disappeared completely.

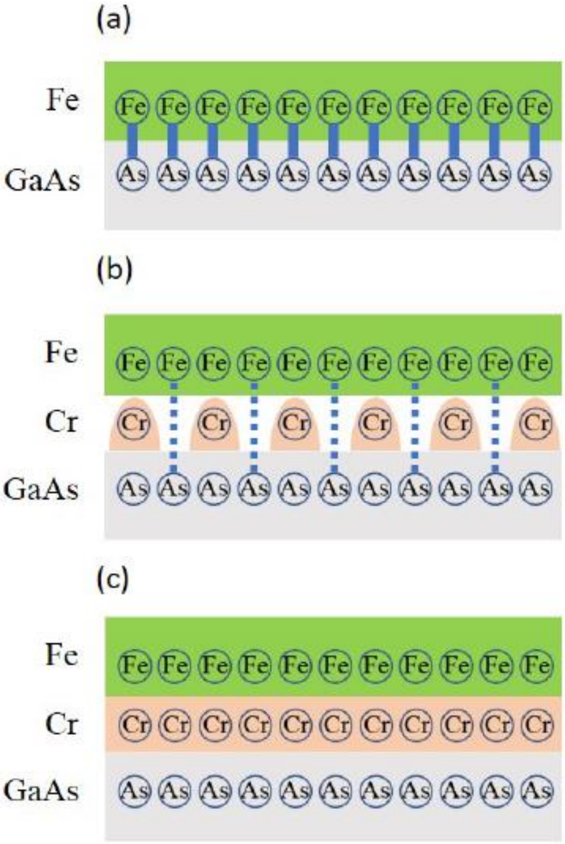

Figure 5.10 indicates the influence of the Cr interlayer between the Fe-As bonding.

In conclusion, we have investigated UMA and the element specific spin and orbital moments in the Fe-Cr-GaAs (100) system through magnetisation measurement, RHEED measurement, XMCD measurement and sum rule calculation. The result obtained through SQUID-VSM measurement confirmed that UMA was decreased by the increasing Cr interlayer. RHEED measurement reveals that when Cr reaches 5 ML on GaAs (100) substrate, it goes from being an island film to a continuous film, and shows the Cr single crystalline structure on the screen. XMCD measurements indicate two points: firstly, that 10 ML Fe with a Cr interlayer and Cr capping layer can adjust the spin moment of Fe, which is due to symmetry breaking; secondly, that UMA is correlated with orbital moment and spin to orbital ratio, which is due to the Cr interlayer having no relationship to the spin moment of Fe.

The origin of UMA is a controversial issue, as outlined in previous research. Our experiment shows that the notion of stress being induced by interface lattice mismatch can be ruled out because Cr has a similar lattice structure as Fe film, meaning that the stress induced cannot be a major factor influencing UMA. It therefore seems that the chemical bonding between As and Fe atoms is how UMA originates, when the Cr interlayer is between 0 ML and 5 ML and the area of Cr on GaAs substrate was increasing. This lead to UMA decreasing sharply, but at 5 ML Cr displayed a single crystalline structure and fully covered all areas on GaAs substrate. 5 ML Cr cut the bonding between As and Fe atoms, meaning that when Cr reached 5 ML, UMA disappeared. This indicates that the origin of UMA in the Fe-GaAs system is from chemical bonding: if the chemical bonding between Fe and GaAs is full cut, UMA would not exist.

These results are useful for understanding the fundamental magnetic properties in the Fe-GaAs system, which could be important for future researchers and applications of this structure in next generation spintronic devices like MRAM, where the detailed functions of data process and storage could be integrated in a single device.

5.2 Au/Fe/Cr/GaAs System

5.2.1 Introduction

For studying the films with Au as the capping layer, the magnetic property of Cr interlayer can be measured by XMCD measurement, the spin and orbital moment can be calculated by sum rule, thus UMA changed by the thickness of Cr interlayer can be observed deeply and directly, and it also can remove the influence from Cr capping layer.

X-ray magnetic circular dichroism (XMCD) combines the abilities of spectroscopy and magnetometry. The success of the XMCD technique is not only due the element specificity with sub-monolayer sensitivity, but also the development of the integral sum-rules[89, 166-170]. Many researches have focused on the ferromagnets like Fe, Co and Ni, but little work has been done on XMCD for the early *3d* transition metals (TMs)[171, 172] because of two major drawbacks: (1) These metals are either non-magnetic (Ti, V) or antiferromagnetic (Cr, Mn) in their bulk configuration, and thus reveal no XMCD signal; (2) For spin-polarized early TMs, the circular dichroism is much smaller compared to the ferromagnets Fe, Co and Ni. When demonstrating early *3d* TMs, it is difficult to extract the circular dichroism even without the attendant noise.

Over the last two decades, major studies for Fe/Cr structure have focused on the Fe/Cr alloy[173-175] or the Fe/Cr multilayers[176-181], while much less work has focused on Cr moments in Fe/Cr on the GaAs substrate, in particular on very thin Cr interlayer films. To determine the influence of UMA when using a very thin Cr interlayer, in this work different thicknesses of Cr film were inserted between GaAs substrate and 10ML Fe films. The Cr layer is an antiferromagnetic film, which would normally be used in the investigation of antiparallel coupling[155-157, 182]. Fe and Cr have a similar lattice constant, meaning that the Cr interlayer could make only a slight contribution to the formation of a strain induced UMA. However, no UMA was observed. Subsequently, we undertook room temperature XMCD, RHEED and SQUID-VSM investigations into the properties of ultrathin films grown on substrate with various Cr interlayer. From our studies, we were able to confirm the results from section 5.1. When the thickness of Cr reached 5 ML, the Fe-As bonding was fully blocked, so UMA disappeared; in addition, the Cr orbital moment decreased significantly from 0.5 ML to 5 ML, although above 5 ML the values of the Cr orbital moment were similar to the Fe/Cr multilayer. Secondly, there are two different valence states for both Fe and Cr atoms, which exist in the Fe-Cr-As compound layer (the thickness of Cr is under 0.5 ML), and slightly increase UMA. More importantly, the Cr atoms transferred from the antiferromagnetic property to the ferromagnetic property in the compound layer.

5.2.2 Sample Growth

The 10 ML Fe films with different thicknesses of Cr interlayer were grown on GaAs (100) substrates. Before deposition on the Cr interlayer, the substrate surface was etched and cleaned. The first step was to remove any contaminants on the substrate surface by using acetone, iso-propyl alcohol (IPA) and deionized water. The second step was to remove the oxide layer through the immersion of the substrate into an $H_2SO_4/H_2O_2/H_2O$ (4:1:1) solution for 45 seconds. Both steps were performed in a level 100 clean room so as to prevent any dust particles contamination. The third step was to create a flat surface for film deposition. The etched substrate was immediately transferred into an MBE chamber with a base pressure of 2.3×10^{-10} mbar. The substrate was then treated with ion-milling before annealing (low energy Argon ion beams were sputtered onto the substrate surface for 30 minutes and gently removed a thin layer of surface material, exposing the virgin layer of the substrate). The final step is annealing, where the substrate was required to be annealed at 480°C (at an annealing pressure lower than 8×10^{-9} mbar) for 60 minutes to further remove natural oxides and create the surface reconstruction[93]. The surface must cool to room temperature prior to film growth. The Cr interlayer and 10 ML Fe layers were grown using the two different source evaporators in the MBE system, where the pressure was lower than 2.1×10^{-9} mbar. Finally, a 3 nm Au capping layer was deposited to prevent the Fe film from oxidisation.

5.2.3 RHEED Patterns and Analysis

Since the substrates or samples remain in a UHV environment, the only way to examine the surface quality or morphology is to observe the RHEED (Reflection High Energy Electron Diffraction) patterns. The main advantages of RHEED patterns are that they are in-situ, fast, and surface-sensitive. Multiple RHEED patterns were recorded throughout the film deposition for monitoring purposes.

The GaAs (100) substrate were cleaned following the same processes. Figure 5.11 shows the RHEED images of the GaAs (100) substrates, various thicknesses of Cr interlayer and 10 ML Fe films. From the RHEED patterns of all 10 ML Fe films, one result which can be confirmed is that all the 10 ML Fe films have a single crystalline structure, and the different thickness of Cr have not changed the structure of 10 ML Fe films. The lattice constant of 2.87Å for Fe is almost exactly half of GaAs (5.65 Å). The lattice constant of Cr is 2.88 Å, which is almost no different to the Fe value, which means the lattice mismatch between Fe and Cr is very small. Even when the thickness of then Cr interlayer reaches 20 ML, 10 ML Fe remains a single crystalline structure, and the Cr interlayer does not make any contribution to the formation of Fe single crystalline structure[31, 158]. The RHEED patterns for various thickness of Cr interlayer are similar to those in section 5.1, meaning that our experiments are repeatable and that the MBE system is stable. From 0.1 ML to 1 ML, the Cr RHEED images show the single crystalline structure, but because the Cr interlayer in these thicknesses is an island film and covers only a small area of the GaAs substrate, the 0.1 ML to 1 ML Cr RHEED patterns actually indicate the structures from GaAs substrate. When the thickness reaches 2 ML, there is no signal from the RHEED screen. Finally, from 5 ML to 20 ML, the RHEED images indicate the single crystalline structure again, in particular when the Cr thickness was at 5 ML, when the RHEED pattern converted from no single to a single crystalline structure.

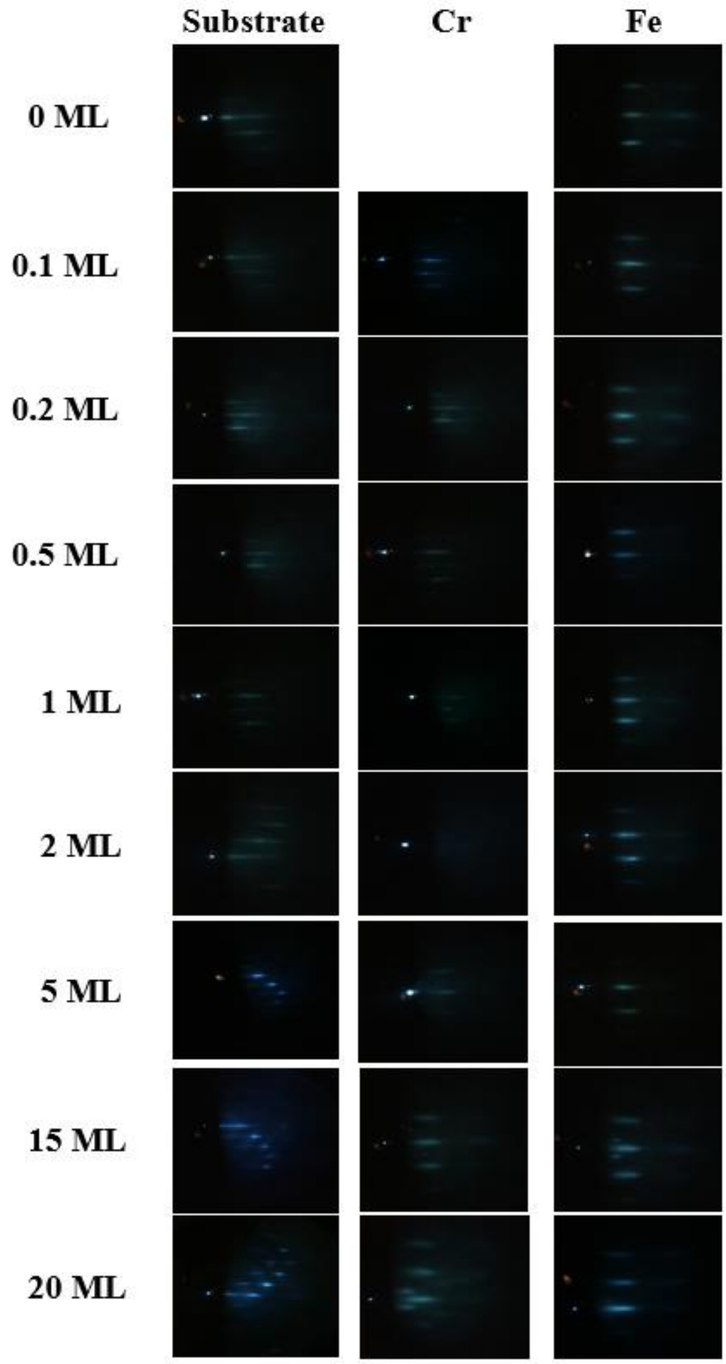

Figure 5.11 shows the RHEED patterns related to GaAs (100) substrates ($[0\bar{1}1]$ view and substrates are all 1×1 single crystalline structure), the various thickness Cr interlayers and 10 ML Fe films which grow on the Cr interlayer. The thickness of the Cr interlayer is from 0ML to 20ML, and the thickness of Fe remains at 10ML.

5.2.4 VSM Measurement and Analysis

The in-plane magnetic hysteresis loops of all the samples were measured on both the $[0\bar{1}1]$(easy axis) and [011] (hard axis) using a Vector Magnetometer Model 10 VSM and Vector measurement system at room temperature (300K), as shown in Figure 5.12. Since a strong uniaxial magnetic anisotropy field, potentially as large as 949.7 Oe, was expected in the Au(3nm)/Fe(10 ML)/GaAs (100) sample along hard axis, the VSM measurement was conducted using a maximum magnetic field of 3000 Oe so as to ensure all the samples were definitely saturated.

None of the easy axis hysteresis loops from Figure 5.12 change according to the different thicknesses of the Cr interlayer, so one result can be confirmed: the various thickness of the Cr interlayers does not influence the easy axis, and so all the easy axis loops have the similar coercivity and saturation fields around 50 Oe. This result also confirmed the previous researches in section 5.1.

The hysteresis loops along the hard axis are more interesting. The Cr interlayer from 0 ML to 0.2 ML, compared with the sample without a Cr layer, saw the magnetic saturation field along the hard axis enhance by 10% and 20% (at 0.1 ML and 0.2 ML Cr interlayer respectively). From 0.5 ML to 5 ML, the value of the saturation field decreased significantly, and uniaxial magnetic anisotropy disappeared at 5 ML. Finally, the hysteresis loops along the hard axis from the 15 ML and 20 ML Cr interlayer remain in the same saturation field (around 50 Oe) when the Cr interlayer is 5 ML: these films did not indicate uniaxial magnetic anisotropy. This result confirmed my previous results in section 5.1: the 5 ML Cr continuous interlayer fully blocked the uniaxial magnetic anisotropy, and cut the Fe-As bonding by the occupation area from the interface between the Fe film and GaAs substrate.

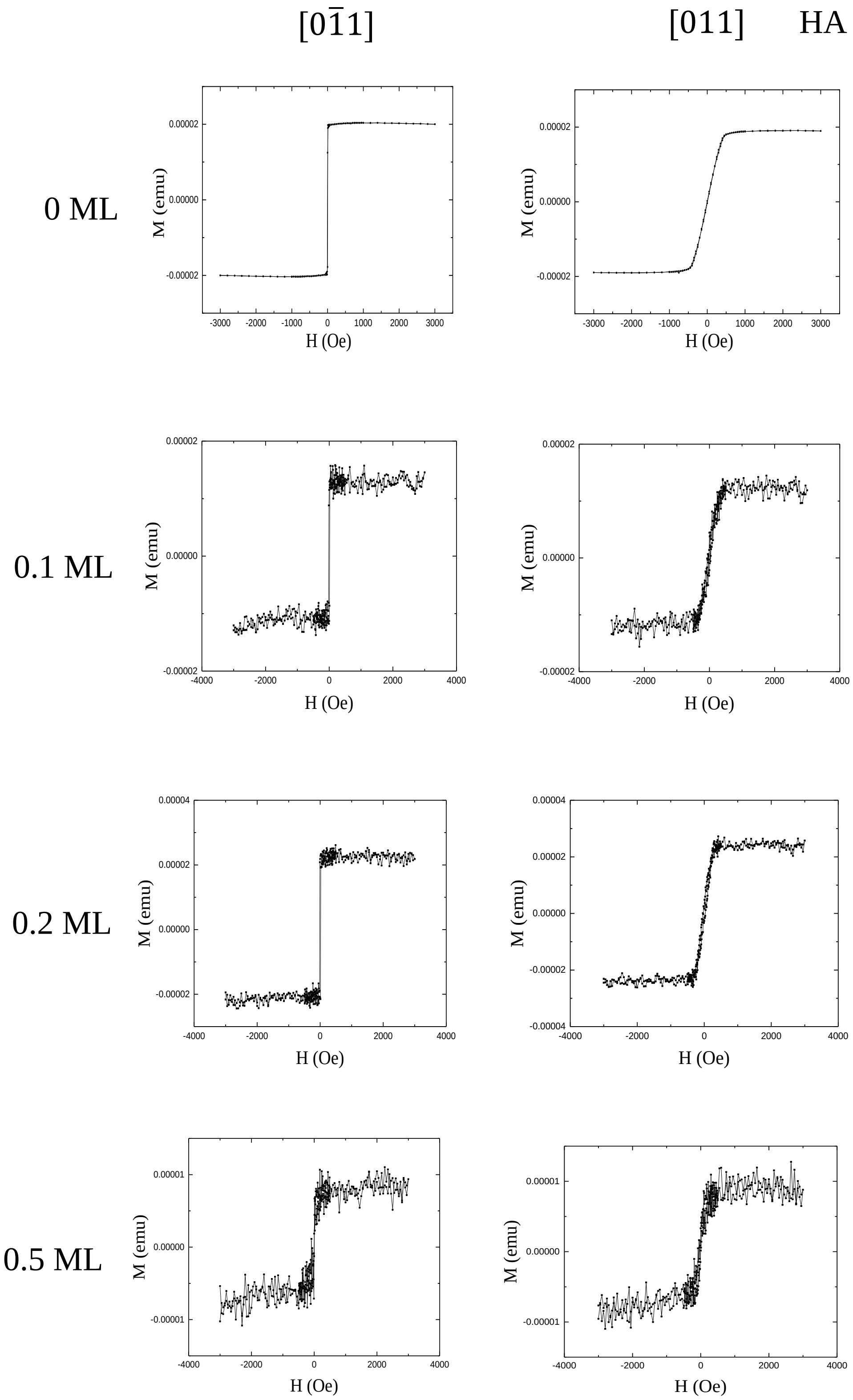
[0$\bar{1}$1]
[011]
HA
0 ML
0.1 ML
0.2 ML
0.5 ML
M (emu)
H (Oe)
0.00004
0.00002
0.00001
0.00000
-0.00001
-0.00002
-0.00004
-4000
-3000
-2000
-1000
0
1000
2000
3000
4000

1 ML

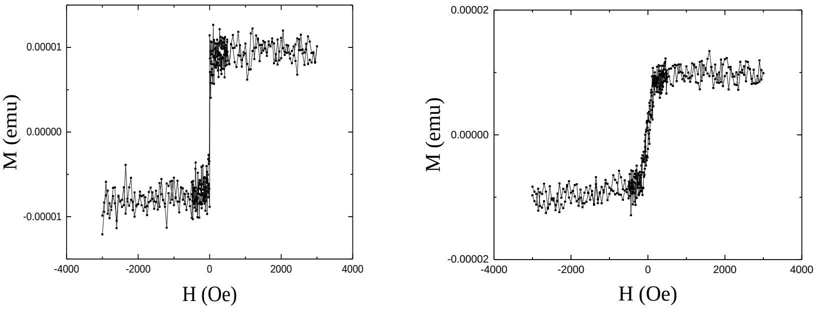

2 ML

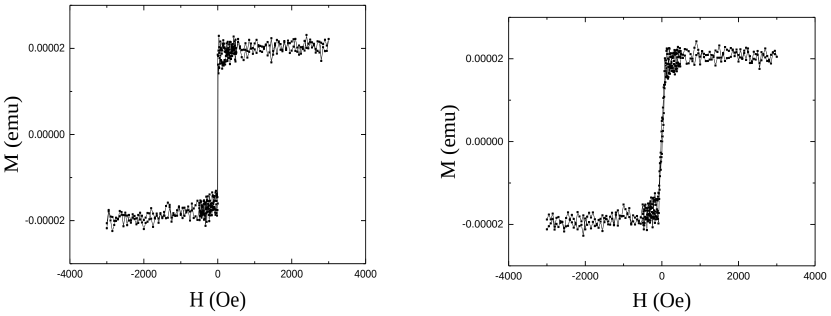

5 ML

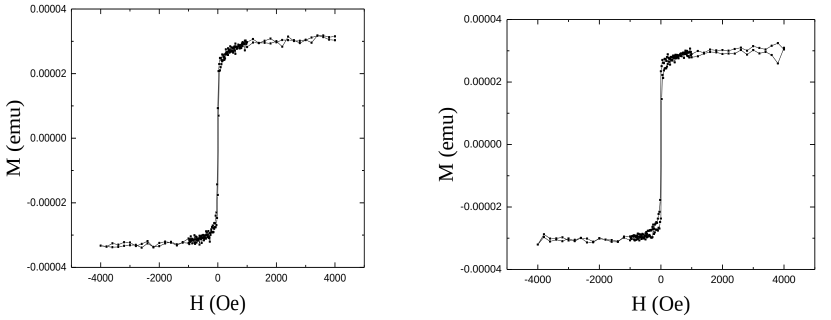

15 ML

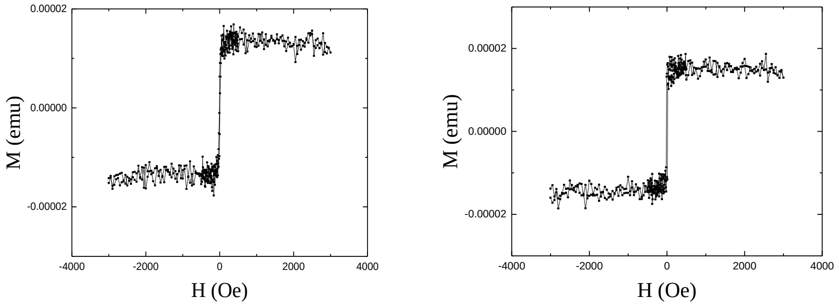

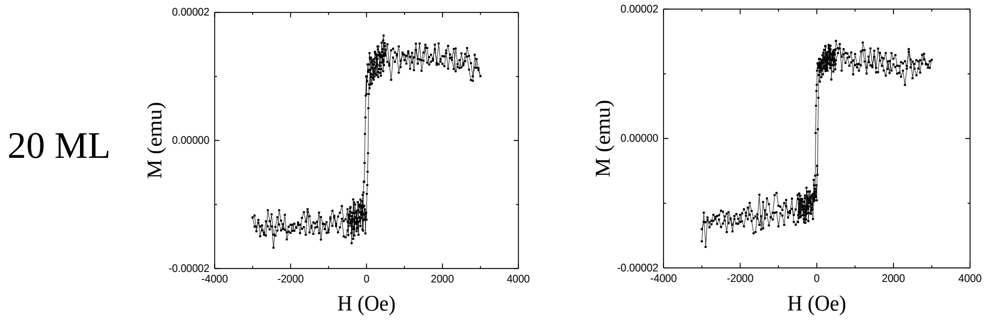

Figure 5.12 VSM hysteresis loops of various Cr interlayer thicknesses (from 0 to 20 ML) between GaAs (100) substrate and 10 ML Fe. These loops are all measured at room temperature with the 3000 Oe magnetic field applied along [011] and $[0\bar{1}1]$ (hard axis and easy axis respectively).

The value of the UMA field (H_K) can be obtained from the saturation field along the hard axis direction. Furthermore, the effective uniaxial anisotropy constant (K_u^{eff}) and the saturation magnetisation (M_s) can be calculated using equations 4.1 and 4.2, as described in chapter 4.

Table 5.3 presents detailed data about the values of the saturation field, the effective uniaxial anisotropy constant and saturation magnetisation. Since the values of the effective uniaxial anisotropy constant and saturation magnetisation are in direct proportion to the change in the saturation field, these two kinds of values have a similar tendency in terms of the value of the saturation field. In this case, it increased for the 0.1 ML and 0.2 ML Cr interlayers, and dropped for the 0.5 ML to 5 ML Cr interlayers, and for thicknesses for the 5 ML to 20 ML Cr interlayers, it had the similar value.

The tendency charts for the saturation field, effective uniaxial anisotropy constant and saturation magnetisation are shown in Figure 5.13 (a), (b) and (c) respectively. Compared with the previous results in section 5.1, the tendency charts for the saturation field and effective uniaxial anisotropy are very similar, whilst the values for saturation magnetisation are clearly different. From the last section, the values of saturation magnetisation are at their peak at 5 ML Cr interlayer, and then decrease from 5 ML to 20 ML. In this experiment, however, the values of saturation magnetisation increased from the 0 ML to 5 ML Cr interlayer, and then fluctuated around 1640 erg/cm^3 from the 5 ML to 20 ML Cr interlayer. In this part, Au was used for the capping layer as it has three main advantages: 1) The Au capping layer has a slight influence with spin and orbital moments, while the Cr capping layer or interlayer decreased the orbital and spin moments. 2) Using Au as a capping layer would rule out the effect of symmetry breaking between the two different thickness Cr layers. 3) The spin and orbital moments of the Cr interlayers can be obtained from XMCD without the Cr capping layer, which means the influence of the Cr interlayer can be intuitively shown from XMCD calculations. The saturation magnetisation has the correlation with the total moment, and the spin moment leads major role in the total moment, meaning that the saturation magnetisation is influenced by the spin moment. This detailed relationship will be discussed in the next section (XMCD analysis). The difference from the two tendency charts of saturation magnetisation is caused by symmetry breaking. In this project, the values of saturation magnetisation decreased at the beginning and then remained from 5 ML.

Table 5.3 The values of the saturation field, effective uniaxial anisotropy constant and saturation magnetisation for various thicknesses of Cr interlayers between 10 ML Fe single crystalline film and GaAs (100) substrate.

Sample	Saturation field (Oe)	$K_u^{eff} (kJ/m^3)$	M_S (emu/cm^3)
Au(3nm)/Fe(10ML)/GaAs (100)	949.7 ± 25.3	141.5 ± 5.4	1858.9 ± 25.3
Au(3nm)/Fe(10ML)/Cr(0.1ML)/GaAs (100)	1050.1 ± 23.1	158.8 ± 6.1	1859.7 ± 20.6
Au(3nm)/Fe(10ML)/Cr(0.2ML)/GaAs (100)	1150.2± 22.4	171.1 ± 4.6	1863.9 ± 20.9
Au(3nm)/Fe(10ML)/Cr(0.5ML)/GaAs (100)	749.9± 14.1	98.3 ± 4.9	1784.6 ± 24.6
Au(3nm)/Fe(10ML)/Cr(1ML)/GaAs (100)	550.2 ± 10.3	82.9 ± 5.2	1736.1 ± 23.3
Au(3nm)/Fe(10ML)/Cr(2ML)/GaAs (100)	340.1 ± 10.5	66.4 ± 5.6	1688.7 ± 21.5
Au(3nm)/Fe(10ML)/Cr(5ML)/GaAs (100)	55.5 ± 3.5	6.9 ± 2.1	1634.5 ± 26.6
Au(3nm)/Fe(10ML)/Cr(15ML)/GaAs (100)	50.9 ± 4.4	5.8 ± 2.5	1641.5 ± 20.3
Au(3nm)/Fe(10ML)/Cr(20ML)/GaAs (100)	49.9 ± 5.8	5.4 ± 2.3	1638.2 ± 20.1

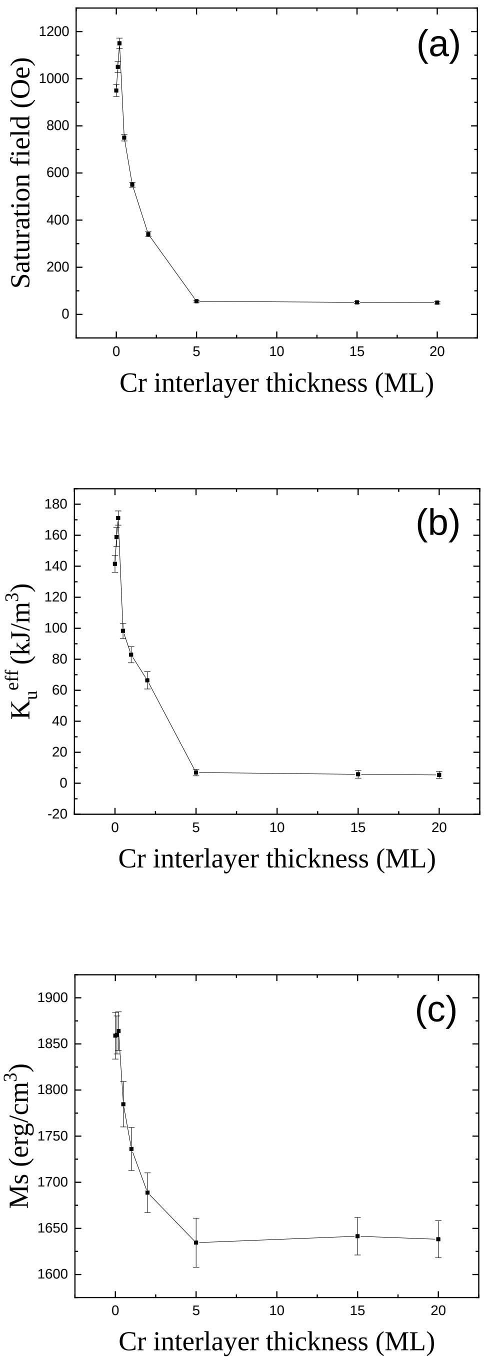

Figure 5.13 (a), (b)and (c) are the tendency charts for the saturation field, effective uniaxial anisotropy constant and saturation magnetisation respectively.

5.2.5 XMCD Measurement and Analysis

XMCD measurements were performed at normal incidence to the Au(3nm)/Fe(10 ML)/Cr/GaAs (100) samples in the I06 station of Diamond Light Source. The XMCD spectra were measured at both positive and negative applied fields for Fe and Cr elements. The data were collected by a Total Electron Yield (TEY) detector in the analysis chamber under a magnetic field of 1T. All the samples were measured with a 60-degree angle along the perpendicular direction.

The XAS and XMCD spectra of Fe L_2 and L_3 edges for 10 ML Fe films with various thicknesses of Cr interlayers on GaAs (100) substrate are shown in Figure 5.14 from (a) to (i). Figure 5.15 (a) to (h) indicate the XAS and XMCD spectra of Cr L_2 and L_3 edges for different thicknesses of Cr interlayers. In the XAS part, u_+ and u_- are the absorption coefficients under antiparallel and parallel magnetic fields to the photon incident direction. In the XMCD part, the value of $u_+ - u_-$ and the integrated value from $u_+ - u_-$ are shown; these data are used for calculating XMCD sum rules. According to the XMCD sum rules, the orbital (m_{orb}) and spin (m_{spin}) magnetic moments and the ratio (m_{ratio}) of m_{orb} to m_{spin} can be determined from XAS and XMCD spectra using equations 3.1 to 3.7, mentioned in chapter 3. According to Chen *et al* and Scgerz *et al*[91, 116, 183, 184], we have used the value of n_{3d} for Fe and Cr element of 6.61 and 5.45 respectively to calculate all the results.

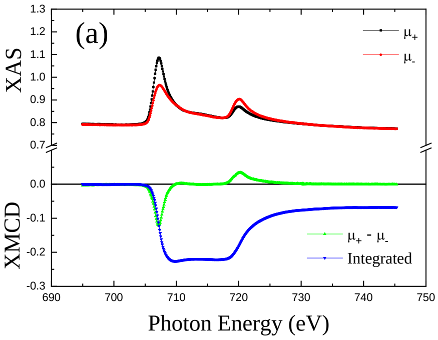
(a)
XAS
XMCD
μ_+
μ_-
$\mu_+ - \mu_-$
Integrated
1.3
1.2
1.1
1.0
0.9
0.8
0.7
0.0
-0.1
-0.2
-0.3
690
700
710
720
730
740
750
Photon Energy (eV)

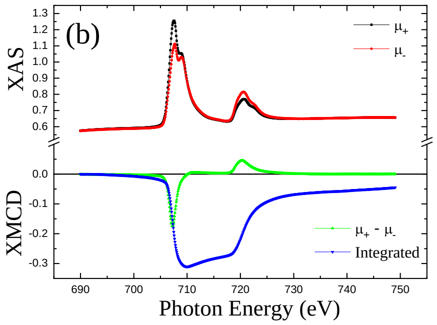
(b)
XAS
XMCD
μ_+
μ_-
$\mu_+ - \mu_-$
Integrated
1.3
1.2
1.1
1.0
0.9
0.8
0.7
0.6
0.0
-0.1
-0.2
-0.3
690
700
710
720
730
740
750
Photon Energy (eV)

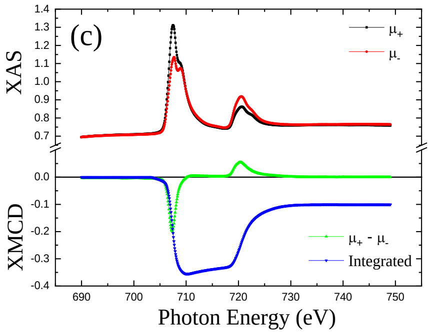
(c)
XAS
XMCD
μ_+
μ_-
$\mu_+ - \mu_-$
Integrated
1.4
1.3
1.2
1.1
1.0
0.9
0.8
0.7
0.0
-0.1
-0.2
-0.3
-0.4
690
700
710
720
730
740
750
Photon Energy (eV)

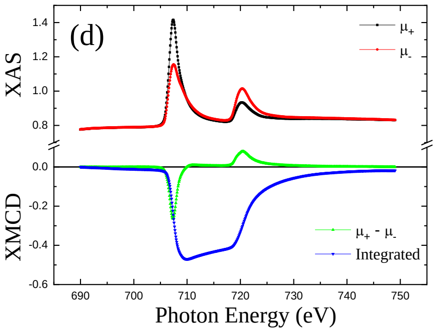
(d)
XAS
XMCD
μ_+
μ_-
$\mu_+ - \mu_-$
Integrated
1.4
1.2
1.0
0.8
0.0
-0.2
-0.4
-0.6
690
700
710
720
730
740
750
Photon Energy (eV)

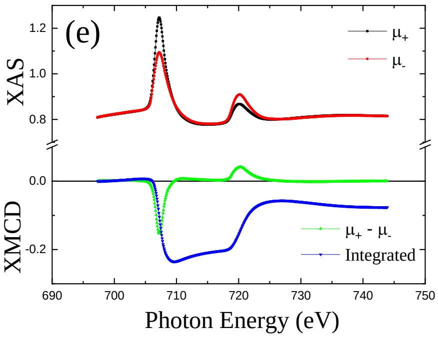
(e)
XAS
XMCD
μ_+
μ_-
$\mu_+ - \mu_-$
Integrated
1.2
1.0
0.8
0.0
-0.2
690
700
710
720
730
740
750
Photon Energy (eV)

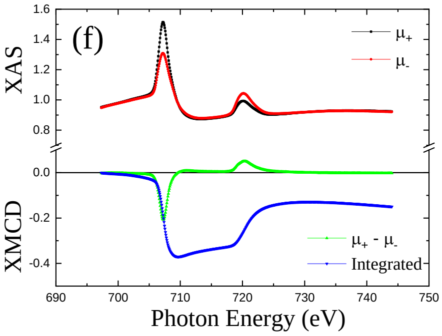
(f)
XAS
XMCD
μ_+
μ_-
$\mu_+ - \mu_-$
Integrated
1.6
1.4
1.2
1.0
0.8
0.0
-0.2
-0.4
690
700
710
720
730
740
750
Photon Energy (eV)

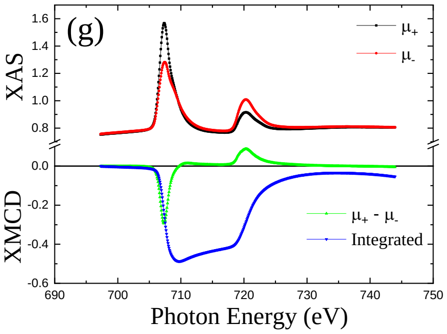
(g)
XAS
XMCD
μ_+
μ_-
$\mu_+ - \mu_-$
Integrated
1.6
1.4
1.2
1.0
0.8
0.0
-0.2
-0.4
-0.6
690
700
710
720
730
740
750
Photon Energy (eV)

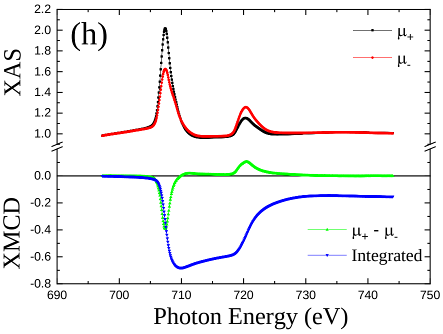
(h)
XAS
XMCD
μ_+
μ_-
$\mu_+ - \mu_-$
Integrated
2.2
2.0
1.8
1.6
1.4
1.2
1.0
0.0
-0.2
-0.4
-0.6
-0.8
690
700
710
720
730
740
750
Photon Energy (eV)

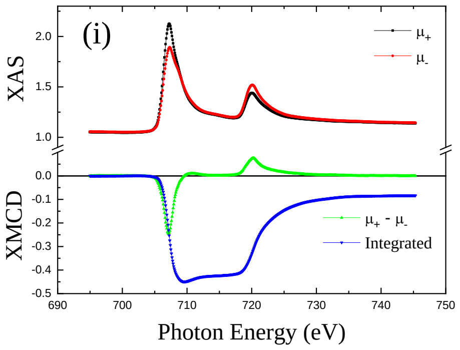

Figure 5.14 XAS and XMCD spectra of Fe atoms at L_2 and L_3 edges in Au(3nm)/Fe(10ML)/Cr/GaAs (100) from (a) to (i): (a), (b), (c) are the thickness of Cr interlayer for 0ML, 0.1 ML and 0.2 ML films respectively. (d), (e), (f), (g), (h) and (i) are the thickness of Cr interlayer for 0.5 ML, 1 ML, 2 ML, 5ML, 15 ML and 20 ML films respectively.

Figure 5.14 clearly shows that (b) and (c) have two different peaks on both the L_3 and L_2 edges of Fe atoms, while the other figures have one peak on the L_3 and L_2 edges around 707 eV and 720 eV. Figure 5.14 (b) and (c) are the 0.1 ML and 0.2 ML thickness of Cr interlayers, and the enhancements of the saturation field for 0.1 and 0.2 ML Cr interlayers were obtained from VSM analysis results. There are two peaks in Figure (b) and (c), the major peak on the L_3 edge (the higher one) is similar to others around 707 eV, but the secondary peak on L_3 (the lower one) is at 709 eV, according to the XAS figures. The two different peaks on the L_3 and L_2 edges refer to the two different valence states for Fe atoms. From previous research on Fe oxidisation XMCD, the reason for different valence states caused by the oxidation for Fe atoms can be ruled out[108, 185-189].

There are three important differences between this project and the iron oxidisation films: 1) In this project, we used the MBE system to grow all layers, and when the different layers grow, the pressure of the MBE system was always under 5.1×10^{-9} mbar during growth, which is impossible for the samples' oxidation. 2) The Fe oxidisation films should not have their edge jump from the secondary peak in XAS figures, while in my project, there are obvious edge jumps on the secondary peak of the L_3 edge, as shown in Figure 5.14 (b) and (c) in XAS images. 3) The values of orbital moment from Fe oxidisation films are almost double my orbital moment values in this project. This means that a kind of chemical compound layer is formed when the thickness of Cr interlayer is around 0.1 and 0.2 ML, and this chemical compound layer induced a kind of valence state for Fe atoms. Compared with Figure 5.14 (b) and (c), the edge jump in the XAS image from 0.2 ML Cr interlayer film is larger than the edge jump from 0.1 ML on both the L_3 and L_2 edges. This refers to the fact that the 0.2 ML Cr interlayer made a greater contribution on the interface than the 0.1 ML Cr interlayer. We suggest the chemical compound layer is slightly enhanced UMA, and this layer is formed from the 0.1 ML Cr interlayer and disappeared at the 0.5 ML Cr interlayer.

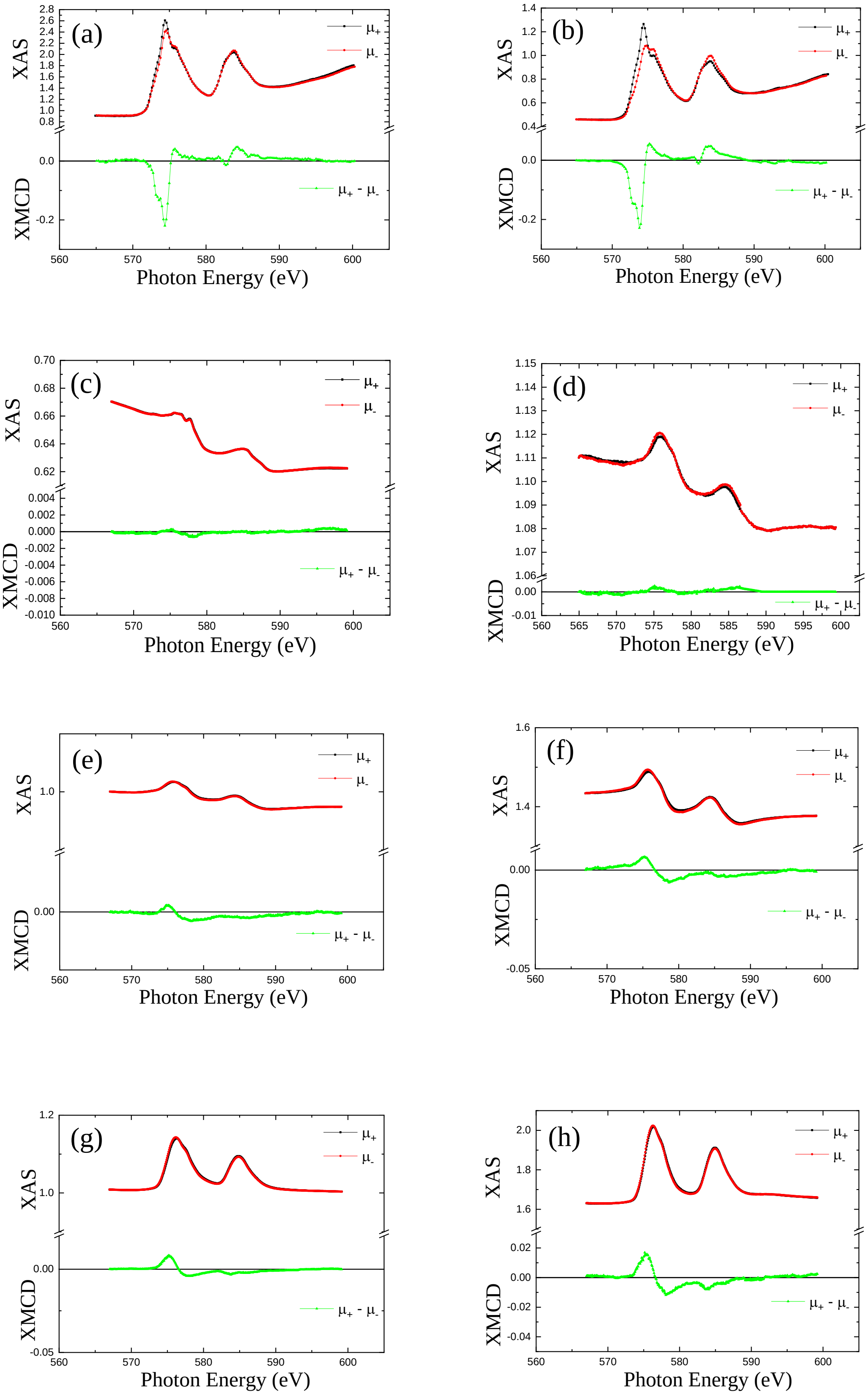
(a)
XAS
XMCD
2.8
2.6
2.4
2.2
2.0
1.8
1.6
1.4
1.2
1.0
0.8
0.0
-0.2
μ+
μ-
μ+ - μ-
560
570
580
590
600
Photon Energy (eV)
(b)
XAS
XMCD
1.4
1.2
1.0
0.8
0.6
0.4
0.0
-0.2
μ+
μ-
μ+ - μ-
560
570
580
590
600
Photon Energy (eV)
(c)
XAS
XMCD
0.70
0.68
0.66
0.64
0.62
0.004
0.002
0.000
-0.002
-0.004
-0.006
-0.008
-0.010
μ+
μ-
μ+ - μ-
560
570
580
590
600
Photon Energy (eV)
(d)
XAS
XMCD
1.15
1.14
1.13
1.12
1.11
1.10
1.09
1.08
1.07
1.06
0.00
-0.01
μ+
μ-
μ+ - μ-
560
565
570
575
580
585
590
595
600
Photon Energy (eV)
(e)
XAS
XMCD
1.0
0.00
μ+
μ-
μ+ - μ-
560
570
580
590
600
Photon Energy (eV)
(f)
XAS
XMCD
1.6
1.4
0.00
-0.05
μ+
μ-
μ+ - μ-
560
570
580
590
600
Photon Energy (eV)
(g)
XAS
XMCD
1.2
1.0
0.00
-0.05
μ+
μ-
μ+ - μ-
560
570
580
590
600
Photon Energy (eV)
(h)
XAS
XMCD
2.0
1.8
1.6
0.02
0.00
-0.02
-0.04
μ+
μ-
μ+ - μ-
560
570
580
590
600
Photon Energy (eV)

Figure 5.15 XAS and XMCD spectra of Cr atoms at L_2 and L_3 edges in Au(3nm)/Fe(10ML)/Cr/GaAs (100) films from (a) to (h). Figure (a) and (b) are the thicknesses of the Cr interlayer for the 0.1 ML and 0.2 ML films respectively. (c), (d), (e), (f), (g) and (h) are the thicknesses of the Cr interlayer for the 0.5 ML, 1 ML, 2 ML, 5ML, 15 ML and 20 ML films respectively.

Figure 5.15 indicate the XAS and XMCD spectra of Cr L_2 and L_3 edges from various thickness of Cr interlayers between 10 ML Fe layer and GaAs (100) substrate. Figure 5.15 (a) (0.1 ML Cr interlayer) and (b) (0.2 ML Cr interlayer) shows there are also two different peaks on both L_2 and L_3 edges, which is similar with the result from the Fe element; the Cr element has two different valence states in these two films. This means the Cr element is involved in the chemical compound layer. Comparing (a) and (b) with other configurations in Figure 5.15, 0.1 ML and 0.2 ML Cr interlayers show ferromagnetic properties in the XMCD part, while other thicknesses of Cr interlayers indicate antiferromagnetic properties.

As is known, the bulk Cr layer is the antiferromagnetic property[160], while in this project 0.1 and 0.2 ML Cr interlayers between 10 ML Fe layer and GaAs (100) substrate formed a chemical compound layer, allowing the magnetic property of Cr to change from antiferromagnetic to ferromagnetic. This suggests that ferromagnetic Cr was involved in the chemical compound layer, and enhanced the spin-orbital coupling from interface and increased UMA in the film. Comparing Figure 5.15 (a) with Figure 5.15 (b), the edge jump from both L_2 and L_3 edges is larger in the 0.2 ML Cr interlayer than 0.1 ML Cr interlayer, which suggests that the 0.2 ML Cr interlayer has a stronger ferromagnetic property than 0.1 ML Cr. We suggest the strong or weak ferromagnetic property in a compound layer depends on the percentage of Cr in this layer, for when the Cr achieved a fixed value in this chemical compound layer, it had the largest edge jump and strongest ferromagnetic property. If slightly over or under this value, this layer still indicated a ferromagnetic property, but one which was not as strong as that fixed value. It could then reach 0.5 ML due to too many Cr atoms on the interface; when the balance of this chemical compound layer broke, the chemical compound layer disappeared. From the XMCD part of Figure 5.15 (c) to 5.15 (h), the antiferromagnetic property is slightly amplified by the increased thickness of the Cr interlayer.

Table 5.4 Orbital moment, spin moment, total moment and orbital to spin ratio of both Fe and Cr atoms from various samples in units of u_B/atom.

Sample	Element	$m_{orb}(u_B)$	$m_{spin}(u_B)$	$m_{ratio}(u_B)$
Au(3nm)/Fe(10ML)/GaAs (100)	Fe	0.201±0.002	1.96±0.02	0.103
Au/Fe/Cr(0.1ML)/GaAs	Fe	0.208±0.004	1.99±0.02	0.105
	Cr	0.036±0.015	0.81±0.13	
Au/Fe/Cr(0.2ML)/GaAs	Fe	0.229±0.009	2.11±0.03	0.109
	Cr	0.075±0.018	1.26±0.11	
Au/Fe/Cr(0.5ML)/GaAs	Fe	0.173±0.010	1.87±0.01	0.093
	Cr	-0.013±0.021	-1.01±0.09	
Au/Fe/Cr(1ML)/GaAs	Fe	0.161±0.005	1.76±0.02	0.091
	Cr	-0.048±0.013	-1.22±0.06	
Au/Fe/Cr(2ML)/GaAs	Fe	0.148±0.003	1.68±0.01	0.088
	Cr	-0.061±0.011	-1.25±0.04	
Au/Fe/Cr(5ML)/GaAs	Fe	0.111±0.003	1.64±0.01	0.067
	Cr	-0.092±0.014	-1.33±0.08	
Au/Fe/Cr(15ML)/GaAs	Fe	0.108±0.006	1.69±0.01	0.064
	Cr	-0.089±0.016	-0.51±0.16	
Au/Fe/Cr(20ML)/GaAs	Fe	0.111±0.008	1.73±0.02	0.063
	Cr	-0.085±0.017	-0.48±0.11	
Bulk Fe[91]	Fe	0.085±0.002	1.98±0.02	0.043

Bulk Cr[160]	Cr	-0.08±0.002	-0.49±0.02	
5ML Cr[160]	Cr	-0.108±0.002	-1.32±0.02	
$Fe_{85}Cr_{15}$ Alloy[190]	Fe	0.063±0.004	2.32±0.02	0.037
	Cr	0.023±0.009	2.48±0.13	
Fe/Cr Multilayers[177]	Fe	0.143±0.004	1.95±0.02	0.073
	Cr	-0.088±0.015	-1.28±0.13	

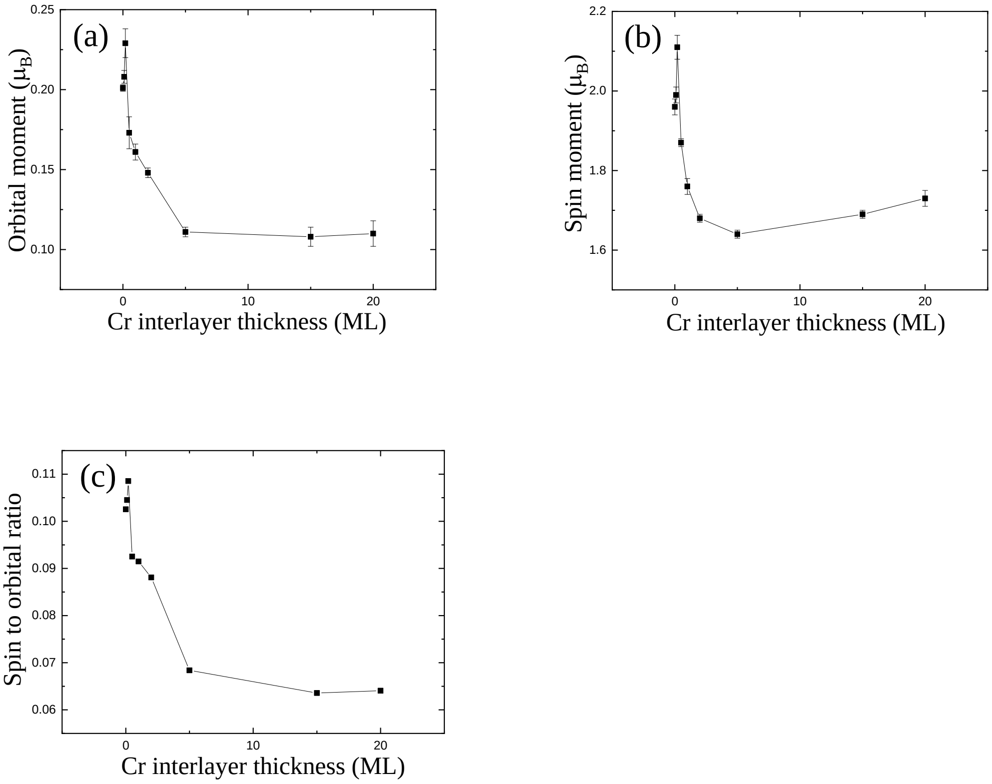

Figure 5.16 (a) and (b) show the orbital moment and spin moment of Fe atoms with different thicknesses of Cr interlayer respectively. Figure (c) gives the values for orbital to spin ratio.

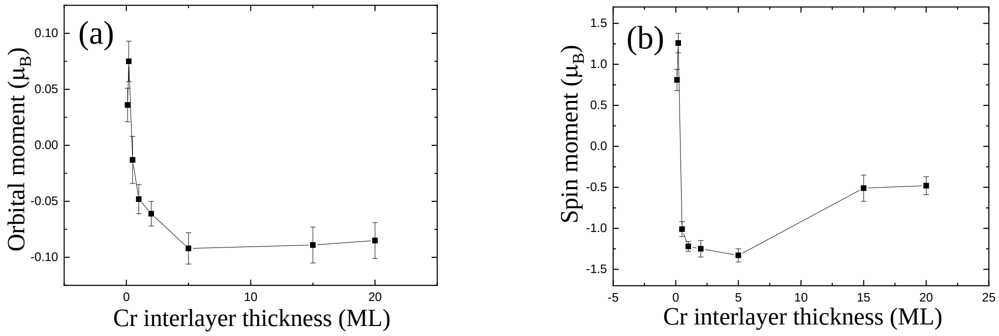

Figure 5.17 (a) and (b) indicate the orbital moment and spin moment of Cr atoms with different thicknesses of Cr interlayer between 10 ML Fe films and GaAs (100) substrate respectively.

The detailed values of spin moments, orbital moments, and spin to orbital ratios for both Cr and Fe elements are shown in Table 5.4. This table also includes the values from previous researches. The tendency charts for orbital moment, spin moment and spin to orbital ratio of Fe atoms are shown in Figure 5.16(a), (b) and (c), respectively. Firstly, the spin moment of Fe atoms in the film without a Cr interlayer are as large as 1.96u_B, which is higher than the value in the Au(3nm)/Fe(10ML)/GaAs (100) film (1.549u_B) and similar to the value of bulk Fe (1.98u_B). Because of using Cr for the capping layer, this will decrease the spin moment; as such, in this project, the spin moments of Fe (using Au as a capping layer) are larger than the last project at the beginning. The spin moment and orbital moment of Fe then experienced a small enhancement from 0 ML Cr interlayer film to 0.2 ML Cr interlayer film. This enhancement was caused by the chemical compound layer, which induced the formation of second valence state of Fe atoms in this layer. This chemical compound layer then increased the values of both the orbital moment and spin moment of Fe atoms.

When the thickness of the Cr interlayer is 0.5 ML, the Cr atoms changed from having a ferromagnetic property to being antiferromagnetic, and the chemical compound layer did not exist. As such, the orbital moment and spin moment of Fe experienced a sharp decrease. From 0.5 ML to 5 ML, the orbital moment and spin moment of Fe atoms dropped significantly. The decreased situation from the orbital moment of Fe atoms is similar to the last project, where the results were similar: UMA decreased by the increased Cr interlayer thickness, and until the Cr interlayer is 5 ML, UMA is fully blocked by the continuous Cr interlayer. However, the values of spin moment of Fe atoms from 0.5 ML to 5 ML Cr interlayer are different to the last project in section 5.1. In this project, the Au capping layer was used for all samples, meaning the symmetry breaking effect will not influence the spin moment of Fe atoms[191, 192]. In section 5.1, the spin moment of Fe atoms increased from the 0.5 ML to 5 ML Cr interlayer, while in this project, due to the enhancement from the Cr antiferromagnetic property, the spin moment of Fe atoms decreased. From the 5 ML to 20 ML Cr interlayer, the orbital moments of Fe atoms retain a similar value, around $0.11u_B$, which confirmed the conclusion from section 5.1: the 5 ML Cr interlayer formed a continuous film and fully blocked UMA. Spin moments of Fe atoms increased from the 5 ML to 20 ML Cr interlayer, which is influenced by the decrease from the antiferromagnetic property of Cr atoms. In research by Paduani *et al*[160], the value of the spin moment of Cr atoms in bulk Cr film is much smaller than that in the 5 ML Cr layer. The 15 ML and 20 ML Cr interlayers are closed to the bulk Cr film, so the spin moment of Cr was enhanced, and the spin moment of Fe influenced by the interface Cr layer also improved slightly. According to equation 3.3, the value of the spin to orbital ratio is in direct proportion to the orbital moment and inversely proportional to the spin moment, so from the 0 ML to 5 ML Cr interlayer, the spin to orbital ratio of Fe atoms has the same tendency with the orbital moment, while from the 5 ML to 20 ML Cr interlayer, there is a small decrease caused by the enhancement from the spin moment of Fe atoms.

The tendency charts for the orbital moment and spin moment of Cr atoms are shown in Figure 5.17(a) and (b), respectively. From 0.1 ML to 0.2 ML, the Cr atoms in the chemical compound layer indicated a ferromagnetic property, so the values of the orbital moment are positive. From 0.5 ML to 20 ML, those values are negative. Due to the increased thickness of the Cr interlayer, the antiferromagnetic property of Cr atoms was enhanced until 5 ML, so the values of both the spin moment and orbital moment dropped sharply. When the Cr interlayer was at 5 ML, the value of the orbital moment of Cr was similar to previous research[160]. Then, when the thickness of Cr reached 15 ML and 20 ML, the orbital moment moved around -0.087u_B, which is closer to the value for bulk Cr.

The spin moments of Cr atoms for several monolayer films and the bulk films display an enormous difference. The spin moment for bulk films are obviously higher than the several monolayer films, so from 5 ML to 20 ML, the spin moment of Cr atoms was enhanced. Comparing the 0.1 ML and 0.2 ML Cr interlayer with the other Cr structure researches, the FeCr alloy structure or the Fe-Cr multilayers structure can be ruled out in this layer[177, 190]. There are two major differences: 1) In this layer, the Fe and Cr elements both indicate two different valence states, but in other structures, there is only one valence state from XMCD observation. 2) In this layer, the values of both spin and orbital moments for Cr and Fe atoms are significantly larger than other structures. We suggest 0.1 ML or 0.2 ML Cr interlayer mixed with the As atoms and Fe atoms on the interface, which form a kind of Cr-Fe-As chemical compound layer.

5.2.6 Summary of Findings

In conclusion, we have investigated UMA, chemical compound layer and the element specific spin and orbital moments in Fe-Cr-GaAs (100) samples with an Au capping layer using magnetisation measurement, RHEED measurement, XMCD measurement and sum rule calculation. The result obtained by VSM measurement confirmed that the UMA decreased with increasing Cr interlayer, and we found a 10% enhancement when the thickness of Cr interlayer is around 0.2 ML. The RHEED measurement reveals that when Cr reaches 5 ML on GaAs (100) substrate, it goes from being an island film to a continuous film, and shows a Cr single crystalline structure. XMCD measurements present two results: firstly, a chemical compound layer is observed when the thickness of the Cr interlayer is 0.1 or 0.2 ML, which results in the Cr magnetic property changing from antiferromagnetic to ferromagnetic; secondly, this compound layer increases the spin and orbital moments for both Cr and Fe atoms, and Cr and Fe atoms have two valence states in this layer.

In the final section the origin of UMA was discussed. The conclusion from section 5.1 was confirmed. The key point is the chemical compound layer. In this layer, Cr atoms transferred from being antiferromagnetic to being ferromagnetic, and there was a stronger exchange coupling on the interface with the Fe layer and GaAs substrate. The orbital and spin moment of Fe atoms are increased in this layer, and UMA is slightly enhanced in this process.

These results would be useful for understanding the fundamental Cr element magnetic properties, which could be important for subsequent researchers as well as for applications of this chemical compound layer in the next generation of spintronic devices such as Spin-FET.

Chapter 6 Fe/Au/GaAs system

6.1 Introduction

As from the above studies of CoFeB/GaAs, CoFeB/MgO and Fe/Cr/GaAs, the orbital moments play an important role in determining the magnetic anisotropies. The heavy metals, such as Au, have a large spin-orbital coupling. If one can introduce the Au to the magnetic interface, the orbital moments and thus the magnetic anisotropies of the magnetic hetero-structures might be changed. The UMA might be influenced by the Au interlayer, and it also can confirm the previous result about the origin of UMA.

At the same time, the synthesis and structural studies of various Fe-bimetal alloys have spurred renewed interest in possible applications for recording media, magnetic microsystems and biomedicines. Recently, pure gold materials doped with iron have been extensively studied because of their unique physical and chemical properties[193-199]. Furthermore, there has been considerable recent attention about Fe-Pt alloys have because of their various technological applications, including data storage[200]. The magnetic and crystallographic properties of bulk alloys and nanoscale particles have also been studied[201, 202].

FeAu is recognized as a potential medium due to its large magneto-crystalline anisotropy via compositional and dimensional tuning[203, 204], so understanding the structures and their magnetic properties are necessary for improving the functions in application. Previous studies indicate that the room-temperature bulk structure and magnetic properties of FeAu adopt cubic[205] and tetragonal structures[206] respectively.

In order to tune the orbital moments and also understand the ultrathin FeAu structure and magnetic properties, we have performed VSM, RHEED and XMCD measurements on the films, using different thicknesses of ultrathin Au layers between the 10 ML Fe and GaAs (100) substrate.

6.2 Sample Growth

10 ML Fe films with different thicknesses of Au interlayer were grown on GaAs (100) substrates. Before deposition on the Au interlayer, the substrate surface was etched and cleaned. Firstly, the contaminants of the substrate surface were removed using acetone, iso-propyl alcohol (IPA) and deionized water. The second step was to remove the oxide layer by immersing the substrate in an $H_2SO_4/H_2O_2/H_2O$ (4:1:1) solution for 45 seconds. Both steps were performed in a level 100 clean room to prevent any dust particle contamination. The third step was to create a flat surface for film deposition. The etched substrate was immediately transferred into a MBE chamber with a base pressure of 2.3×10^{-10} mbar, before the substrate was treated with ion-milling before annealing. It should be noted that low energy Argon ion beams were sputtered onto the substrate surface for 30 minutes, so that they gently removed a thin layer of surface material, exposing the virgin layer of the substrate. The penultimate step is annealing: the substrate was required to be annealed at 480°C (at an annealing pressure lower than 8×10^{-9} mbar) for 60 minutes in order to further remove natural oxides and create surface reconstruction. The surface is allowed to cool to room temperature prior to film growth. The Au interlayer and 10 ML Fe layers were grown by the two different source evaporators in the MBE system at a pressure lower than 2.1×10^{-9} mbar. Finally, a 3 nm Cr capping layer was deposited to prevent the 10 ML Fe film from oxidisation.

6.3 RHEED Patterns and Analysis

Since the substrates or samples are located within an UHV environment, the most effective mechanism for examining the surface quality and morphology in our system is the RHEED pattern. The main advantages of RHEED are that it is in-situ, fast, and surface sensitive. An electron gun with a high energy range between 10 and 50 keV provides an electron beam which impinges upon a given sample surface at an angle about 1°, and is diffracted on the fluorescent screen. This means detailed surface information can be observer from the screen.

Figure 6.1 shows the RHEED patterns from GaAs (100) substrates, the Au interlayers of various thicknesses and 10 ML Fe films. From the RHEED patterns for 10 ML Fe films, when the thickness of the Au interlayer is from 0 ML to 0.5 ML, the RHEED pattern for Fe films show a single crystalline structure. When the Cr interlayer is from 1 ML to 2 ML, the RHEED patterns show a combination of single crystalline and polycrystalline structures. Finally, when the Au interlayer reaches 5 ML, the 10 ML Fe film preformed the fully polycrystalline structure.

Lattice mismatch is the main reason that the structure formed by the Fe film was polycrystalline. The lattice constant of 2.87Å for Fe is almost exactly half that of GaAs (5.65 Å), meaning it is easy to form a single crystalline structure on GaAs substrate. However, the lattice constant for Au is 4.065 Å – a huge difference when compared to GaAs or Fe – meaning that when the Au interlayer grew on the GaAs substrate, the lattice mismatch was amplified alongside the increasing thickness of the Au interlayer. In addition, when the Au interlayer formed a continuous film, the 10 ML Fe layer indicated a polycrystalline structure. The large lattice mismatch between Au and GaAs formed a rough surface morphology. As for the 0.2 ML to 0.5 ML Au interlayer RHEED patterns, there were a few points on the screen, meaning that the films were island films and the surface morphology was rough. As for the 1 ML to 2 ML Au interlayer, although the surface remained rough, there were more points on the screen and the formation tendency were close to the line (single crystalline structure). Finally, the 5 ML Au interlayer formed a single crystalline structure and there was a flat continuous film.

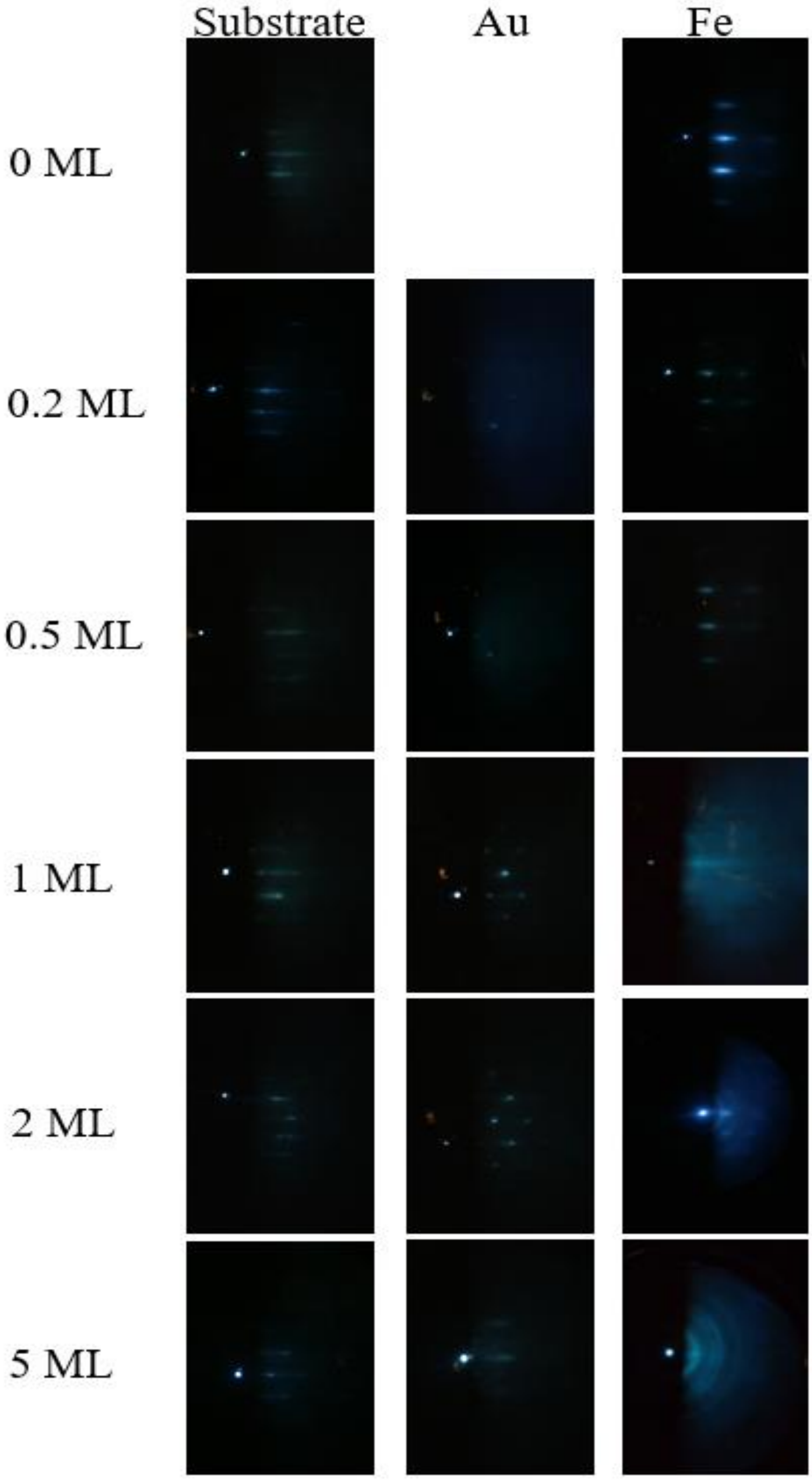

Figure 6.1 shows the RHEED patterns from GaAs (100) substrates ($[0\bar{1}1]$ view), the various thicknesses of Au interlayers and 10 ML Fe films which grew on the Au interlayer. The thickness of the Au interlayer is from 0ML to 5ML, and the thickness of Fe remains 10ML.

6.4 VSM Measurement and Analysis

The in-plane magnetic hysteresis loops of all the samples were measured with both $[0\bar{1}1]$(easy axis) and [011] (hard axis) using a Vector Magnetometer Model 10 VSM and Vector measurement system at room temperature (300K), as shown in Figure 6.2. Since a strong uniaxial magnetic anisotropy field as large as 1790.8 Oe was expected in the Cr(3nm)/Fe(10 ML)/GaAs (100) sample along the hard axis, the VSM measurement was conducted using a maximum magnetic field of 3000 Oe to ensure that all samples were fully saturated.

All the easy axis loops from Figure 6.2 have a similar shape, which means that the easy axis cannot be influenced by the Au interlayer. As can be seen in the hard axis loops in Figure 6.2, the saturation field changed according to the varying thickness of the Au interlayers. For the 0 ML to 0.5 ML Au interlayers, the values of the saturation field along the hard axis were enhanced, while at the 0.5 ML Au interlayer, the saturation field achieved its highest value of 1950.6 Oe. This was enhanced by almost 10% compared with the sample which did not have an Au interlayer. From 0.5 ML to 5 ML, the saturation field decreased from 1950.6 Oe to 59.3 Oe, which is a significant drop. When the Au interlayer reached 5 ML, UMA disappeared (easy and hard axis loops have a similar shape), thereby confirming the results identified in chapter 5, namely that UMA originates via Fe-As chemical bonding. When the interlayer film formed a continuous film, the bonding was cut by the interlayer, and so the UMA was blocked.

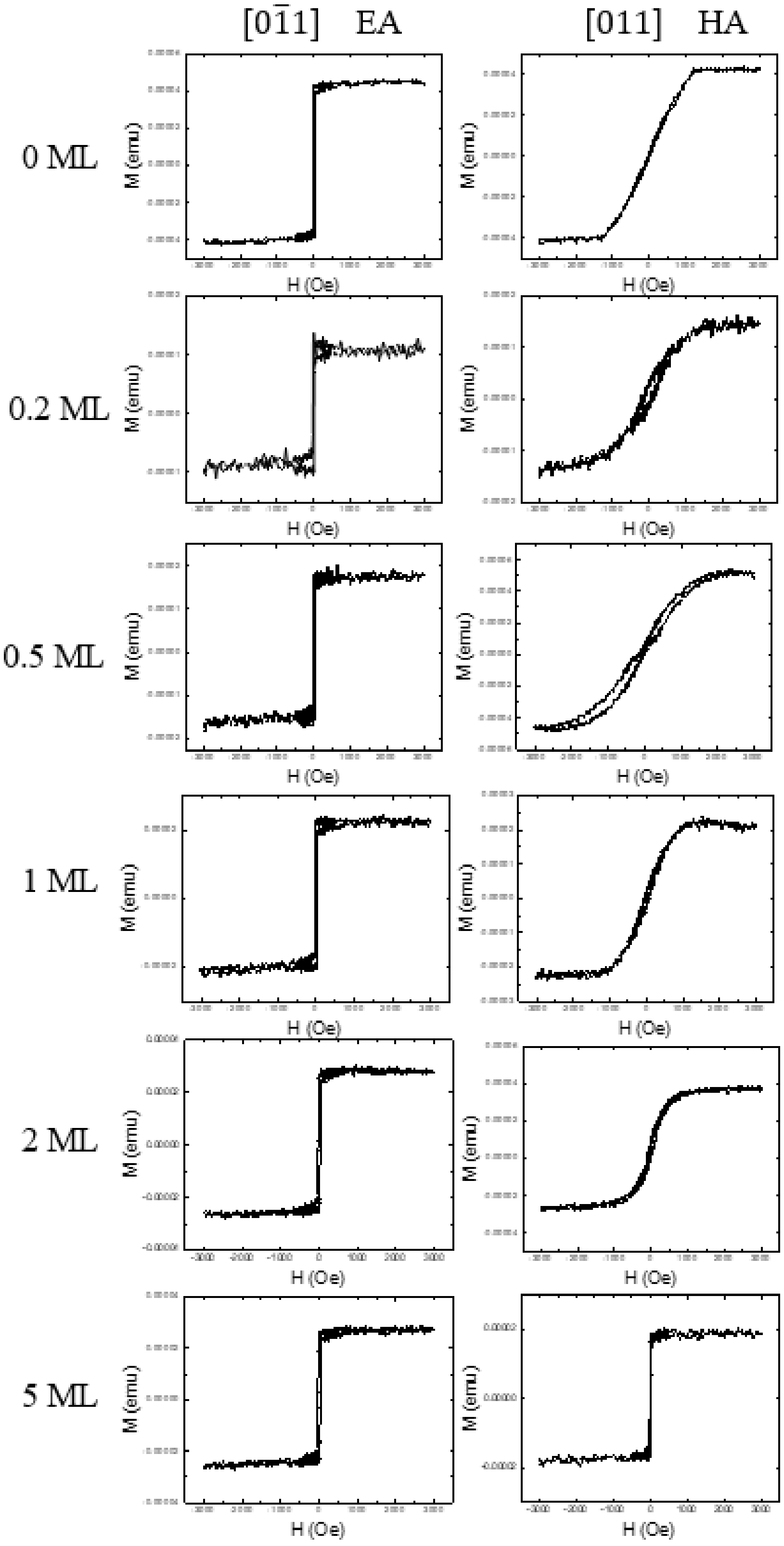

Figure 6.2 VSM hysteresis loops of various Au interlayer thickness (from 0 to 5ML) between GaAs (100) substrate and 10 ML Fe. These loops are all measured at room temperature with the 3000 Oe magnetic field applied along [011] and $[0\bar{1}1]$ (hard axis and easy axis respectively).

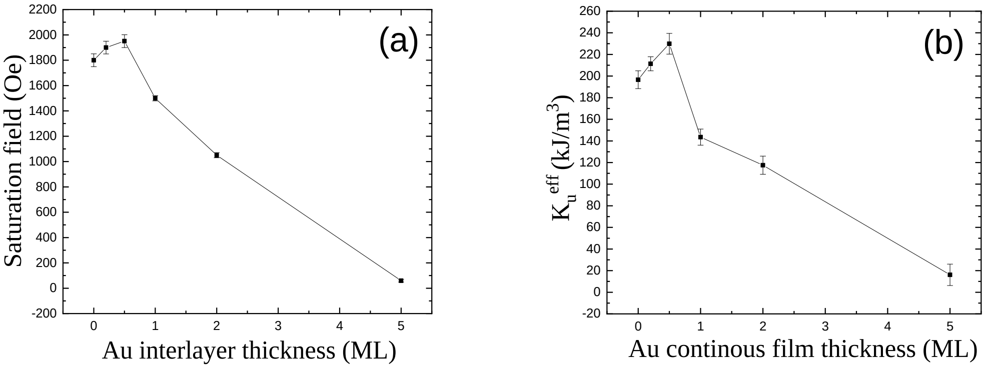

Figure 6.3 (a) and (b) are the tendency charts for the saturation field and effective uniaxial anisotropy constant respectively.

Table 6.1 The values of the saturation field and effective uniaxial anisotropy constant for various thicknesses of Au interlayers between 10 ML Fe single crystalline film and GaAs (100) substrate.

Sample	Saturation field (Oe)	$K_u^{eff}(kJ/m^3)$
Cr(3nm)/Fe(10ML)/GaAs (100)	1790.8 ± 25.3	196.6 ± 8.2
Cr(3nm)/Fe(10ML)/Au(0.2ML)/GaAs (100)	1899.9± 25.4	211.3± 6.5
Cr(3nm)/Fe(10ML)/Au(0.5ML)/GaAs (100)	1950.6± 24.5	229.9 ± 9.6
Cr(3nm)/Fe(10ML)/Au(1ML)/GaAs (100)	1440.6 ± 25.5	143.5 ± 7.5
Cr(3nm)/Fe(10ML)/Au(2ML)/GaAs (100)	1050.1 ± 26.4	97.5 ± 8.4
Cr(3nm)/Fe(10ML)/Au(5ML)/GaAs (100)	59.3 ± 10.5	16.1 ± 9.9

The value of the UMA field (H_K) can be obtained from the saturation field in the hard axis direction. Furthermore, the effective uniaxial anisotropy constant (K_u^{eff}) can be calculated using equation 4.1, which was mentioned in chapter 4. Table 6.1 presents the detailed data for the values of the saturation field and the effective uniaxial anisotropy constant. The trend-lines for the saturation field and effective uniaxial anisotropy constant are shown in Figure 6.3 (a) and (b) respectively. The starting point in this project contains similar values for the saturation field and effective uniaxial anisotropy constant, with the same sample in Section 5.1. This indicates our growth and measurement equipment are stable and that the experiments are repeatable. Because the values of effective uniaxial anisotropy constant are in direct proportion to changes in the saturation field, this value has a similar tendency with to the value of saturation field, which increased in the Au interlayer from 0 ML to 0.5 ML and which dropped in the Au interlayer from 0.5 ML to 5 ML. It is suggested that the reason for the enhancement of the saturation field and the effective uniaxial anisotropy constant in the 0 ML to 0.5 ML Au interlayer is the kind of FeAu alloy formed on the GaAs (100) substrate. This has the effect of slightly increasing the saturation field along the hard axis. Detailed discussions on this are presented below in Section 6.5.

6.5 XMCD Measurements and Analysis

XMCD measurements were performed at normal incidence to the Cr(3nm)/Fe(10 ML)/Au/GaAs (100) samples in the I10 station from Diamond Light Source. The XMCD spectra were measured at both positive and negative applied fields for Fe atoms. The data were collected by a Total Electron Yield (TEY) detector in the analysis chamber under a magnetic field of 1T. The samples were measured at a 60-degree angle along the perpendicular direction and all in room temperature (300K).

The XAS and XMCD spectra of Fe L_2 and L_3 edges for 10 ML Fe films with various thicknesses of Au interlayers on GaAs (100) substrate are shown in Figure 6.4 from (a) to (f). Au atoms have a no-magnetic property, meaning that it is not necessary make an XMCD measurement for Au atoms. As regards XAS, u_+ and u_- are the absorption coefficients under antiparallel and parallel magnetic fields to the photon incident direction. XMCD shows the value of $u_+ - u_-$ and the integrated value from $u_+ - u_-$, data which are used for calculating using XMCD sum rules. According to XMCD sum rules, the orbital (m_{orb}) and spin (m_{spin}) magnetic moments and the ratio (m_{ratio}) of m_{orb} to m_{spin} can be determined from XAS and XMCD spectra using equations from 3.1 to 3.7, which were described in chapter 3. Following Chen *et al*[91], the value of n_{3d} for the Fe element of 6.61 was used to calculate all the results.

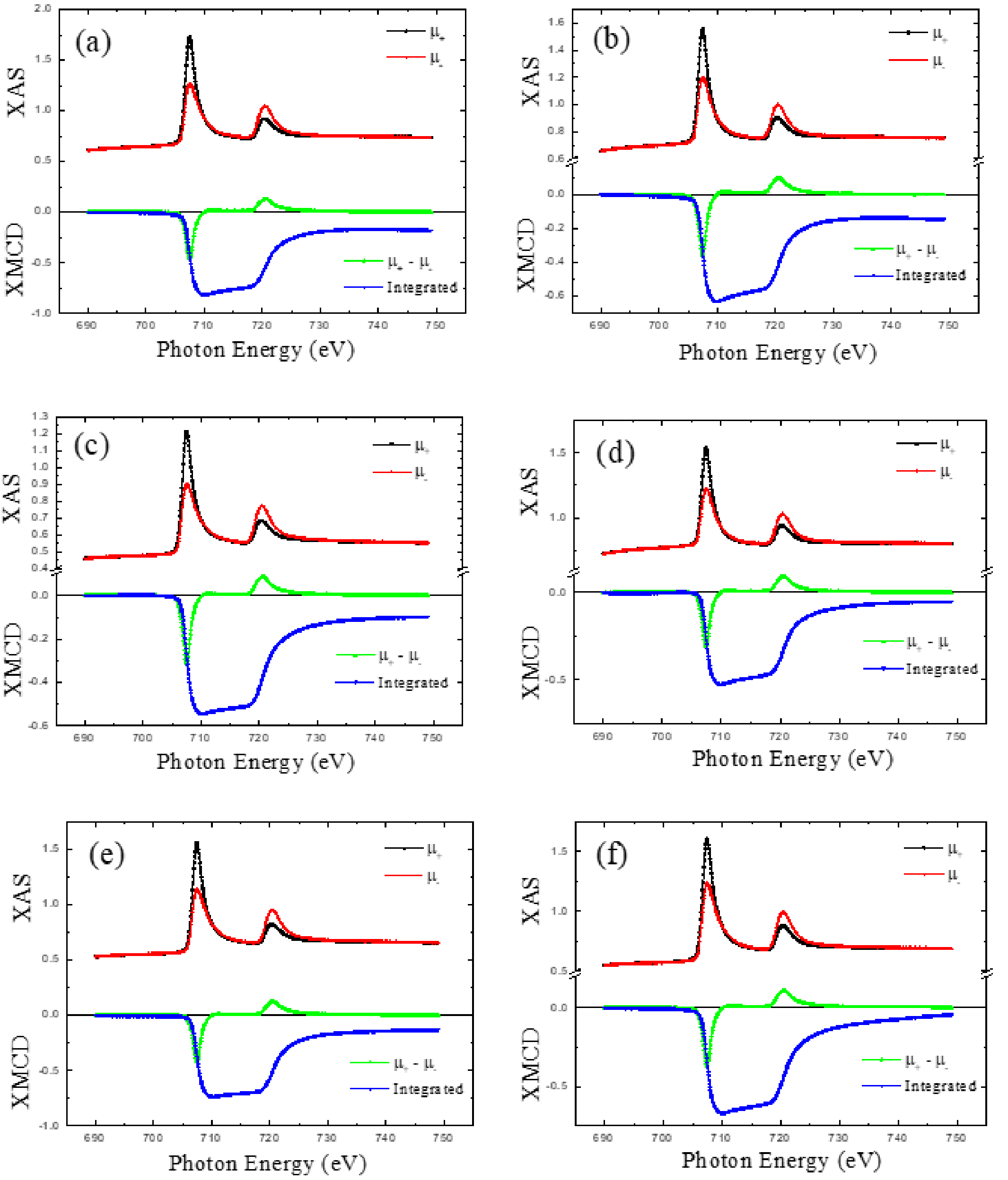

Figure 6.4 XAS and XMCD spectra of Fe atoms at L_2 and L_3 edges in Cr(3nm)/Fe(10ML)/Au/GaAs (100) from (a) to (f): (a), (b), (c) are the thickness of Au interlayer for 0ML, 0.2 ML and 0.5 ML respectively. (d), (e), (f), are the thickness of Au interlayer for 1 ML, 2 ML and 5ML respectively.

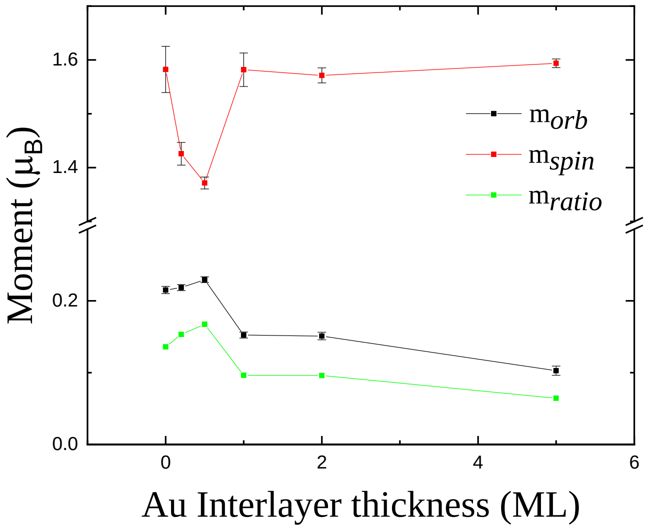

Figure 6.5 presents black and red lines which show the orbital moment and spin moment of Fe atoms with different thicknesses of Au interlayers. The green line gives the values for the orbital to spin ratio.

Table 6.2 indicates the orbital moment, spin moment and orbital to spin ratio of Fe atoms from various samples in units of u_B/atom.

Sample	$m_{orb}(u_B)$	$m_{spin}(u_B)$	$m_{ratio}(u_B)$
Cr(3nm)/Fe(10ML)/GaAs (100)	0.215±0.005	1.58 ±0.04	0.136
Cr(3nm)/Fe(10ML)/Au(0.2ML)/GaAs (100)	0.219±0.004	1.43±0.02	0.153
Cr(3nm)/Fe(10ML)/Au(0.5ML)/GaAs (100)	0.230±0.004	1.37±0.01	0.167
Cr(3nm)/Fe(10ML)/Au(1ML)/GaAs (100)	0.153±0.004	1.58±0.03	0.096
Cr(3nm)/Fe(10ML)/Au(2ML)/GaAs (100)	0.151±0.005	1.57±0.01	0.096
Cr(3nm)/Fe(10ML)/Au(5ML)/GaAs (100)	0.102±0.006	1.59±0.01	0.063
$Fe_{90}Au_{10}$ alloy[207]	0.243±0.003	1.63±0.02	0.149
Fe/Au multilayers[208]	0.108±0.002	1.92±0.02	0.056
Bulk bcc Fe[91]	0.085	1.98	0.043

The values for the orbital moment, spin moment and orbital to spin ratio of Fe atoms are shown in Table 6.2, and the values for FeAu alloy, Fe/Au multilayers and bulk Fe films are also included in this table for comparison purposes. The tendency charts for the orbital moment, spin moment and spin to orbital ratio of Fe atoms are shown in Figure 6.5, using black, red and green lines respectively. With the exception of the 0.2 and 0.5 ML Au interlayer, the spin moment of Fe retains a very similar value, which is slightly lower than the value for bulk bcc structure Fe film ($1.98u_B$). Since the 3 nm Cr capping layer was used for all samples, and the Cr layer decreased the spin moment, the Fe spin moment decreased to $1.58u_B$ for all samples which did not have 0.2 and 0.5 ML Au interlayer samples.

The red line in Figure 6.5 shows that the spin moment experienced a sharp decrease in the Au interlayer from 0 to 0.5 ML, before it reversed for the 0.5 to 1 ML Au interlayer. The Fe/Au multilayer film had a similar spin moment value ($1.92u_B$) as the bulk Fe film, while the value for the FeAu alloy film was much lower, meaning that the formation of the FeAu alloy decreases the Fe spin moment. Because the Cr capping layer also influenced the Fe spin moment, so the values of the spin moment for 0.2 and 0.5 ML Au interlayer films are even lower than $1.63u_B$. This might suggest the 0.2 and 0.5 ML Au formed the FeAu alloy with Fe atoms on the surface, and that this alloy layer decreased the spin moment of Fe atoms.

Comparing the tendency for the spin moment, orbital moment and UMA, one result can be confirmed: the spin moment has no relationship to UMA, but the orbital moment has a strong connection with UMA. The orbital moment of Fe atoms was enhanced from 0 to 0.5 ML Au interlayer, and then dropped for the 0.5 to 5 ML Au interlayer. For the 1 to 5 ML Au interlayer, the orbital moment of Fe atoms dropped by increasing the Au interlayer. If the Fe polycrystalline structure became increasingly obvious on the RHEED screen, the Fe orbital moment decreased sharply, especially when the thickness of the Au interlayer was 5 ML (the Au interlayer was a single crystalline structure while the Fe film was a fully polycrystalline structure), the orbital moment of Fe significantly decreased and was at its lowest value ($0.102u_B$).

This result also confirmed our previous conclusion in chapter 5: when the interlayer film formed the continuous film, UMA was fully blocked, and that since the origin of UMA is from the chemical bonding between Fe and As atoms, if this bonding is cut by the appropriate thickness of interlayer, UMA would not be formed in the Fe-GaAs system. In addition, compared to the sample without the Au interlayer, the 0.5 ML Au interlayer was enhanced by 7%, and then as the thickness of Au interlayer increased, the orbital moment decreased significantly. The values of the Fe orbital moment in the samples with the 0.2 and 0.5 ML Au interlayer are close to the value of the FeAu alloy ($0.24u_B$), and almost double the value of the Fe/Au multilayers ($0.11u_B$), which could rule out the Fe/Au multilayers structure formed on the GaAs surface. From Figure 6.4, it can be seen that there is only one peak on the XAS spectra of Fe atoms for both L_2 and L_3 edges, so the possibility of a chemical compound layer can be ruled out. We suggest that the 0.2 and 0.5 ML Au formed the FeAu alloy with Fe atoms on the GaAs (100) surface, and this FeAu alloy enhanced the orbital moment of Fe atoms but decreased the spin moment of Fe atoms.

According to equation 3.3, the value of the spin to orbital ratio is in direct proportion to the orbital moment and inversely proportional to the spin moment, so for the Au interlayer from 0 ML to 5 ML Au, the spin to orbital ratio of Fe atoms has the same tendency as the orbital moment, meaning the FeAu alloy has a stronger spin-orbital exchange coupling than the ultrathin Fe film on GaAs (100) substrate.

6.6 Summary of Findings

In conclusion, we have investigated UMA and the element specific spin and orbital moments for Fe atoms in Fe/Au/GaAs (100) samples with a Cr capping layer using magnetisation measurement, RHEED measurement, XMCD measurement and sum rule calculation. RHEED patterns indicate the surface morphology for Au atoms grows on the GaAs substrate and 10 ML Fe layer on the various Au interlayer. We found that large lattice constant Au atoms grow on the GaAs (100) substrate and the sample surface is rough, and formed a single crystalline structure at 5 ML; the Fe RHEED patterns show the single crystalline structure from the 0 to 0.5 ML Au interlayer, while when the thickness of the Au interlayer is 1 or 2 ML, the Fe RHHED pattern indicates the combination of a single crystalline and polycrystalline structure. Finally, when the Au interlayer is 5 ML, the RHEED patterns for Fe yielded a fully polycrystalline structure. The result obtained by VSM measurement found that UMA increased when the thickness of the Au interlayer is 0.2 or 0.5 ML, and then decreased when the Au interlayer was thicker. XMCD data evidenced the 0.1 and 0.2 Au interlayer formed an FeAu alloy on the GaAs (100) surface, and this FeAu alloy interlayer enhanced the orbital moment of Fe atoms but decreased the spin moment.

The origin of UMA was discussed in the previous chapter, and the conclusions from Section 5.1 and 5.2 are also confirmed in this chapter. One aspect of particular note is that the FeAu alloy might be formed in the interlayer. In this alloy layer, Fe atoms had stronger exchange coupling on the interface with the Fe layer and GaAs substrate. The values of the Fe orbital moment are increased in this layer, which also resulted in the slight enhancement of UMA. Compared with Cr interlayer system, the Cr interlayer will decrease the spin moment of Fe, so the spin-orbital ratio got increased, and the very thin Cr interlayer (0.1 or 0.2 ML Cr) formed a kind of chemical compound layer with Fe and As, and this compound layer slightly increased the UMA and spin to orbital coupling.

These results will be useful for understanding the interface interaction from the heavy metal element interlayer and the influence from Fe-bimetal alloys on the UMA, which is necessary for improving the functions in magnetic recording applications.

Chapter 7 Conclusions and Future Work

7.1 Conclusions

In my thesis, I have studied the growth, structure and magnetic properties of several magnetic heterostructures with GaAs and MgO. The main conclusions drawn from the results for each system are as follows:

CoFeB /GaAs (100)

The CoFeB sample was prepared using magnetron sputtering growth on the GaAs (100) substrate. The in-plane and out-of-plane magnetic properties were studied using VSM and polar MOKE measurements respectively. The results obtained using VSM and MOKE measurements confirmed that UMA can achieve as large as 270 Oe, which is among the largest UMA observed in any CoFeB amorphous alloy.

The XAS and XMCD data were systematically analysed using integration and the sum rules approach. The processed data gave an indication of the magnetic orbital and spin moments of both the Fe and Co elements within the film. XMCD measurements revealed that the UMA is correlated with a strong spin-orbit coupling related to the enhanced orbital to spin moment ratios of both Fe and Co in the CoFeB. More importantly, the spin moment of the Co was found to remain as large as that of the crystalline hcp Co, and the orbital moments were enhanced by more than 370%, suggesting the dominant contribution of the spin-orbit coupling of the Co atoms to the UMA in the CoFeB/GaAs (100) amorphous film.

TEM cross section inspections indicated that the film structure was as expected, and that the interface between the CoFeB film and GaAs substrate were clear. The surface roughness was kept at a minimum, and there was no strong sign of deep inter-fusion between the two materials. The images also showed no evidence of shape anisotropy since the film was clearly amorphous. The one remaining reason for its large UMA behaviour was presumably that it came from interface bonding. This also matches previous research results published elsewhere. We conclude that this sample composition and preparation technique can be used to better control, and indeed enhance, the UMA interface. Ultimately this will enable the fabrication of more efficient spintronic devices.

CoFeB/MgO structure

The CoFeB/MgO structure samples on Si (001)/SiO_2 substrate were prepared by DC and RF sputtering evaporators. Both in-plane and out-of-plane magnetic hysteresis loops were measured using VSM measurement. The PMA effect was found on sample A (Ta (5)/MgO (3)/CoFeB (1.2)/Ta (5)) and B (Ta (5)/CoFeB (1.2)/MgO (3)/CoFeB (1.2)/Ta (5)) whilst there was no PMA effect in this film without the MgO layer in sample C (Ta (5)/CoFeB (1.2)/Ta (5)). The spin moment and orbital moment of both the Fe and Co elements were measured using XMCD and calculated by the sum rule. XMCD measurement reveals that the PMA is correlated with a strong spin-orbital coupling of Co atoms related to the enhanced orbital to spin moment ratios of Co atoms in the CoFeB/MgO structure. More importantly, comparing the samples which have a PMA effect with those which do not, the values of the Co orbital moment is almost double the sample with PMA, and the orbital moment of Fe atoms show no significant change. This suggests the dominant contribution to PMA in the CoFeB/MgO structure is the orbital moment of Co atoms. We conclude that the PMA is correlated with the orbital moment of Co, and Co atoms play the important role on the interface. This discovery would improve the fabrication of electronic device based on MRAM structure.

Cr/Fe/Cr/GaAs (100)

Various thicknesses of Cr interlayer were grown between the 10 ML Fe layer and GaAs substrate by the MBE system. Through the Cr RHEED patterns, the single crystalline structure of Cr was shown when the thickness of Cr was at 5 ML, which formed a continuous film. As the Fe and Cr have a similar lattice constant, so the lattice mismatch between Fe and Co atoms would not influence the structure of Fe 10 ML, meaning that all Fe layers presented a single crystalline structure.

Through the VSM results, when the Cr interlayer was from 0.5 ML to 2 ML, the values of UMA decreased significantly. When the Cr interlayer was from 5 to 20 ML, the saturation field along the hard axis moved around 56 Oe, and the UMA disappeared. In particular, when the Cr interlayer was 5 ML, the Cr interlayer formed a continuous film and cut the bonding between the Fe and As atoms, meaning it fully blocked UMA from the 5 ML Cr interlayer.

The XMCD measurements indicate two points: firstly, that the Cr interlayer and Cr capping layer can adjust the Fe spin moment because of the symmetry breaking; secondly, that UMA is correlated with orbital moment and spin to orbital ratio, which is due to the thickness of the Cr interlayer. It has no relationship with the spin moment of Fe. These results refer to the origin of UMA. It appears that the chemical bonding between As and Fe atoms is the major reason for UMA, and if this bonding were to be cut by the interlayer, UMA would not exist. This evidence of the origin of UMA is from the interface bonding rather than the lattice mismatch related film stress.

In conclusion, the origin of UMA in Fe-GaAs system is from interface interaction or interface chemical bonding between Fe and As atoms. This important result would be helpful for understanding the basic knowledge of Fe-GaAs system and enable the fabrication of electronic device based on spinFET structure.

Au/Fe/Cr/GaAs (100)

The Au/Fe/Cr/GaAs (100) samples were prepared using an MBE system. There were three different sources in the evaporator, with the various thicknesses of interlayers deposited by a Cr source. The results from RHEED were very similar to the Cr/Fe/Cr/GaAs (100) system: Cr formed a continuous film with a single crystalline structure at 5 ML, while the structure for the 10 ML Fe films remained as a single crystalline structure. The results obtained using VSM measurement confirmed the results in the Cr/Fe/Cr/GaAs (100) system, namely that the UMA was decreased when the Cr interlayer increased (from 0.5 to 20 ML), and when the thickness of Cr was 5ML, the UMA was fully blocked. When the thickness of the Cr interlayer was around 0.2 ML, a 10% increase in UMA was found in the film.

Through XMCD measurement, there were two different valence states on both Fe and Cr atoms from XAS spectra when the Cr interlayer was 0.1 or 0.2 ML, meaning the chemical compound layer formed on the GaAs surface. In this chemical compound layer, the magnetic property of Cr changed from being antiferromagnetic to ferromagnetic. The spin and orbital moments for both Cr and Fe atoms increased in this layer.

The origin of UMA has been discussed in the Cr/Fe/Cr/GaAs (100) system. The conclusion concerning the Cr/Fe/Cr/GaAs (100) system can also be confirmed in this system. The more interesting point concerns the chemical compound layer. In this layer, Cr atoms transformed from being antiferromagnetic to ferromagnetic, and had a stronger exchange coupling on the interface. The orbital and spin moment of Fe atoms were increased in this layer, and the UMA was slightly enhanced in the process. We conclude that the chemical compound layer was found on the interface. This chemical compound layer enhanced UMA, and in this process, the magnetic property of Cr interlayer changed from antiferromagnetic to ferromagnetic. This result will be useful for understanding the magnetic property of Cr element in Fe-GaAs system.

Cr/Fe/Au/GaAs (100)

The 10 ML Fe films with different thicknesses of Au interlayer were grown on GaAs (100) substrates by an MBE system equipped with a RHEED gun. Due to the large lattice constant of Au atoms, the RHEED patterns for the Au interlayer from 0.2 to 2 ML were rough, and when the Au interlayer reached 5 ML, the RHEED pattern indicated a single crystalline structure, meaning that the Au had already formed a continuous film at 5 ML. The RHEED patterns for the Fe layer remained as a single crystalline structure for the 0 to 0.5 ML Au interlayer, while from 1 to 2 ML, the combination of a single crystalline and polycrystalline structure was displayed on the RHEED screen. When the Cr interlayer reached 5 ML, the Fe layer formed a fully polycrystalline structure.

Through VSM measurement, UMA increased when the thickness of the Au interlayer was 0.2 or 0.5 ML, and then decreased by the thicker Au interlayer. When the Au interlayer reached 5 ML, the UMA and effective uniaxial anisotropy constant received the smallest values.

XMCD data provided evidence that the 0.1 and 0.2 Au interlayer formed an FeAu alloy on the GaAs (100) surface, and this FeAu alloy interlayer enhanced the orbital moment of Fe atoms but decreased the spin moment. In the FeAu alloy layer, Fe atoms had a stronger exchange coupling on interface. The values of the Fe orbital moment were increased in this layer, which influenced the enhancement for UMA. In conclusion, there is an FeAu alloy which might have formed on the interface, and this alloy structure may have slightly increased the UMA by an interface interaction with the GaAs (100) substrate. This result gives the influence of alloy layer on the semiconductor substrate, and it will be helpful for the research of interface magnetic properties with alloy structure.

In summary, the CoFeB/GaAs(100) and CoFeB/MgO systems evidenced the Co atoms play important role on the interface, and Co atoms have a large influence on both UMA and PMA in CoFeB system. Ultimately this will enable the fabrication of next generation electronic devices based on the MRAM structure. In the later three systems (Cr/Fe/Cr/GaAs(100), Au/Fe/Cr/GaAs(100) and Cr/Fe/Au/GaAs(100)), they all evidenced the UMA in Fe-GaAs system is from the Fe-As chemical bonding, if an interlayer formed a continuous film and cut this bonding, the UMA would not have existed. In the Au/Fe/Cr/GaAs(100) system, the Fe-Cr-As chemical compound interlayer was found in this system and enhanced the UMA; in Cr/Fe/Au/GaAs(100) system, the FeAu alloy interlayer might form on the GaAs substrate, and this alloy structure may have enhanced UMA. From results of these three systems, it could be seen that the interface is very important for the UMA, and with the different structures, the UMA was influenced significantly. Research of the UMA in Fe-GaAs system would be very useful for fabrication of electronic devices based on spinFET structure.

7.2 Future Work

Further to the conclusions drawn in this thesis, there are still many open questions. For further research purposes, the following ideas are suggested as consideration.

For the XMCD measurements of CoFeB on the GaAs (100) sample, a further measurement could be done in order to strengthen the results. The samples could be measured at a much larger magnetic field, one that is big enough to reach the saturation point. The spectra taken at that point would give confirmed data to calculate the orbital and spin magnetic moments of each element.

For the CoFeB/ MgO structure researches, more samples could be designed for comparing, for example Ta(5)/MgO(3)/CoFeB(1.2)/MgO(3)/Ta(5), Ta(5)/CoFeB(0.6)/MgO(1.2)/CoFeB(0.6)/Ta(5) and Ta(5)/CoFeB(0.4)/MgO(1.2)/CoFeB(0.8)/Ta(5). These multilayer samples have very interesting combinations which could help us research the PMA effect from the CoFeB/MgO structure more deeply.

For the Au/Fe/Cr/GaAs (100) and Cr/Fe/Cr/GaAs (100) systems, more TEM images could be measured for these samples to strengthen the results, and more specific sample structure and morphology could be compared to the RHEED results. In the Au/Fe/Cr/GaAs (100) system, the XPS (X-ray photoelectron spectroscopy) measurement could be done for 0.1 and 0.2 Cr interlayer samples, which could analyse the specific valence states for Cr and Fe atoms, thus the type of compounds layer could be confirmed from the results. In the Au/Fe/Cr/GaAs (100) system, it is better to get the STM (scanning tunnelling microscope) images in a vacuum chamber when growing the Cr interlayer from 0 to 5 ML. This could help us understand the formation process of a Cr single crystalline structure, and would be very useful for researching the Cr atoms on the GaAs surface.

For the Cr/Fe/Au/GaAs (100) system, there are some measurements which could be undertaken to strengthen the results. More Au interlayers of different could be inserted between Fe and the GaAs (100) substrate, such as 0.1, 0.3, 3, 7, 10, 15 ML Au interlayers. These Au interlayers could let us study the generated and disappeared conditions of the FeAu alloy and provide clearer results. TEM measurement could also be undertaken on this project, with TEM images providing evidence concerning the formation of FeAu alloy structure on the GaAs surface.

Last but not least, since all the experiments are heavily dependent on the performance and condition of the equipment, any improvements done to them are welcome so as to ease the difficulties of the operator. Powerful processing capabilities, the reliable and reasonable design of the hardware and a clearer design of user interface could further improve the lab efficiency, thereby bringing more opportunities for greater discoveries.

List of Abbreviations

AFM	Atomic Force Microscopy
BCC	Bulk centred cubic
BOA	Bond orientational anisotropy
CVD	Chemical Vapour deposition
CIP	Current in plane
CPP	Current perpendicular to plane
DC	Direct current
DI	De-ionized (water)
DFT	Density functional theory
DMO	Dilute magnetic oxides
DW	Domain Wall
EA	Easy axis
FCC	Face Centred Cubic
FET	Field Effect Transistor
FM	Ferromagnetic
GMR	Giant Magneto resistance
HA	Hard axis
HV	High Voltage
HM	Half-Metallic

HCP	Hexagonal close packed
IC	Integrated circuits
IT	Information Technology
IPA	Iso-Propyl Alcohol
LED	Light Emitting Diode
LEED	Low-Energy Electron Diffraction
MCA	Magnetocrystalline anisotropy
MTJ	Magnetic tunnel junction
MBE	Molecule Beam Epitaxy
MOKE	Magneto-Optical Kerr Effect
ML	Monolayer
MR	Magneto resistance
PLD	Pulse Laser Deposition
PIPS	Precision ion polishing system
RHEED	Reflection High-Energy Electron Diffraction
RAM	Random Access Memory
RT	Room Temperature
SC	Semiconductor
SQUID	Superconducting Quantum Interference Device
STT	Spin transfer torque

STM	Scanning tunnelling microscope
TM	Transition metal
TEM	Transmitting Electron Microscope
TSP	Titanium Sublimation Pumps
TEY	Total electron yield
TMR	Tunnel Magneto resistance
UHV	Ultra-High Vacuum
VSM	Vibrating Sample Magnetometer
XAS	X-ray Absorption Spectra
XPS	X-ray photoelectron spectroscopy
XMCD	X-ray Magnetic Circular Dichroism

References

[1] M. Johnson and R. H. Silsbee, "Interfacial charge-spin coupling: Injection and detection of spin magnetization in metals," *Physical Review Letters,* vol. 55, no. 17, p. 1790, 1985.

[2] M. N. Baibich *et al.*, "Giant magnetoresistance of (001) Fe/(001) Cr magnetic superlattices," *Physical review letters,* vol. 61, no. 21, p. 2472, 1988.

[3] D. D. Awschalom and M. E. Flatté, "Challenges for semiconductor spintronics," *Nature Physics,* vol. 3, no. 3, pp. 153-159, 2007.

[4] E. Rashba, "Theory of electrical spin injection: Tunnel contacts as a solution of the conductivity mismatch problem," *Physical Review B,* vol. 62, no. 24, p. R16267, 2000.

[5] H. Zhu, M. Ramsteiner, H. Kostial, M. Wassermeier, H.-P. Schönherr, and K. Ploog, "Room-temperature spin injection from Fe into GaAs," *Physical Review Letters,* vol. 87, no. 1, p. 016601, 2001.

[6] C. Kittel and J. Galt, "Ferromagnetic domain theory," *Solid State Physics,* vol. 3, pp. 437-564, 1956.

[7] N. A. Spaldin, *Magnetic materials: fundamentals and applications*. Cambridge University Press, 2010.

[8] A. Tonomura, "Electron-Holographic Interferometry," in *Electron Holography*: Springer, 1999, pp. 78-132.

[9] J. Jiao, S. Seraphin, X. Wang, and J. C. Withers, "Preparation and properties of ferromagnetic carbon-coated Fe, Co, and Ni nanoparticles," *Journal of Applied Physics,* vol. 80, no. 1, pp. 103-108, 1996.

[10] P. Weiss, "La variation du ferromagnétisme avec la température," *Comptes Rendus,* vol. 143, pp. 1136-1139 特に 1137, 1906.

[11] T. J. Quinn and J. Martin, "A Radiometric Determination of the Stefan-Boltzmann Constant and Thermodynamic Temperatures between-40 degrees C and+ 100 degrees C," *Philosophical Transactions of the Royal Society of London A: Mathematical, Physical and Engineering Sciences,* vol. 316, no. 1536, pp. 85-189, 1985.

[12] A. Cohen, "A Padé approximant to the inverse Langevin function," *Rheologica acta,* vol. 30, no. 3, pp. 270-273, 1991.

[13] M. G. Paterlini and D. M. Ferguson, "Constant temperature simulations using the Langevin equation with velocity Verlet integration," *Chemical physics,* vol. 236, no. 1, pp. 243-252, 1998.

[14] C. Kittel, "Physical theory of ferromagnetic domains," *Reviews of modern Physics,* vol. 21, no. 4, p. 541, 1949.

[15] J. Crangle and G. Goodman, "The magnetization of pure iron and nickel," in *Proceedings of the Royal Society of London A: Mathematical, Physical and Engineering Sciences*, 1971, vol. 321, no. 1547, pp. 477-491: The Royal Society.

[16] W. Heisenberg, "Zur theorie des ferromagnetismus," *Zeitschrift für Physik,* vol. 49, no. 9-10, pp. 619-636, 1928.

[17] R. Cutkosky, "Solutions of a Bethe-Salpeter equation," *Physical Review,* vol. 96, no. 4, p. 1135, 1954.

[18] L. Néel, "Influence des fluctuations des champs moléculaires sur les propriétés magnétiques des corps," Universite, 1932.

[19] K. i. Chahara, T. Ohno, M. Kasai, and Y. Kozono, "Magnetoresistance in magnetic manganese oxide with intrinsic antiferromagnetic spin structure," *Applied Physics Letters,* vol. 63, no. 14, pp. 1990-1992, 1993.

[20] C. L. Henley, "Ordering due to disorder in a frustrated vector antiferromagnet," *Physical review letters,* vol. 62, no. 17, p. 2056, 1989.

[21] C. Ederer and N. A. Spaldin, "Weak ferromagnetism and magnetoelectric coupling in bismuth ferrite," *Physical Review B,* vol. 71, no. 6, p. 060401, 2005.

[22] B. M. Moskowitz, "Hitchhiker's guide to magnetism," in *Environmental Magnetism Workshop (IRM),* 1991, vol. 279, no. 1, p. 48.

[23] B. JAC and B. HEINRICH, "Ultrathin Magnetic Structures I & II," ed: Springer-Verlag, 1994.

[24] S. K. Hanks and T. Hunter, "Protein kinases 6. The eukaryotic protein kinase superfamily: kinase (catalytic) domain structure and classification," *The FASEB journal,* vol. 9, no. 8, pp. 576-596, 1995.

[25] N. Akulov, "Über das magnetische Quadrupolmoment des Eisenatoms," *Zeitschrift für Physik A Hadrons and Nuclei,* vol. 57, no. 3, pp. 249-256, 1929.

[26] N. Akulov, "Zur atomtheorie des ferromagnetismus," *Zeitschrift für Physik A Hadrons and Nuclei,* vol. 54, no. 7, pp. 582-587, 1929.

[27] E. Beaurepaire, J.-C. Merle, A. Daunois, and J.-Y. Bigot, "Ultrafast spin dynamics in ferromagnetic nickel," *Physical review letters,* vol. 76, no. 22, p. 4250, 1996.

[28] B. Heinrich, J. Cochran, T. Monchesky, and R. Urban, "Exchange coupling through spin-density waves in Cr (001) structures: Fe-whisker/Cr/Fe (001) studies," *Physical Review B,* vol. 59, no. 22, p. 14520, 1999.

[29] J. Krebs, B. Jonker, and G. Prinz, "Properties of Fe single-crystal films grown on (100) GaAs by molecular-beam epitaxy," *Journal of applied physics,* vol. 61, no. 7, pp. 2596-2599, 1987.

[30] E. Rhoderick and R. Williams, "Metal Semicond Contacts," *Clarendon, Oxford,* 1988.

[31] Y. Xu, E. Kernohan, M. Tselepi, J. Bland, and S. Holmes, "Single crystal Fe films grown on InAs (100) by molecular beam epitaxy," *Applied physics letters,* vol. 73, no. 3, pp. 399-401, 1998.

[32] J. S. Claydon, D. Niu, Y. Xu, N. D. Telling, I. W. Kirkman, and G. van der Laan, "Spin and orbital moments of ultra-thin Fe films on various semiconductor surfaces," *IEEE transactions on magnetics,* vol. 41, no. 10, pp. 3325-3327, 2005.

[33] Y. Xu, E. Kernohan, D. Freeland, A. Ercole, M. Tselepi, and J. Bland, "Evolution of the ferromagnetic phase of ultrathin Fe films grown on GaAs (100)-4× 6," *Physical Review B,* vol. 58, no. 2, p. 890, 1998.

[34] Y. Xu, D. Freeland, M. Tselepi, and J. Bland, "Anisotropic lattice relaxation and uniaxial magnetic anisotropy in F e/I n A s (100)− 4× 2," *Physical Review B,* vol. 62, no. 2, p. 1167, 2000.

[35] Q. Xue, T. Hashizume, J. Zhou, T. Sakata, T. Ohno, and T. Sakurai, "Structures of the Ga-rich 4× 2 and 4× 6 reconstructions of the GaAs (001) surface," *Physical review letters,* vol. 74, no. 16, p. 3177, 1995.

[36] C. Kendrick, G. LeLay, and A. Kahn, "Bias-dependent imaging of the In-terminated InAs (001)(4× 2) c (8× 2) surface by STM: Reconstruction and transitional defect," *Physical Review B,* vol. 54, no. 24, p. 17877, 1996.

[37] X. Qin and M. Lagally, "Adatom pairing structures for Ge on Si (100): The initial stage of island formation," *Science,* vol. 278, no. 5342, pp. 1444-1447, 1997.

[38] T. J. Zega *et al.*, "Determination of interface atomic structure and its impact on spin transport using Z-contrast microscopy and density-functional theory," *Physical review letters,* vol. 96, no. 19, p. 196101, 2006.

[39] J. M. LeBeau, Q. O. Hu, C. J. Palmstrøm, and S. Stemmer, "Atomic structure of postgrowth annealed epitaxial Fe/(001) GaAs interfaces," *Applied Physics Letters,* vol. 93, no. 12, p. 121909, 2008.

[40] L. Fleet, H. Kobayashi, Y. Ohno, and A. Hirohata, "Atomic Interfacial Structures in Fe/GaAs Films," *IEEE Transactions on Magnetics,* vol. 47, no. 10, pp. 2756-2759, 2011.

[41] L. Fleet, H. Kobayashi, Y. Ohno, J.-Y. Kim, C. Barnes, and A. Hirohata, "Interfacial structure and transport properties of Fe/GaAs (001)," *Journal of Applied Physics,* vol. 109, no. 7, p. 07C504, 2011.

[42] L. Fleet *et al.*, "Correlating the interface structure to spin injection in abrupt Fe/GaAs (001) films," *Physical Review B,* vol. 87, no. 2, p. 024401, 2013.

[43] A. Filipe, A. Schuhl, and P. Galtier, "Structure and magnetism of the Fe/GaAs interface," *Applied physics letters,* vol. 70, no. 1, pp. 129-131, 1997.

[44] G. Prinz, G. Rado, and J. Krebs, "Magnetic properties of single-crystal {110} iron films grown on GaAs by molecular beam epitaxy," *Journal of Applied Physics,* vol. 53, no. 3, pp. 2087-2091, 1982.

[45] J. Claydon, Y. Xu, M. Tselepi, J. Bland, and G. Van der Laan, "Direct Observation of a Bulklike Spin Moment at the F e/G a A s (100)− 4× 6 Interface," *Physical review letters,* vol. 93, no. 3, p. 037206, 2004.

[46] Y. Xu, D. Freeland, M. Tselepi, and J. Bland, "Uniaxial magnetic anisotropy of epitaxial Fe films on InAs (100)-4× 2 and GaAs (100)-4× 2," *Journal of Applied Physics,* vol. 87, no. 9, pp. 6110-6112, 2000.

[47] E. Kneedler, B. Jonker, P. Thibado, R. Wagner, B. Shanabrook, and L. Whitman, "Influence of substrate surface reconstruction on the growth and magnetic properties of Fe on GaAs (001)," *Physical Review B,* vol. 56, no. 13, p. 8163, 1997.

[48] M. Brockmann, M. Zölfl, S. Miethaner, and G. Bayreuther, "In-plane volume and interface magnetic anisotropies in epitaxial Fe films on GaAs (001)," *Journal of magnetism and magnetic materials,* vol. 198, pp. 384-386, 1999.

[49] I. Present, "Cramming more components onto integrated circuits," *Readings in computer architecture,* vol. 56, 2000.

[50] K. L. Wang, J. G. Alzate, and P. Khalili Amiri, "Low-power non-volatile spintronic memory: STT-RAM and beyond," *Journal of Physics D: Applied Physics,* vol. 46, no. 7, 2013.

[51] S. Assefa *et al.*, "Fabrication and characterization of MgO-based magnetic tunnel junctions for spin momentum transfer switching," *Journal of Applied Physics,* vol. 102, no. 6, p. 063901, 2007.

[52] C. Lin *et al.*, "45nm low power CMOS logic compatible embedded STT MRAM utilizing a reverse-connection 1T/1MTJ cell," in *Electron Devices Meeting (IEDM), 2009 IEEE International*, 2009, pp. 1-4: IEEE.

[53] Y. Huai, F. Albert, P. Nguyen, M. Pakala, and T. Valet, "Observation of spin-transfer switching in deep submicron-sized and low-resistance magnetic tunnel junctions," *Applied Physics Letters,* vol. 84, no. 16, pp. 3118-3120, 2004.

[54] E. Chen *et al.*, "Advances and Future Prospects of Spin-Transfer Torque Random Access Memory," *IEEE Transactions on Magnetics,* vol. 46, no. 6, pp. 1873-1878, 2010.

[55] J. A. Katine, F. J. Albert, R. A. Buhrman, E. B. Myers, and D. C. Ralph, "Current-driven magnetization reversal and spin-wave excitations in Co/Cu/Co pillars," (in English), *Physical Review Letters,* vol. 84, no. 14, pp. 3149-3152, Apr 3 2000.

[56] S. S. Parkin *et al.*, "Giant tunnelling magnetoresistance at room temperature with MgO (100) tunnel barriers," *Nat Mater,* vol. 3, no. 12, pp. 862-7, Dec 2004.

[57] J. C. Slonczewski, "Current-driven excitation of magnetic multilayers," (in English), *Journal of Magnetism and Magnetic Materials,* vol. 159, no. 1-2, pp. L1-L7, Jun 1996.

[58] L. Berger, "Emission of spin waves by a magnetic multilayer traversed by a current," *Phys Rev B Condens Matter,* vol. 54, no. 13, pp. 9353-9358, Oct 1 1996.

[59] K. Lee and S. H. Kang, "Development of embedded STT-MRAM for mobile system-on-chips," *IEEE Transactions on Magnetics,* vol. 47, no. 1, pp. 131-136, 2011.

[60] A. V. Khvalkovskiy *et al.*, "Erratum: Basic principles of STT-MRAM cell operation in memory arrays," *Journal of Physics D: Applied Physics,* vol. 46, no. 13, 2013.

[61] J. Z. Sun, "Spin-current interaction with a monodomain magnetic body: A model study," (in English), *Physical Review B,* vol. 62, no. 1, pp. 570-578, Jul 1 2000.

[62] S. Ikeda *et al.*, "Tunnel magnetoresistance of 604% at 300K by suppression of Ta diffusion in CoFeB∕MgO∕CoFeB pseudo-spin-valves annealed at high temperature," *Applied Physics Letters,* vol. 93, no. 8, 2008.

[63] B. Liu *et al.*, "Transient enhancement of magnetization damping in CoFeB film via pulsed laser excitation," (in English), *Applied Physics Letters,* vol. 109, no. 4, p. 042401, Jul 25 2016.

[64] D. D. Djayaprawira *et al.*, "230% room-temperature magnetoresistance in CoFeB∕MgO∕CoFeB magnetic tunnel junctions," *Applied Physics Letters,* vol. 86, no. 9, 2005.

[65] J. J. Cha *et al.*, "Atomic-scale spectroscopic imaging of CoFeB/Mg–B–O/CoFeB magnetic tunnel junctions," *Applied Physics Letters,* vol. 95, no. 3, 2009.

[66] K. Tsunekawa *et al.*, "Giant tunneling magnetoresistance effect in low-resistance CoFeB∕MgO(001)∕CoFeB magnetic tunnel junctions for read-head applications," *Applied Physics Letters,* vol. 87, no. 7, 2005.

[67] S. Ikeda *et al.*, "A perpendicular-anisotropy CoFeB-MgO magnetic tunnel junction," *Nat Mater,* vol. 9, no. 9, pp. 721-4, Sep 2010.

[68] D. C. Worledge *et al.*, "Spin torque switching of perpendicular Ta | CoFeB | MgO-based magnetic tunnel junctions," *Applied Physics Letters,* vol. 98, no. 2, 2011.

[69] C. A. Chang, R. Ludeke, L. Chang, and L. Esaki, "Molecular-beam epitaxy (MBE) of In1− x Ga x As and GaSb1− y As y," *Applied Physics Letters,* vol. 31, no. 11, pp. 759-761, 1977.

[70] A. Cho and H. Casey Jr, "Properties of Schottky barriers and p-n junctions prepared with GaAs and Al x Ga1− x As molecular beam epitaxial layers," *Journal of Applied Physics,* vol. 45, no. 3, pp. 1258-1263, 1974.

[71] K. Ploog and A. Fischer, "Surface segregation of Sn during MBE of n-type GaAs established by SIMS and AES," *Journal of Vacuum Science and Technology,* vol. 15, no. 2, pp. 255-259, 1978.

[72] D. V. Morgan and K. Board, *An introduction to semiconductor microtechnology*. John Wiley & Sons, 1990.

[73] J. Y. Tsao, *Materials fundamentals of molecular beam epitaxy*. Academic Press, 2012.

[74] A. Chambers, *Modern vacuum physics*. CRC Press, 2004.

[75] J. George, *Preparation of thin films*. CRC Press, 1992.

[76] *wafertech*. Available: http://www.wafertech.co.uk/products/categories-off-orientation/

[77] Wikipedia. (2010). *Transmission Electron Microscopy*. Available: http://en.wikipedia.org/wiki/Transmission_electron_microscopy

[78] D. Smith, "Development of a Vibrating-Coil Magnetometer," *Review of Scientific Instruments,* vol. 27, no. 5, pp. 261-268, 1956.

[79] S. Foner, "Versatile and sensitive vibrating-sample magnetometer," *Review of Scientific Instruments,* vol. 30, no. 7, pp. 548-557, 1959.

[80] J. Kerr, "XLIII. On rotation of the plane of polarization by reflection from the pole of a magnet," *The London, Edinburgh, and Dublin Philosophical Magazine and Journal of Science,* vol. 3, no. 19, pp. 321-343, 1877.

[81] M. Faraday, "Experimental researches in electricity. Nineteenth series," *Philosophical Transactions of the Royal Society of London,* vol. 136, pp. 1-20, 1846.

[82] D. J. Griffiths and E. G. Harris, "Introduction to quantum mechanics," *American Journal of Physics,* vol. 63, no. 8, pp. 767-768, 1995.

[83] Wikipedia. (2010). *Hysteresis loop*. Available: https://en.wikipedia.org/wiki/Hysteresis

[84] D. L. Source. (2017). *Diamond's beamlines*. Available: http://www.diamond.ac.uk/Beamlines/

[85] J. Stöhr, "X-ray magnetic circular dichroism spectroscopy of transition metal thin films," *Journal of Electron Spectroscopy and Related Phenomena,* vol. 75, pp. 253-272, 1995.

[86] J. Stöhr and H. C. Siegmann, *Magnetism: from fundamentals to nanoscale dynamics*. Springer Science & Business Media, 2007.

[87] J. Stöhr, *NEXAFS spectroscopy*. Springer Science & Business Media, 2013.

[88] F. Wilhelm, *Magnetic Properties of Ultrathin Films, Coupled Trilayers and 3d, 5d Multilayers Studied by X-ray Magnetic Circular Dichroism*. dissertation. de, 2000.

[89] B. Thole, P. Carra, F. Sette, and G. van der Laan, "X-ray circular dichroism as a probe of orbital magnetization," *Physical Review Letters,* vol. 68, no. 12, p. 1943, 1992.

[90] P. Carra, B. Thole, M. Altarelli, and X. Wang, "X-ray circular dichroism and local magnetic fields," *Physical Review Letters,* vol. 70, no. 5, p. 694, 1993.

[91] C. Chen *et al.*, "Experimental confirmation of the X-ray magnetic circular dichroism sum rules for iron and cobalt," *Physical review letters,* vol. 75, no. 1, p. 152, 1995.

[92] B. Cui, C. Song, Y. Wang, W. Yan, F. Zeng, and F. Pan, "Tuning of uniaxial magnetic anisotropy in amorphous CoFeB films," *Journal of Physics: Condensed Matter,* vol. 25, no. 10, p. 106003, 2013.

[93] G. Wastlbauer and J. Bland*, "Structural and magnetic properties of ultrathin epitaxial Fe films on GaAs (001) and related semiconductor substrates," *Advances in physics,* vol. 54, no. 2, pp. 137-219, 2005.

[94] J. Sinha *et al.*, "Enhanced interface perpendicular magnetic anisotropy in Ta| CoFeB| MgO using nitrogen doped Ta underlayers," *Applied Physics Letters,* vol. 102, no. 24, p. 242405, 2013.

[95] W. Tsai *et al.*, "Investigation of perpendicular magnetic anisotropy of CoFeB by x-ray magnetic circular dichroism," *Applied Physics Letters,* vol. 100, no. 17, p. 172414, 2012.

[96] F. Bianco, P. Bouchon, M. Sousa, G. Salis, and S. Alvarado, "Enhanced uniaxial magnetic anisotropy in Fe 31 Co 69 thin films on GaAs (001)," *Journal of Applied Physics,* vol. 104, no. 8, p. 083901, 2008.

[97] Y. Xu *et al.*, "Hybrid spintronic structures with magnetic oxides and Heusler alloys," *IEEE Transactions on Magnetics,* vol. 44, no. 11, pp. 2959-2965, 2008.

[98] A. Ionescu *et al.*, "Submonolayer growth of Fe on a Ga As (100)− 2× 6 reconstructed surface," *Physical Review B,* vol. 72, no. 12, p. 125404, 2005.

[99] M. Dumm, M. Zölfl, R. Moosbühler, M. Brockmann, T. Schmidt, and G. Bayreuther, "Magnetism of ultrathin FeCo (001) films on GaAs (001)," *Journal of Applied Physics,* vol. 87, no. 9, pp. 5457-5459, 2000.

[100] P. Bruno, "Tight-binding approach to the orbital magnetic moment and magnetocrystalline anisotropy of transition-metal monolayers," *Physical Review B,* vol. 39, no. 1, p. 865, 1989.

[101] A. Hindmarch, A. Rushforth, R. Campion, C. Marrows, and B. Gallagher, "Origin of in-plane uniaxial magnetic anisotropy in CoFeB amorphous ferromagnetic thin films," *Physical Review B,* vol. 83, no. 21, p. 212404, 2011.

[102] J. Hafner, M. Tegze, and C. Becker, "Amorphous magnetism in Fe-B alloys: First-principles spin-polarized electronic-structure calculations," *Physical Review B,* vol. 49, no. 1, p. 285, 1994.

[103] D. Gillingham *et al.*, "Smoothening of ultrathin Fe films grown on GaAs (100) observed by scanning tunneling microscopy and Brillouin light scattering," *Physical Review B,* vol. 76, no. 21, p. 214412, 2007.

[104] T. Egami *et al.*, "Anisotropy and coercivity of amorphous RE-TM films," *IEEE transactions on magnetics,* vol. 23, no. 5, pp. 2269-2271, 1987.

[105] R. Alben, J. Becker, and M. Chi, "Random anisotropy in amorphous ferromagnets," *Journal of applied physics,* vol. 49, no. 3, pp. 1653-1658, 1978.

[106] A. Hindmarch *et al.*, "Interface induced uniaxial magnetic anisotropy in amorphous CoFeB films on AlGaAs (001)," *Physical review letters,* vol. 100, no. 11, p. 117201, 2008.

[107] A. Hindmarch, D. Arena, K. Dempsey, M. Henini, and C. Marrows, "Influence of deposition field on the magnetic anisotropy in epitaxial Co 70 Fe 30 films on GaAs (001)," *Physical Review B,* vol. 81, no. 10, p. 100407, 2010.

[108] W. Liu *et al.*, "Spin and orbital moments of nanoscale Fe3O4 epitaxial thin film on MgO/GaAs (100)," *Applied Physics Letters,* vol. 104, no. 14, p. 142407, 2014.

[109] R. Skomski, A. Kashyap, and A. Enders, "Is the magnetic anisotropy proportional to the orbital moment?," *Journal of Applied Physics,* vol. 109, no. 7, p. 07E143, 2011.

[110] H. Q. Tu, B. You, Y. Q. Zhang, Y. Gao, Y. B. Xu, and J. Du, "Uniaxial Magnetic Anisotropy in Amorphous CoFeB Films on Different Orientational GaAs Substrates," *IEEE Transactions on Magnetics,* vol. 51, no. 11, pp. 1-4, 2015.

[111] J. Trygg, B. Johansson, O. Eriksson, and J. Wills, "Total Energy Calculation of the Magnetocrystalline Anisotropy Energy in the Ferromagnetic 3 d Metals," *Physical review letters,* vol. 75, no. 15, p. 2871, 1995.

[112] Y. Xu *et al.*, "Giant enhancement of orbital moments and perpendicular anisotropy in epitaxial Fe/GaAs (100)," *Journal of Applied Physics,* vol. 89, no. 11, pp. 7156-7158, 2001.

[113] W. Liu *et al.*, "Evidence for ferromagnetic coupling at the doped topological insulator/ferrimagnetic insulator interface," *AIP Advances,* vol. 6, no. 5, p. 055813, 2016.

[114] L. Lari, S. Lea, C. Feeser, B. W. Wessels, and V. K. Lazarov, "Ferromagnetic InMnSb multi-phase films study by aberration-corrected (scanning) transmission electron microscopy," *Journal of Applied Physics,* vol. 111, no. 7, p. 07C311, 2012.

[115] D. D. Djayaprawira *et al.*, "230% room-temperature magnetoresistance in CoFeB⁄ MgO⁄ CoFeB magnetic tunnel junctions," *Applied Physics Letters,* vol. 86, no. 9, p. 092502, 2005.

[116] C. Chen *et al.*, "Element-specific magnetic hysteresis as a means for studying heteromagnetic multilayers," *Physical Review B,* vol. 48, no. 1, p. 642, 1993.

[117] T. Ueno *et al.*, "Enhanced orbital magnetic moments in magnetic heterostructures with interface perpendicular magnetic anisotropy," *Scientific reports,* vol. 5, 2015.

[118] I. Kowalik *et al.*, "Description of the new I1011 beamline for magnetic measurements using synchrotron radiation at MAX-lab," in *Journal of Physics: Conference Series*, 2010, vol. 211, no. 1, p. 012030: IOP Publishing.

[119] S. Kanai, M. Tsujikawa, Y. Miura, M. Shirai, F. Matsukura, and H. Ohno, "Magnetic anisotropy in Ta/CoFeB/MgO investigated by x-ray magnetic circular dichroism and first-principles calculation," *Applied Physics Letters,* vol. 105, no. 22, p. 222409, 2014.

[120] A. T. Hindmarch *et al.*, "Interface Induced Uniaxial Magnetic Anisotropy in Amorphous CoFeB Films on AlGaAs(001)," *Physical Review Letters,* vol. 100, no. 11, 2008.

[121] C. T. Chen *et al.*, "Experimental confirmation of the X-ray magnetic circular dichroism sum rules for iron and cobalt," *Phys Rev Lett,* vol. 75, no. 1, pp. 152-155, Jul 3 1995.

[122] C. T. Chen *et al.*, "Element-specific magnetic hysteresis as a means for studying heteromagnetic multilayers," *Physical Review B,* vol. 48, no. 1, pp. 642-645, 1993.

[123] T. Liu, Y. Zhang, J. Cai, and H. Pan, "Thermally robust Mo/CoFeB/MgO trilayers with strong perpendicular magnetic anisotropy," *Scientific reports,* vol. 4, 2014.

[124] E. Barati, M. Cinal, D. Edwards, and A. Umerski, "Gilbert damping in magnetic layered systems," *Physical Review B,* vol. 90, no. 1, p. 014420, 2014.

[125] J. Sinha *et al.*, "Influence of boron diffusion on the perpendicular magnetic anisotropy in Ta| CoFeB| MgO ultrathin films," *Journal of Applied Physics,* vol. 117, no. 4, p. 043913, 2015.

[126] D. Kim *et al.*, "Perpendicular magnetization of CoFeB on top of an amorphous buffer layer," *Journal of Magnetism and Magnetic materials,* vol. 374, pp. 350-353, 2015.

[127] S. Iihama, S. Mizukami, H. Naganuma, M. Oogane, Y. Ando, and T. Miyazaki, "Gilbert damping constants of Ta/CoFeB/MgO (Ta) thin films measured by optical detection of precessional magnetization dynamics," *Physical Review B,* vol. 89, no. 17, p. 174416, 2014.

[128] X. Liu, W. Zhang, M. J. Carter, and G. Xiao, "Ferromagnetic resonance and damping properties of CoFeB thin films as free layers in MgO-based magnetic tunnel junctions," *Journal of Applied Physics,* vol. 110, no. 3, p. 033910, 2011.

[129] Q. Zhang *et al.*, "Polarization-Mediated Thermal Stability of Metal/Oxide Heterointerface," *Advanced Materials,* vol. 27, no. 43, pp. 6934-6938, 2015.

[130] J. Teixeira *et al.*, "Domain imaging, MOKE and magnetoresistance studies of CoFeB films for MRAM applications," *Materials Science and Engineering: B,* vol. 126, no. 2, pp. 180-186, 2006.

[131] T. Zhu, P. Chen, Q. Zhang, R. Yu, and B. Liu, "Giant linear anomalous Hall effect in the perpendicular CoFeB thin films," *Applied Physics Letters,* vol. 104, no. 20, p. 202404, 2014.

[132] S. Ikeda *et al.*, "A perpendicular-anisotropy CoFeB–MgO magnetic tunnel junction," *Nature materials,* vol. 9, no. 9, pp. 721-724, 2010.

[133] A. Brataas, A. D. Kent, and H. Ohno, "Current-induced torques in magnetic materials," *Nature materials,* vol. 11, no. 5, pp. 372-381, 2012.

[134] T. Zhu, Y. Yang, R. Yu, H. Ambaye, V. Lauter, and J. Xiao, "The study of perpendicular magnetic anisotropy in CoFeB sandwiched by MgO and tantalum layers using polarized neutron reflectometry," *Applied Physics Letters,* vol. 100, no. 20, p. 202406, 2012.

[135] M. Yoshikawa *et al.*, "Tunnel Magnetoresistance Over 100% in MgO-Based Magnetic Tunnel Junction Films With Perpendicular Magnetic L1 $ _ {0} $-FePt Electrodes," *IEEE Transactions on Magnetics,* vol. 44, no. 11, pp. 2573-2576, 2008.

[136] H. Danan, A. Herr, and A. Meyer, "New determinations of the saturation magnetization of nickel and iron," *Journal of Applied Physics,* vol. 39, no. 2, pp. 669-670, 1968.

[137] B. Liu *et al.*, "The effect of growth sequence on magnetization damping in Ta/CoFeB/MgO structures," *Journal of Magnetism and Magnetic Materials,* 2017.

[138] S. Datta and B. Das, "Electronic analog of the electro-optic modulator," *Applied Physics Letters,* vol. 56, no. 7, pp. 665-667, 1990.

[139] B. Jonker, "Progress toward electrical injection of spin-polarized electrons into semiconductors," *Proceedings of the IEEE,* vol. 91, no. 5, pp. 727-740, 2003.

[140] D. Keavney, D. Wu, J. Freeland, E. Johnston-Halperin, D. Awschalom, and J. Shi, "Element resolved spin configuration in ferromagnetic manganese-doped gallium arsenide," *Physical review letters,* vol. 91, no. 18, p. 187203, 2003.

[141] M. Marangolo *et al.*, "Magnetism of the Fe/ZnSe (001) interface," *Physical review letters,* vol. 88, no. 21, p. 217202, 2002.

[142] S. Wolf *et al.*, "Spintronics: a spin-based electronics vision for the future," *Science,* vol. 294, no. 5546, pp. 1488-1495, 2001.

[143] Y. Xu *et al.*, "Ferromagnetic metal/semiconductor hybrid structures for magnetoelectronics," *Journal of applied physics,* vol. 85, no. 8, pp. 5369-5371, 1999.

[144] F. Bensch, G. Garreau, R. Moosbühler, G. Bayreuther, and E. Beaurepaire, "Onset of ferromagnetism in Fe epitaxially grown on GaAs (001)(4× 2) and (2× 6)," *Journal of Applied Physics,* vol. 89, no. 11, pp. 7133-7135, 2001.

[145] Y. Yan *et al.*, "Element specific spin and orbital moments of nanoscale CoFeB amorphous thin films on GaAs(100)," *AIP Advances,* vol. 6, no. 9, 2016.

[146] M. Zölfl *et al.*, "Magnetic films epitaxially grown on semiconductors," *Journal of Magnetism and Magnetic Materials,* vol. 175, no. 1-2, pp. 16-22, 1997.

[147] J. Freeland, I. Coulthard, W. Antel Jr, and A. Stampfl, "Interface bonding for Fe thin films on GaAs surfaces of differing morphology," *Physical Review B,* vol. 63, no. 19, p. 193301, 2001.

[148] F. Bensch, R. Moosbühler, and G. Bayreuther, "Onset of magnetic anisotropy in epitaxial Fe films on GaAs (001)," *Journal of applied physics,* vol. 91, no. 10, pp. 8754-8756, 2002.

[149] O. Durand, J. Childress, P. Galtier, R. Bisaro, and A. Schuhl, "Origin of the uniaxial magnetic anisotropy in Fe films grown by molecular beam epitaxy," *Journal of magnetism and magnetic materials,* vol. 145, no. 1-2, pp. 111-117, 1995.

[150] E. Pugh, J. Matisoo, D. Speliotis, and E. Boyd, "Magnetic anisotropy in evaporated iron films," *Journal of Applied Physics,* vol. 31, no. 5, pp. S293-S295, 1960.

[151] T. Knorr and R. Hoffman, "Dependence of geometric magnetic anisotropy in thin iron films," *Physical Review,* vol. 113, no. 4, p. 1039, 1959.

[152] D. J. Huang, J. Lee, G. Mulhollan, and J. Erskine, "Influence of surface atomic steps on in-plane magnetic anisotropy of ultrathin Fe films on W (001)," *Journal of applied physics,* vol. 73, no. 10, pp. 6751-6753, 1993.

[153] P. Krams, B. Hillebrands, G. Güntherodt, and H. Oepen, "Magnetic anisotropies of ultrathin Co films on Cu (1 1 13) substrates," *Physical review B,* vol. 49, no. 5, p. 3633, 1994.

[154] J. Claydon, Y. Xu, M. Tselepi, J. Bland, and G. van der Laan, "Magnetic moments of ferromagnetic, superparamagnetic, and submonolayer Fe on a GaAs (100) surface," *Journal of applied physics,* vol. 95, no. 11, pp. 6543-6545, 2004.

[155] Z.-P. Shi, P. M. Levy, and J. L. Fry, "Spin polarization of epitaxial Cr on Fe (001) and interlayer magnetic coupling in Fe/Cr multilayered structures," *Physical review letters,* vol. 69, no. 25, p. 3678, 1992.

[156] C. Carbone and S. Alvarado, "Antiparallel coupling between Fe layers separated by a Cr interlayer: dependence of the magnetization on the film thickness," *Physical Review B,* vol. 36, no. 4, p. 2433, 1987.

[157] K. Ounadjela, C. Sommers, A. Fert, D. Stoeffler, F. Gautier, and V. Moruzzi, "Electronic structure and interlayer exchange coupling in Fe/Cr superlattices," *EPL (Europhysics Letters),* vol. 15, no. 8, p. 875, 1991.

[158] W. Lee, B.-C. Choi, Y. Xu, and J. Bland, "Magnetization reversal dynamics in epitaxial Fe/GaAs (001) thin films," *Physical Review B,* vol. 60, no. 14, p. 10216, 1999.

[159] K. Suzuki, N. Kataoka, A. Inoue, A. Makino, and T. Masumoto, "High saturation magnetization and soft magnetic properties of bcc Fe–Zr–B alloys with ultrafine grain structure," *Materials Transactions, JIM,* vol. 31, no. 8, pp. 743-746, 1990.

[160] C. Paduani and J. Krause, "A first-principles study of Cr impurities in iron," *Brazilian journal of physics,* vol. 36, no. 4A, pp. 1262-1266, 2006.

[161] H. Wang *et al.*, "High-precision soft x-ray polarimeter at Diamond Light Source," *Review of Scientific Instruments,* vol. 82, no. 12, p. 123301, 2011.

[162] G. Woltersdorf, M. Buess, B. Heinrich, and C. Back, "Time resolved magnetization dynamics of ultrathin Fe (001) films: Spin-pumping and two-magnon scattering," *Physical review letters,* vol. 95, no. 3, p. 037401, 2005.

[163] S. Rezende, A. Azevedo, M. Lucena, and F. De Aguiar, "Anomalous spin-wave damping in exchange-biased films," *Physical Review B,* vol. 63, no. 21, p. 214418, 2001.

[164] C. Mathieu *et al.*, "Brillouin light scattering investigations of exchange biased (110)-oriented NiFe/FeMn bilayers," *Journal of applied physics,* vol. 83, no. 5, pp. 2863-2865, 1998.

[165] R. D. McMichael, M. D. Stiles, P. Chen, and W. F. Egelhoff Jr, "Ferromagnetic resonance linewidth in thin films coupled to NiO," *Journal of applied physics,* vol. 83, no. 11, pp. 7037-7039, 1998.

[166] A. Scherz, H. Wende, and K. Baberschke, "Fine structure of X-ray magnetic circular dichroism for early 3 d transition metals," *Applied Physics A: Materials Science & Processing,* vol. 78, no. 6, pp. 843-846, 2004.

[167] P. Carra, H. König, B. Thole, and M. Altarelli, "Magnetic x-ray dichroism: General features of dipolar and quadrupolar spectra," *Physica B: Condensed Matter,* vol. 192, no. 1-2, pp. 182-190, 1993.

[168] H. Ebert and G. Schütz, "Spin---Orbit-Influenced Spectroscopies of Magnetic Solids," in *Lecture Notes in Physics, Berlin Springer Verlag*, 1996, vol. 466.

[169] Y. Idzerda, C. Chen, H.-J. Lin, G. Meigs, G. Ho, and C.-C. Kao, "Soft X-ray magnetic circular dichroism and magnetic films," *Nuclear Instruments and Methods in Physics Research Section A: Accelerators, Spectrometers, Detectors and Associated Equipment,* vol. 347, no. 1, pp. 134-141, 1994.

[170] G. Harp, S. Parkin, W. O'Brien, and B. Tonner, "X-ray magnetic-circular-dichroism study of Fe/V multilayers," *Physical Review B,* vol. 51, no. 5, p. 3293, 1995.

[171] G. van der Laan, "The role of the spin polarization in x-ray magnetic circular dichroism spectra of itinerant magnets," *Journal of Physics: Condensed Matter,* vol. 9, no. 18, p. L259, 1997.

[172] A. Scherz, P. Poulopoulos, H. Wende, G. Ceballos, K. Baberschke, and F. Wilhelm, "Thickness dependence of the V induced magnetic moment in Fe/V/Fe (110) trilayers," *Journal of applied physics,* vol. 91, no. 10, pp. 8760-8762, 2002.

[173] R. Coehoorn, "Relation between interfacial magnetism and spin-dependent scattering at non-ideal Fe/Cr and Fe/V interfaces," *Journal of magnetism and magnetic materials,* vol. 151, no. 3, pp. 341-353, 1995.

[174] D. Koelling, "Magnetic multilayers with (Nb, Mo, Cr) spacer materials," *Physical Review B,* vol. 50, no. 1, p. 273, 1994.

[175] D. Venus and B. Heinrich, "Interfacial mixing of ultrathin Cr films grown on an Fe whisker," *Physical Review B,* vol. 53, no. 4, p. R1733, 1996.

[176] M. Tomaz, W. Antel, W. O'Brien, and G. Harp, "Orientation dependence of interlayer coupling and interlayer moments in Fe/Cr multilayers," *Physical Review B,* vol. 55, no. 6, p. 3716, 1997.

[177] W. Alayo, M. Tafur, Y. Xing, E. Baggio-Saitovitch, V. Nascimento, and A. Alvarenga, "Study of the interfacial regions in Fe⁄ Cr multilayers," *Journal of Applied Physics,* vol. 102, no. 7, p. 073902, 2007.

[178] T. Walker, A. Pang, H. Hopster, and S. Alvarado, "Magnetic ordering of Cr layers on Fe (100)," *Physical review letters,* vol. 69, no. 7, p. 1121, 1992.

[179] D. T. Pierce, R. Celotta, and J. Unguris, "Magnetic moments in Cr thin films on Fe (100)," *Journal of applied physics,* vol. 73, no. 10, pp. 6201-6203, 1993.

[180] C. Turtur and G. Bayreuther, "Magnetic moments in ultrathin Cr films on Fe (100)," *Physical review letters,* vol. 72, no. 10, p. 1557, 1994.

[181] Y. Idzerda, L. Tjeng, H.-J. Lin, C. Gutierrez, G. Meigs, and C. Chen, "Magnetic structure of Fe/Cr/Fe trilayers," *Surface science,* vol. 287, pp. 741-746, 1993.

[182] J. Unguris, R. Celotta, and D. T. Pierce, "Magnetism in Cr thin films on Fe (100)," *Physical review letters,* vol. 69, no. 7, p. 1125, 1992.

[183] A. Scherz, H. Wende, K. Baberschke, J. Minár, D. Benea, and H. Ebert, "Relation between L 2, 3 XMCD and the magnetic ground-state properties for the early 3 d element V," *Physical Review B,* vol. 66, no. 18, p. 184401, 2002.

[184] A. Scherz *et al.*, "Limitations of integral XMCD sum-rules for the early 3d elements," *Physica Scripta,* vol. 2005, no. T115, p. 586, 2005.

[185] X. Liu, W. Liu, and Z. Zhang, "Evolution of magnetic properties in the vicinity of the Verwey transition in Fe 3 O 4 thin films," *Physical Review B,* vol. 96, no. 9, p. 094405, 2017.

[186] Y. Lu, J. Claydon, Y. Xu, S. Thompson, K. Wilson, and G. Van der Laan, "Epitaxial growth and magnetic properties of half-metallic Fe 3 O 4 on GaAs (100)," *Physical Review B,* vol. 70, no. 23, p. 233304, 2004.

[187] E. Goering, M. Lafkioti, S. Gold, and G. Schuetz, "Absorption spectroscopy and XMCD at the Verwey transition of Fe 3 O 4," *Journal of Magnetism and Magnetic Materials,* vol. 310, no. 2, pp. e249-e251, 2007.

[188] D. Huang *et al.*, "Spin and Orbital Magnetic Moments of F e 3 O 4," *Physical review letters,* vol. 93, no. 7, p. 077204, 2004.

[189] J. Duffy *et al.*, "Spin and orbital moments in Fe 3 O 4," *Physical Review B,* vol. 81, no. 13, p. 134424, 2010.

[190] A. Froideval *et al.*, "Magnetic and structural properties of FeCr alloys," *Physical review letters,* vol. 99, no. 23, p. 237201, 2007.

[191] A. Bogdanov and U. Rößler, "Chiral symmetry breaking in magnetic thin films and multilayers," *Physical review letters,* vol. 87, no. 3, p. 037203, 2001.

[192] R. Kawakami, E. J. Escorcia-Aparicio, and Z. Qiu, "Symmetry-induced magnetic anisotropy in Fe films grown on stepped Ag (001)," *Physical review letters,* vol. 77, no. 12, p. 2570, 1996.

[193] H. Okamoto, T. Massalski, L. Swartzendruber, and P. Beck, "The Au− Fe (gold-iron) system," *Bulletin of Alloy Phase Diagrams,* vol. 5, no. 6, pp. 592-601, 1984.

[194] D. Die, X.-Y. Kuang, J.-J. Guo, and B.-X. Zheng, "First-principle study of AunFe (n= 1–7) clusters," *Journal of Molecular Structure: THEOCHEM,* vol. 902, no. 1, pp. 54-58, 2009.

[195] F. Wilhelm *et al.*, "Au and Fe magnetic moments in disordered Au-Fe alloys," *Physical Review B,* vol. 77, no. 22, p. 224414, 2008.

[196] H. L. Liu, J. H. Wu, J. H. Min, and Y. K. Kim, "Synthesis of monosized magnetic-optical AuFe alloy nanoparticles," *Journal of Applied Physics,* vol. 103, no. 7, p. 07D529, 2008.

[197] P. Crespo *et al.*, "Fe impurities weaken the ferromagnetic behavior in Au nanoparticles," *Physical review letters,* vol. 97, no. 17, p. 177203, 2006.

[198] T. Nahm, H. Noh, B. Choi, J.-S. Park, S. Oh, and E. Cho, "Photoelectron spectroscopy study of Fe-diluted Au–Fe alloys," *Journal of Physics: Condensed Matter,* vol. 15, no. 19, p. 3181, 2003.

[199] A. Błachowski, K. Ruebenbauer, J. Przewoźnik, and J. Żukrowski, "Hyperfine interactions on iron nuclei in the BCC and fractally decomposed BCC/FCC mixed

phase iron–gold alloys," *Journal of Alloys and Compounds,* vol. 458, no. 1, pp. 96-103, 2008.

[200] T. Klemmer *et al.*, "Structural studies of L 1 0 FePt nanoparticles," *Applied Physics Letters,* vol. 81, no. 12, pp. 2220-2222, 2002.

[201] Q. Xiao, E. Brück, Z. Zhang, F. de Boer, and K. Buschow, "Effect of ordering transformation rate on the magnetic properties of Fe–Pt-based bulk alloys," *Journal of magnetism and magnetic materials,* vol. 280, no. 2, pp. 381-390, 2004.

[202] Q. Xiao, E. Brück, Z. Zhang, F. De Boer, and K. Buschow, "Phase transformation and magnetic properties of Fe–Pt-based bulk alloys," *Journal of alloys and compounds,* vol. 364, no. 1, pp. 315-322, 2004.

[203] V. Gavrilenko and R. Wu, "Magneto-optical properties of FeAu alloys and Fe/Au superlattices," *Journal of applied physics,* vol. 85, no. 8, pp. 5112-5114, 1999.

[204] K. Takanashi, S. Mitani, M. Sano, H. Fujimori, H. Nakajima, and A. Osawa, "Artificial fabrication of an L 10-type ordered FeAu alloy by alternate monatomic deposition," *Applied physics letters,* vol. 67, no. 7, pp. 1016-1018, 1995.

[205] Y. Ko *et al.*, "Pressure–volume equation of state of FeAu and FePt," *High Pressure Research,* vol. 29, no. 4, pp. 800-805, 2009.

[206] K. Buschow, P. Van Engen, and R. Jongebreur, "Magneto-optical properties of metallic ferromagnetic materials," *Journal of magnetism and magnetic materials,* vol. 38, no. 1, pp. 1-22, 1983.

[207] J. Lv, J.-Y. Zhang, R.-R. Liang, and H.-S. Wu, "Structures, stabilities, and magnetic properties of the FenAu (n= 1 n= 1 n= 1 12) clusters," 2016.

[208] M. McHenry, J. MacLaren, M. Eberhart, and S. Crampin, "Electronic and magnetic properties of Fe/Au multilayers and interfaces," *Journal of Magnetism and Magnetic Materials,* vol. 88, no. 1-2, pp. 134-150, 1990.